Advances of the
Material Science and Engineering

Proceedings of the Workshop on Advances of the Material Science and Engineering 2023

Editors
Aniruddha Mondal
Rabindra Nath Barman
Tushar Kanti Bera
Arindam Biswas

ADVANCES OF THE MATERIAL SCIENCE AND ENGINEERING

Proceedings of the Workshop on Advances of the Material Science and Engineering 2023

ADVANCES OF THE MATERIAL SCIENCE AND ENGINEERING

Proceedings of the Workshop on Advances of the Material Science and Engineering 2023

Editors

Aniruddha Mondal

Rabindra Nath Barman

Tushar Kanti Bera

Arindam Biswas

NEW DELHI PUBLISHERS

New Delhi, Kolkata

Advances of the Material Science and Engineering by Aniruddha Mondal, Rabindra Nath Barman, Tushar Kanti Bera, Arindam Biswas published by New Delhi Publishers, New Delhi.

First Edition: 2023

ISBN: 978-81-19006-98-4 (ebook)

New Delhi Publishers
90, Sainik Vihar, Mohan Garden, New Delhi – 110 059
Tel: 011-23256188, 9971676330
E-mail: ndpublishers@gmail.com
Website: www.ndpublisher.in

Branch Office
216 Flat-GC, Green Park,
Narendrapur, Kolkata – 700103

राष्ट्रीय प्रौद्योगिकी संस्थान दुर्गापुर
(शिक्षा मंत्रालय, भारत सरकार के अधीन राष्ट्रीय महत्व का संस्थान)
NATIONAL INSTITUTE OF TECHNOLOGY DURGAPUR
(An Institute of National Importance under Ministry of Education, Govt. of India)

प्रो. अरविन्द चौबे / Prof. Arvind Choubey, निदेशक / Director

Ref. No. : NITD/05/06/2023 **Date :** 13.09.2023

DIRECTOR'S DESK

It gives me immense pleasure that Dept. of Physics, Dept. of Mechanical Engineering and Dept. of Electrical Engineering, NIT Durgapur is organizing a workshop on **""Advances of The Material Science and Engineering" during 22.09.2023 to 24.09.2023 in hybrid mode** with the collaboration of Queen's University, Canada and A.N. Frumkin Institute of Physical Chemistry & Electrochemistry, Moscow, Russia funded by **Scheme for Promotion of Academic and Research Collaboration (SPARC), Ministry of Human Resources & Development (MHRD), Government of India.** This workshop will enhance the knowledge of students, faculty members and researchers to engage in active research. The students and faculty will get chance to interact with International faculties like Prof. Dr. Jean Michel Nunzi, Queen's University, Canada; Prof. Dr. Aleksei Tameev, Higher School of Economics (National: Research University), Russia. Medical diagnostics to prevent or monitor disease can now be performed much more readily due to the availability of a wide variety of measurable analytes, greater test sensitivity, and an increase in the informative value of the data obtained. There is a demonstrated need for inexpensive, easy-to-operate medical diagnostic tools that are maintenance-free and/or disposable. Miniaturization of diagnostic tools can provide this type of personal healthcare testing, which is referred to as Point-of-Care, or POC-testing. POC-testing can provide the diagnostic services that previously required several steps, highly skilled personnel and expensive equipment. POC devices can detect medical markers using several detection principles: chemical recognition, optical interaction, conductivity or capacitance change. The field effect transistors (FETs) is a most important device for the above aspect. The FET can be used to determine the dangerous gasses in air at industrial areas and heavy metals into water. The monitoring of gasses like CO_x, NO_x, Methane etc., is required a gas sensor. Also monitoring of heavy metals in rural areas like Bankura, Purulia and Birbhum (West Bengal) is required for health issues. The FET device can work on the changes of electrical conductivity (changes of dielectric properties of the active medium) due to presence of such gasses and heavy metals in the environment and water respectively. Therefore low cost hybrid materials is to be synthesized for the development of the FET sensor.

As I have been told the speakers will deliver lectures on the mechanism of synthesis of different smart and hybrid materials for the development of the more sustainable devices.

I extend my best wishes and commitment to support the activity and similar such activities at NIT Durgapur.

13/09/2023

(Prof. Arvind Choubey)
Director
NIT Durgapur

E-mail : director@nitdgp.ac.in, Website : www.nitdgp.ac.in
महात्मा गाँधी एवेन्यू, दुर्गापुर - 713209, भारत / Mahatma Gandhi Avenue, Durgapur - 713209, India
टेल/Tel. No.- +91-343-254 6397, फैक्स/Fax No.- +91-343 254 7375

Preface

The Scheme for Promotion of Academic and Research Collaboration (SPARC) aims to improving the research ecosystem of India's Higher Educational Institutions by facilitating academic and research collaborations between Indian Institutions and the best institutions in the world from 28 selected nations to jointly solve problems of national and/or international relevance.

The scheme proposes to enable productive academic co-operation by supporting the following critical components that can catalyze impact making research, namely:

Visits and long-term stay of top international faculty / researchers in Indian institutions to pursue teaching and research

Visits by Indian students for training and experimentation in premier laboratories worldwide

Joint development of niche courses, world-class books and monographs, translatable patents, demonstrable technologies or action research outcomes and products

Consolidation of Bilateral co-operation through academic and research partnerships through Indo-X Workshops in India

Publication, Dissemination and Visibility through a high profile annual international Conference in India

The expected outcomes include tangible results in terms of large quantity of high quality research publications, solution to key national and international problems, development of niche courses, high quality text books and research

monographs, imbibing of best practices from top international academicians and researchers, strong bilateral co-operation, and improved world reputation and ranking of Indian Institutions.

Objectives

SPARC aims at improving the research ecosystem of India's higher educational institutions by facilitating academic and research collaborations between Indian institutions and the best institutions in the world from 28 selected nations to jointly solve problems of national and international relevance in the first phase.

Under this Scheme, 600 joint research proposals will be awarded for 2 years to facilitate research collaboration between Indian research groups with the best in class faculty and renowned research groups in the leading universities of the world, in areas that are at the cutting edge of science or with direct social relevance to the mankind, specifically India.

In order to facilitate fundamental and socially relevant research in India, lot of emphasis is being laid to strengthen collaboration between Indian Research groups with Top research groups in the world, so that Indian scientists and students can interact with the finest minds in the world. With this objective in mind, MHRD (Ministry of Human Resource Development, Government of India) in 2015 launched GIAN (Global Initiative of Academic Networks), under which an International academician can visit an Indian Institute for two weeks to offer a course. The response was overwhelming, as apart from the course the Indian students and academicians got a chance to interact with the International Faculty. In the meantime, DST (Department of Science & Technology, Government of India) came up with another unique program in 2017, VAJRA (Visiting Advanced Joint Research), under which an International Scientist of Repute can spend longer duration in the country. However, it was realized that maximum benefit of a collaboration can be harvested only when the Indian Research group, particularly the students can be physically exposed to the world class research facilities and equipment available with Top international groups in their respective Institutes. As of now, such travel opportunities are limited, as there are no formal program that generously support student visit for longer periods.

SPARC proposed to fill up this void in the collaboration eco system, as it not only funds for long term visit by the International Faculty (2 to 8 months) but

would also fund the travel and sustenance of Indian students at the University/ Institute of the International collaborator. The program aims at exposing large number of young students, the torch bearers of the future generation, to state of art developments in science, thereby increasing the number of highly trained scientific manpower in the country, as well as significantly enhance the visibility of Indian Science and Scientists in the world map of highly competitive cutting edge science. It is expected that some of the joint ideas would not only lead to breakthrough in science, but would also result in sustainable technological products that will be beneficial to mankind at large, in addition to fulfilling the need of India.

The major outcome of the SPARC initiative will be strong research collaboration between Indian Research groups with top research group in the leading Universities of the world, in areas that are at the cutting edge of science or with direct social relevance to the mankind, specifically India. The strong joint research should lead to tangible result that should include large number of high quality research publications, solution to key national and international problems, development of niche courses, high quality text books and research monographs, imbibing of best practices from top international academicians and researchers, strong bilateral co-operation, and improved world reputation and ranking of Indian Institutions.

The scheme proposes to enable productive academic co-operation by supporting the following critical components that can catalyse impact doing research, namely:

- Visits and long-term stay of top international faculty/researchers in Indian institutions to pursue teaching and research.
- Visits by Indian students for training and experimentation in premier laboratories worldwide.]
- Joint development of niche courses, world-class books and monographs, translatable patents, demonstrable technologies or action research outcomes and products.
- Consolidation of Bilateral co-operation through academic and research partnerships through Indo-X Workshops in India.
- Publication, Dissemination and Visibility through a high profile annual international Conference in India

The content of the book has been taken from the workshop "Advances of the Material Science and Engineering 2023", which will explore a detailed discussion on the design and development of the hybrid materials and related devices for the sustainability of the environment. An introduction to the various basic research on sensors, energy harvesting devices and solar cells using organic, inorganic, polymer and composite materials has also been discussed.

Editors

Contents

Section 2: Materials and Devices

Section 3: Sustainability and Energy

Section 4: Instrumentation and Measurement

List of Contributors

Abhijit Das, Department of Electronics and Communication Engineering, National Institute of Technology Agartala (NITA) Jirania, West Tripura, Tripura 799046, INDIA

Ajit Kumar Meikap, Department of Physics, National Institute of Technology Durgapur , Mahatma Gandhi Avenue, A-Zone, Durgapur, West Bengal 713209, INDIA

Alexey Tameev, Frumkin Institute of Physical Chemistry and Electrochemistry, RAS, Moscow 119071, Russia, e-mail: a.tameev@gmail.com

Amiya Samanta, Centre for Biomedical Engineering and Assistive Technology (BEAT), NIT Durgapur, West Bengal 713209, INDIA, Department of Civil Engineering, NIT Durgapur, West Bengal 713209, INDIA

Anand Raj, 4MTech Student, Department of Civil Engineering, National Institute of Technology Durgapur, Mahatma Gandhi Avenue, A-Zone, Durgapur, West Bengal 713209, INDIA

Anikesh Kumar Singh, Department of Electronics and Communication Engineering, National Institute of Technology Agartala (NITA) Jirania, West Tripura, Tripura 799046, INDIA

Aniruddha Mondal, Department of Physics, National Institute of Technology

Durgapur (NITDgp), Mahatma Gandhi Avenue, A-Zone, Durgapur, West Bengal 713209, INDIA

Ankita Choudhury, Department of Physics, National Institute of Technology Durgapur (NITDgp), Mahatma Gandhi Avenue, A-Zone, Durgapur, West Bengal 713209, INDIA

Anurup Chakraborty, Department of Physics, National Institute of Technology, Durgapur, 713209, WB, India ac.21ph1101@phd.nitdgp.ac.in

Arijit Kumar Banerji, Department of Civil Engineering, Dr. B. C. Roy Engineering College Durgapur, Jemua Road, Fuljhore, Durgapur, West Bengal 713206, INDIA

Arindam Biswas, School of Mines and Metallurgy, Kazi Nazrul University, Asansol, West Bengal-713340, India e-mail: mailarindambiswas@yahoo.co.in

Arjun Dey, Thermal Systems Group, U.R. Rao Satellite Centre, Indian Space Research Organisation, Bangalore 560017, Karnataka, India

Arka Dey, Department of Physics, National Institute of Technology Durgapur (NITDgp), Mahatma Gandhi Avenue, A-Zone, Durgapur, West Bengal 713209, INDIA

Ashishkumar R. Kale, Department of Chemical Engineering, National Institute of Technology Durgapur.West Bengal, India.

Askand Kumar, Department of Mechanical Engineering, National Institute of Technology Durgapur (NITDgp), Mahatma Gandhi Avenue, A-Zone, Durgapur, West Bengal 713209, INDIA

Bhakta Kunwar, Department of Physics, Nar Bahadur Bhandari Government College, Gangtok, Sikkim, 737102, INDIA

Bibek Chettri, Department of Physics, Sikkim Manipal Institute of Technology, Majhitar, Rangpo, Sikkim, 737136, India.

Bikash Sharma, Department of Electronics and Communication Engineering., Sikkim Manipal Institute of Technology, Majhitar, Rangpo, Sikkim, 737136, India

Bimal Das. Department of Chemical Engineering, National Institute of Technology Durgapur. West Bengal, India.

Chanchal Das, Department of Civil Engineering, Dr. B. C. Roy Engineering College Durgapur, Jemua Road, Fuljhore, Durgapur, West Bengal 713206, INDIA

Chandan Kumar Bharti, Department of Mechanical Engineering, National Institute of Technology Durgapur (NITDgp), Mahatma Gandhi Avenue, A-Zone, Durgapur, West Bengal 713209, INDIA

Chandan Kumar Bharti, Department of Mechanical Engineering, National Institute of Technology Durgapur (NITDgp), Mahatma Gandhi Avenue, A-Zone, Durgapur, West Bengal 713209, INDIA

Chandan Kumar Raul, Department of Physics, National Institute of Technology Durgapur , Mahatma Gandhi Avenue, A-Zone, Durgapur, West Bengal 713209, INDIA

Debashis Podder, Department of Production Engineering, National Institute of Technology Agartala (NITA)

Deepshikha Datta , Department of Chemistry, Brainware university Barasat, Kolkata, West Bengal, India.

Dinesh Singh, Department of Mechanical Engineering, National Institute of Technology Durgapur (NITDgp), Mahatma Gandhi Avenue, A-Zone, Durgapur, West Bengal 713209, INDIA

Gaurav Kumar, MTech Student, Department of Civil Engineering, National Institute of Technology Durgapur Mahatma Gandhi Avenue, A-Zone, Durgapur, West Bengal 713209, INDIA

Geeta Verma, Department of Mechanical Engineering, National Institute of Technology Durgapur (NITDgp), Mahatma Gandhi Avenue, A-Zone, Durgapur, West Bengal 713209, INDIA

Iman Biswas, Department of Physics, National Institute of Technology Durgapur (NITDgp), Mahatma Gandhi Avenue, A-Zone, Durgapur, West Bengal 713209, INDIA

Jay Chandra Dhar, Department of Electronics and communication engineering, National Institute of Technology Nagaland , Dimapur, Nagaland,797103, INDIA

Jean-Michel Nunzi, Queens University, Kingston, Ontario K7L 3N6, Canada, e-mail: nunzijm@queensu.ca

Koyndrik Bhattacharjee1, 1Department of Civil Engineering, Dr. B. C. Roy Engineering College Durgapur, Jemua Road, Fuljhore, Durgapur, West Bengal 713206, INDIA

Md. Hamjala Alam1, 1Department of Civil Engineering, Dr. B. C. Roy Engineering College Durgapur, Jemua Road, Fuljhore, Durgapur, West Bengal 713206, INDIA

Michael Cholines Pedapudi, Department of Electronics and communication engineering, National Institute of Technology Nagaland

Mitra Barun Sarkar, Department of Electronics and Communication Engineering, National Institute of Technology Agartala (NITA) Jirania , West Tripura Pin - 799046, INDIA

Nagendra Kumar, Department of Mechanical Engineering, National Institute of Technology Durgapur (NITDgp), Mahatma Gandhi Avenue, A-Zone, Durgapur, West Bengal 713209, INDIA

Nitesh Kumar Choudhary, Department of Mechanical Engineering, National Institute of Technology Durgapur (NITDgp), Mahatma Gandhi Avenue, A-Zone, Durgapur, West Bengal 713209, INDIA

Nitesh Kumar Choudhary, Department of Mechanical Engineering, National Institute of Technology Durgapur (NITDgp), Mahatma Gandhi Avenue, A-Zone, Durgapur, West Bengal 713209, INDIA

P. Chinnamuthu, Department of Electronics and Communication Engineering, National Institute of Technology Nagaland, India

Pinaki Ranjan Das, Department of Electrical Engineering, Ramgarh Engineering College, Jharkhand 825101, INDIA, Centre for Biomedical Engineering and Assistive Technology (BEAT), NIT Durgapur, West Bengal 713209, INDIA

Prasanna Karki, Department of Physics, Sikkim Manipal Institute of Technology, Majhitar, Rangpo, Sikkim, 737136, India.

Pronita Chettri1, Department of Physics, Sikkim Manipal Institute of Technology, Majhitar, Rangpo, Sikkim, 737136, India.

Rabindra Nath Barman, Department of Mechanical Engineering, National Institute of Technology Durgapur (NITDgp), Mahatma Gandhi Avenue, A-Zone, Durgapur, West Bengal 713209, INDIA

Rajib Kumar Nanda, Department of Electronics and Communication Engineering, National Institute of Technology Agartala (NITA) Jirania , West Tripura Pin - 799046, INDIA

Ratnesh Kumar, Assistant Professor, Mechanical Engineering Department, National Institute of Technology, Durgapur713209, India

Rituparna Bhattacharya, Department of Electronics and Communication Engineering, National Institute of Technology Agartala (NITA), Jirania, West Tripura, Tripura 799046, INDIA

S.J.Chatterjee, Department of Mechanical Engineering, National Institute of Technology Durgapur (NITDgp), Mahatma Gandhi Avenue, A-Zone, Durgapur, West Bengal 713209, INDIA

S.Karmakar, Department of Mechanical Engineering, National Institute of Technology Durgapur (NITDgp), Mahatma Gandhi Avenue, A-Zone, Durgapur, West Bengal 713209, INDIA

Sanat Kumar Das, Department of Physics, Sikkim Manipal Institute of Technology, Sikkim Manipal University, Sikkim, India, E-mail: sanat.d@smit.smu.edu.in / dassanat707@gmail.com

Sanku Konai, Assistant Professor, Department of Civil Engineering, National Institute of Technology Durgapur, Mahatma Gandhi Avenue, A-Zone, Durgapur, West Bengal 713209, INDIA

Satabdi Saha, Civil Engineering Department, Elitte College of Engineering Karnamadhavpur, Ghola, Sodepur, Kolkata, West Bengal 700113, INDIA

Saurabh Chhipa, Department of Mechanical Engineering, National Institute of Technology Durgapur (NITDgp) Mahatma Gandhi Avenue, A-Zone, Durgapur, West Bengal 713209, INDIA

Shubhajit Vishwas, Department of Electronics and Communication Engineering, National Institute of Technology Agartala (NITA) Jirania , West Tripura Pin - 799046, INDIA

Soumen Basu, Department of Physics, National Institute of Technology Durgapur , Mahatma Gandhi Avenue, A-Zone, Durgapur, West Bengal 713209, INDIA

Soumendu Gorai, Department of Mechanical Engineering, National Institute of Technology Durgapur (NITDgp), Mahatma Gandhi Avenue, A-Zone, Durgapur, West Bengal 713209, INDIA

Subhadeep Saha, Ph.D. Scholar, Mechanical Engineering Department, National Institute of Technology, Durgapur713209, India, ss.22me1109@phd.nitdgp.ac.in

Subrata Saha, Department of Physics, National Institute of Technology Durgapur (NITDgp), Mahatma Gandhi Avenue, A-Zone, Durgapur, West Bengal 713209, INDIA

Sudem Daimary, Department of Electronics and communication engineering, National Institute of Technology Nagaland , Dimapur, Nagaland,797103, INDIA

Sujit Karmakar, Department of Mechanical Engineering, National Institute of Technology Durgapur (NITDgp), Mahatma Gandhi Avenue, A-Zone, Durgapur, West Bengal 713209, INDIA

Sujoy Chakraborty, Department of Production Engineering, National Institute of Technology Agartala (NITA)

Sunil Kumar Choudhary, National Institute of Technology Durgapur, Durgapur, West Bengal 713209, India, Dr. B. C. Roy Engineering College, Durgapur, West Bengal 713206, India

Sushmita Kumari, Former MTech Student, Department of Civil Engineering, National Institute of Technology, Rourkela, Odisha 769008, INDIA

Tushar Kanti Bera, Centre for Biomedical Engineering and Assistive Technology (BEAT), NIT Durgapur, West Bengal 713209, INDIA, Department of Electrical Engineering, NIT Durgapur, West Bengal 713209, INDIA

Uttam Kumar Mandal, Department of Production Engineering, National Institute of Technology Agartala (NITA)

Section 1

Abstracts of the Invited Talk

1

Solar Cell Thin Films: Organic and Perovskite Devices

Jean-Michel Nunzi

Solar cell thin films: organic and perovskite devices Photovoltaic is among the most propitious renewable energy sources for meeting global energy demands. I will review the basic principles of solar cell function using organic solar cells as a case study. This will be illustrated by approaches to advance the stability, including the control over morphology, absorption coefficient, charge carrier mobility and lifetime, exciton lifetime, exciton binding energy and dissociation. Furthermore, owing to their simple solution synthesis procedure, lightweight, wearable, power conversion efficiency, ready to deploy for extreme lightweight, and reduced cost of constituent materials, perovskite solar cells have received huge interest in the past years. Because of the high-quality perovskite film attained by low-temperature fabrication methods, as well as the development of appropriate interface and electrode materials, the effectiveness of perovskite solar cells (PSCs) has topped 25% efficiency in recent years. Additionally, perovskite solar cells' stabilization has received a lot of well-deserved recognition. The future of various carbon, tin, and polymer materials-based perovskite solar cells will be explored, and their industrial expansion possibility discussed. This review will summarize important accomplishments to date and highlight the problems that must be overcome for perovskite solar cells to be developed and commercialized successfully.

Nonlinear Optics: basic principles and their application to organic materials

Since the discovery of lasers, nonlinear optics has emerged as an active field of research. Indeed, on the one hand, it is a powerful spectroscopic tool for the characterization of materials, and on the other hand, it is a promising area for future technologies. This is justified by the possibilities offered by light as an information carrier, as evidenced by its widespread use for communications, image processing and data storage. This naturally led to a systematic investigation of the possibilities offered by nonlinear optics as an information processing tool, with potential advantages such as lossless and high data-rate transmission, high parallelism, and immunity to parasites. To permit such achievements within adequate efficiency and speed conditions, tremendous work has been performed on the elaboration and characterization of new materials for second and third-order nonlinear optics. Numerous possibilities to get large and fast nonlinearities, including the use of electromagnetic confinement in waveguides, Fabry-Perot etalons or metallic micro-structures, and the use of quantum confinement in semiconductors and quantum-dots. Organic materials are among the promising materials owing to large oscillator strengths as evidenced with dyes and stains. Their nonlinear optical response, due principally to the high polarizability of delocalized electrons depends strongly on the conjugation length. With respect to other materials, they have some advantages related to their ease of processing and compatibility with other technologies. Organics are also versatile materials; For instance, the same or slightly modified molecules can be processed as crystals, or used for either solution cast, vacuum evaporated, epitaxy, etc. They may be also used as solutions, gels, glasses or guest-host composites with various shapes. Additionally, various molecular engineering rules exist to tune their linear and nonlinear optical properties, including absorption strengths and excited-state dynamics.

2

Polymer Semiconductors in Thin Film Devices

Alexey Tameev

Polymers are widely used to investigate basic science problems and develop electronic and photonic devices. Of greatest interest are polymer materials that exhibit electric conductivity, photoconductivity or electroluminescence and are capable of forming thin film.

The report presents experimental methods for studying the electrical properties of polymer films (four-probe technique, SCLC, Hall effect), photogeneration efficiency and mobility of charge carriers in photoactive polymers and donor-acceptor composites (time-of-flight, CELIV, constant photocurrent, electrophotography). The corresponding mechanisms of the charge generation and transport are also discussed. Finally, traditional electronic devices (photodiode, LED, photovoltaic cell, field-effect transistor) and the basic processes that ensure their operation are reviewed.

Electrical conductivity in composites with nanoparticles and quantum dots

Hybrid organic-inorganic composites are of interest due to the combination of the physical effects of nanoscale structures with the relatively simple preparation of thin films. Photoactive and charge transfer layers are key functional layers in thin film electronic devices such as solar cells, photodetectors,

light emitting diodes, etc. For example, exploiting the photonic properties of nanoscale particles is one of the trends in developing approaches to create the photovoltaic (PV) effect. Metal nanoparticles (NPs) and quantum dots (QDs) are known attractive materials in this regard.

The report presents the electrical properties of hybrid composites including plasmonic Au NPs, PbS QDs, core-shell platelets, Si NPs providing improved electrical conductivity, photoconductivity, electroluminescence, and discusses the corresponding mechanisms.

3

Design and Development of Gallium Nitride Based Terahertz Solid-State Sources

Arindam Biswas

The terahertz (THz) frequency band popularly called 'terahertz-gap' lies between the millimetre and infrared regions of the electromagnetic spectrum and is defined as the frequency range of 0.1 – 10 THz or the wavelength range of 3.0 – 0.03 mm. This particular frequency band is in great demand for various applications such as short-range terrestrial and airborne communication, space-based communication, bio-imaging, spectroscopy, bio-sensing, quality inspection in various industrial branches, medical and pharmaceutical applications, THz astronomy, etc. The wide bandwidth of THz spectrum can be useful for broadband wireless communication providing data rate of tens of Gbps (gigabytes per second). The generation of terahertz signal with appreciable power is a challenging area of research. In recent years the research and development of suitable solid-state sources capable of generating high power in the Terahertz frequency regime (0.1 – 10 THz) is underway throughout the world. Notwithstanding the tremendous application potential of THz frequency band, this field has not yet been fully exploited since it is difficult to develop reliable solid-state sources capable of generating, detecting, and processing the terahertz signal with sufficient power required for system application. Some THz sources such as electron beam sources, optically pumped far-infrared gas

lasers, Semiconductor Quantum Cascade Lasers (QCL), Resonant Tunnelling Diode (RTD), TUNNETT diode, Gunn diode, high electron mobility transistors (HEMTs), and heterojunction bipolar transistors (HBTs) etc. are reported in the literature. But these sources have several limitations as regards their compactness, cost, output power and efficiency. Most of the available THz sources are complex and bulky. These limitations can be overcome if IMPATT diodes are used as THz sources.

REFERENCES

Arindam Biswas, Sayantan Sinha, Aritra Acharyya, Amit Banerjee, Srikanta Pal, Hiroaki Satoh & Hiroshi Inokawa, "1.0 THz GaN IMPATT Source: Effect of Parasitic Series Resistance", Journal of Infrared, Millimeter, and Terahertz Waves39, 954 (2018).

Sahnawaj Khan, Aritra Acharyya, Hiroshi Inokawa, Hiroaki Satoh, Arindam Biswas, Rudra Sankar Dhar, Amit Banerjee, A. Y. Seteikin, "Terahertz Radiation from High Electron Mobility Avalanche Transit Time Sources Prospective for Biomedical Spectroscopy", Photonics, Vol 10, pp. 800 (2023).

4

Designing of GLAD Based Metal Oxide and Hybrid Heterostructures for Photodetector Application

Jay Chandra Dhar

Glancing angle deposition (GLAD) is a flexible nanofabrication technique that accurately controls the growth of nanostructures by depositing material at an oblique angle, enabling the creation of unique and customizable metal oxide nanoarchitectures for various applications. Metal oxide based high-efficient photodetectors (PDs) with axial heterostructures of 3-D and/or 1-D morphologies. In the present scenario, p-n junction heterostructure nanowire is a recent advanced structure for the superior PD due to the strong built-in electric field in the junction which can efficiently separates the charge carriers. One-dimensional (1D) axial n-ZnO/p-CuO (1D/1D) heterostructure (HS) nanowires (NWs) using glancing angle deposition (GLAD) technique incorporated RF/DC magnetron sputtering system was performed for high performance PD application. The fabricated 1D-1D HS NW based PD shows an extremely high rectification ratio of ~1200 and a low dark current of 0.09 nA with a rise time of ~0.49 ms and a fall time of ~0.11 ms using white light illumination. Moreover, under the UV light illumination the fabricated PD was performed and exhibited high responsivity (R), detectivity (D*) and as low as noise equivalent power (NEP) of ~0.148 A/W (at 380 nm), 0.05 TJone and 70 pW respectively at +3V bias. As a result, the authors have developed a

unique axial p-n-junction HS NWs (n-ZnO/p-CuO) array-based PD produced through a catalytic free glancing angle deposition (GLAD) approach, taking into account all of the aforementioned benefits which can be a good candidate for PD application.

Similarly, UV PDs based on β-Ga2O3/NiO (1D-1D) HS and β-Ga_2O^3/p-si (1D-3D) HS was fabricated on p-type Si substrate using the same GLAD technique with in the RF/DC sputtering chamber. The absorption is maximum for 1D-1D (β-Ga_2O_3/NiO NW HS) structure than that of the 1D-3D structure (β-Ga_2O_3/p-si HS) due to its atomically sharp interface and superior light harvesting capability. On comparing, the1D-1D HS UV PD showed a very high R of 185.25 A/W, D* of 3.86 1013 Jones, NEP of 8.70 10-14 W and EQE of 835.35% at a wavelength of 275 nm (UV-C). Moreover, 1D-1D HS UV PD showed faster response (with rise time and fall time of 0.11 s and 0.25 s respectively) than that of the 1D-3D HS UV PD and also found to be better than some of the recently reported UV PDs. Therefore, the large generation and fast separation of carriers at the strong interface between 1D-1D HS small NW axis makes the 1D-1D HS UV PD a good candidate for UV PD application.

The perovskite is the promising material for light sensing applications due to its higher power conversion efficiency made by its high optical absorption, long diffusion length and lower exciton binding energy. Hence, the authors here have reported perovskite-based photodetectors (PPDs) using the perovskite material $CH_3NH_3PbI_3$ with different metal oxide charge transport layers. The perovskite sandwiched between two carrier transport layers designed with the hybrid heterostructure of electron transport layer (ETL)/$CH_3NH_3PbI_3$/hole transport layers (HTL) showed better photoelectric parameters. The authors designed the PPDs with ZnO as ETL and NiO as HTL with 2-D (thinfilm (TF)) and 1-D (nanowire (NW)) morphologies using glancing angle deposition (GLAD) technique. The device with 1-D carrier transport layers showed broad band detection capability with enhanced device performance in both UV (390 nm) and visible (450 nm) respectively, under the bias voltages of -6 V. Moreover, the 1-D carrier transport layered device showed high response speed of ~ 200 ms. Furthermore, to detect the solar blind UV light (< 280 nm) in the self-powered mode, the authors designed the PPD with large bang gap β-Ga_2O_3 as ETL with the device structure of β-Ga_2O_3 NW/$CH_3NH_3PbI_3$/NiO NW and the devices showed a stunning performance in deep UV region of 275 nm. Hence, the designed perovskite based devices with metal oxide charge transport layers can be suitable candidates for both photodetection application devices.

5

Growth Technology for III–V–Nitride and III–V–Bismide– Bulk Layers: MSM Photodetectors

Sanat Kumar Das

III–V semiconductors containing small amounts of nitrogen and bismuth popularly known as "dilute nitrides and dilute bismides" respectively, have been of great interest since the beginning of the past decade. These materials are mostly being grown by the MBE and MOVPE techniques. Here I have shown the viability of a novel LPE technique for the growth of GaAsN, GaSbBi. GaAsN layers for the first time have been successfully grown by the liquid phase epitaxy technique from a GaAs + Ga + GaN melt with up to 2 mol% Li3N added to the same to act as a flux to promote nitrogen dissolution in Ga. X-ray diffraction study indicates a nitrogen content of 0.9 at. % in the material. 10 K photoluminescence measurements indicate a band gap reduction of 130 meV in the as-grown layers which increases to 150 meV after a high-temperature anneal. Energy dispersive X-ray measurements indicate incorporation of Li in the material and local vibrational modes related to both nitrogen and Li are observed through Raman spectroscopy. Furthermore, a photoluminescence peak at 1.33 eV is suggested to be due to Li. GaAsN layers were further used to fabricate photoconductive and MSM photodetectors with good photo response characteristics.

GaSbBi layers were grown by adding Bi to a GaSb growth melt and

characterized by HRXRD, EDX, PL and Raman spectroscopy. PL intensity increased after Bi addition and a decrease in the PL peak width is found after a high temperature anneal. As-grown material showed a band gap of reduction of up to 40 meV due to Bi incorporation which further increased to 49 meV after high temperature anneal. A maximum Bi incorporation of 0.4 at% was measured by EDX. Raman spectroscopy indicated that free Bi atoms are also introduced in the layer during growth. This again is the first successful report of the growth of GaSbBi using LPE technique.

6

Exploring the Wettability Applications: Glancing Angle Deposited Nanostructures

P. Chinnamuthu

Surfaces with a superhydrophilic wetting nature have been used in numerous applications such as anti-fogging, self-cleaning coatings and tissue reconstruction. Controlling the wettability of the surface is desirable in various technical applications. In recent years, efforts have been made to improve the hydrophilicity of thin films. There are works on improving hydrophilicity using UV illumination of metal oxide films such as TiO2, SnO2 and ZnO, either doping by metal or non-metal. However, there are limitations in applying these metal oxides for use as a reliable superhydrophilic coating and thus need to be checked. For practical application, the surface of the film cannot be illuminated with UV light all the time, and there is a need for long-lasting hydrophilicity in the absence of UV illumination for anti-fogging surfaces, specifically in outdoor applications. We have reported on designing vertical stacked coaxial TiO2-In2O3 heterostructure nanowire (NW), which studies photoinduced hydrophilicity after UV-illumination8. There are also reports on hydrophobic to hydrophilic conversion using surface derivatization, chemical grafting, wet chemical reactions, and modifying hydrophobic cross-linked high internal phase emulsion polymer (polyHIPE) using styrene9–11. Problems associated with these techniques are difficulties in implementation, high cost, polymer degradation possibility, and scale-up issues for large industrial production.

Here, we will discuss the synthesis of various nanostructures and focus on improving photo-induced wettability switching properties by examining the surface porosity, contact angle (CA), and surface energy.

7

Electrical Impedance Based Biological Tissue Health Monitoring and Disease Diagnosis: Technology, Challenges and Recent Trends

Tushar Kanti Bera

Electrical impedance is an inherent property of the biological tissues which can be noninvasively probed to study the body composition, anatomy and physiology. Electrical impedance analysis (BIA), electrical impedance cardiography (ICG), electrical impedance spectroscopy (EIS) and electrical impedance tomography (EIT) have been proven potential diagnostic tool which can be applied for disease detection line stroke, cancer, cardiac disease, pneumonia, and other infections and illness or health conditions. The BIA, ICG, EIS, are signal measurement techniques which could be noninvasively used for disease detection and treatment at low cost and with significant medical safety. Being a radiation free portable computed tomographic technique EIT works similarly to CT-Scanning but does not use X-Ray rather it uses an electrical current signal. EIT is found to be very fast, safe, portable, low cost, and other advantages and therefore it has been applied in biomedical engg., mechanical engg., chemical engg., civil engg., material engg., biotechnology, and many other fields of engineering and applied sciences. In recent days impedance based tissue characterization and health monitoring techniques have been proposed and studied for clinical technology and medical science domains. AI based medical

diagnostic tools are also being proposed and studied in recent days. Wearable instrumentation and wireless biomedical instrumentation with Internet of Things (IoT) technology are found advantageous in many applications. The Internet of Things (IoT) is the billions of physical devices around the world that are now connected to the internet, all collecting and sharing data through the internet. Therefore, the IoT technology can be utilized to enhance the possibility of providing healthcare facilities to the people from remote areas both in developed and underdeveloped countries. In this direction the EIT could be associated with the IoT technology to provide the medical imaging facilities to the patients from remote places for better medical diagnosis and treatment. The power of AI like Machine Learning has enabled us to interpret the medical imaging in the physical absence of doctors and clinicians which can help for diagnosing the diseases in pandemic and other critical medical situations like COVID-19 as well as for providing the healthcare services to the remote areas where the physical presence of the doctors and clinicians are not always available. In this talk the speaker will discuss about the electrical impedance based tissue characterization techniques for biomedical and medical applications. The technology, challenges and recent trends of the impedance based health monitoring technologies will be discussed in detail in the talk.

Section 2

Materials and Devices

8

Investigation of Optoelectronic Properties of Ni/MnO_2 Schottky Junction Device

Abhijit Das, Anikesh Kumar Singh and *Mitra Barun Sarkar*

Abstract

In this work, MnO2 nanorod (NR) array with Ni Schottky electrode were fabricated on silicon (Si) by electron beam evaporation method with the help of glancing angle deposition (GLAD). Field emission scanning electron microscope (FESEM) and Energy dispersive X-ray analysis (EDAX) confirms successful deposition of MnO_2 and formation of the MnO_2 NR array. The optical absorption characteristics illustrations the high absorption in visible region. Using Tauc plot, the optical bandgap was estimated as 2.5 eV. A significant enhancement of photocurrent was recorded with light illumination at the Ni/MnO2 schottky junction. Maximum value of photosensitivity was obtained as 31 at -2.7 V. The So the Ni/MnO_2 NR schottky junction device is a potential candidate for optoelectronics application.

Keywords – MnO_2, nanorod, optical absorption, tauc plot, photosensitivity.

1. INTRODUCTION

Synthesis and Characterization of one dimensional metaloxide nanostructures like nanowire, nanorod, nanotube etc., are deeply investigated due to their structure dependent mechanical, electrical and optical properties

[1-3]. Manganese dioxide (MnO_2) is a popular choice among metal oxide semiconductors since it is affordable, environmentally friendly, and naturally abundant [4-7]. Based on the connections between its fundamental octahedral structure, MnO_2 is an n-type transition metal oxide that can take many different forms [4, 8]. As a result, they exhibit a wide variety of crystal structures, and consequently, based on this, different properties are known to exist. Numerous techniques, including the hydrothermal approach, the sol-gel method, the wet chemical method, Physical vapor deposition method etc., were used to create MnO_2 nanostructures [5-9]. Even though many studies have been done on synthesizing MnO_2 made in various ways, there haven't been any done to make explicitly MnO_2 NR. Moreover, there are no study on using Ni electrode with MnO_2 to create a schottky contact to measure electrical responses. In this work, MnO_2 NR array were synthesized using the catalyst-free, cost effective glancing angle deposition (GLAD) approach, using the electron beam evaporation technique. With the help of Field Emission Electron Microscopy (FESEM) imaging the morphology and dimension of MnO_2 NR were examined. The Energy dispersive X-ray (EDAX) analysis was done to confirm the presence of as-deposited essential elements. The UV-Vis absorption characteristics were studied and using that the tauc plot was done to obtain the optical bandgap. The currentvoltage (I-V) characteristics under white illumination were examined to determine the optoelectronic parameters of the device. This research investigates the room-temperature light absorption and current-voltage characteristics (in presence of white light and dark condition) of the as-deposited MnO_2 NR utilizing Ni contacts.

2. EXPERIMENTS

A. Device Fabrication

On aStandard cleaned n-type <100> Si substrate (1×1 cm), the MnO_2 NR array structure were synthesized using an ebeam evaporator with GLAD (Hind High Vacuum com. pvt. ltd. The substrate holder was mounted at an angle of 85 degrees and 25 cm vertically away from the evaporation material (MnO_2) inside a vacuum chamber. We used nickel (Ni) for the metallization to make electrical contacts. To make the electrical contacts the samples were cover with shadow mask of ~1.5 mm diameter followed by evaporation of The Ni pellets. The schematic diagram of the fabrication setup and the proposed device structure are depicted in Figure-1 (a) and (b) respectively.

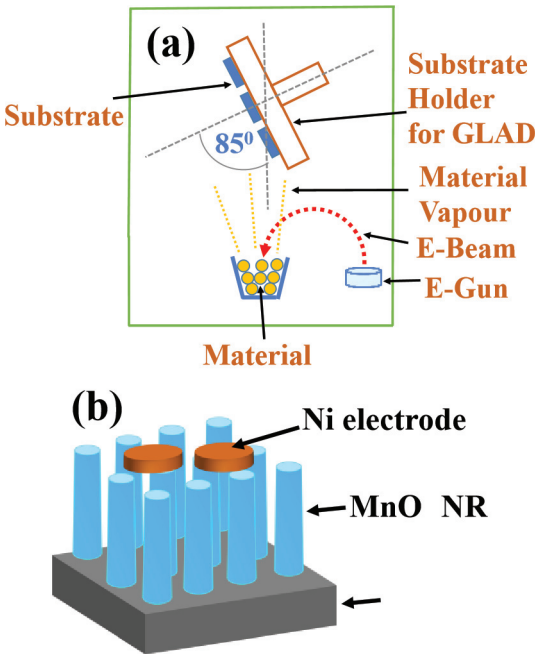

Figure-1: Schematic diagram: a) fabrication Unit, b) Device structure.

B. Characterization

The as-deposited MnO_2 NR samples were morphologically characterized by Field Emission Electron Microscopy (FESEM) (Carl ZEISS, Sigma). Furthermore, the MnO_2 NR samples were analyzed by Energy dispersive X-ray (EDAX) (Carl ZEISS, Sigma) to obtain information regarding the basic elements composing the sample. The photo absorption characteristics were obtained by UV-Vis spectrophotometer (Lamda 950, Perkin Elmer) for the visible range. The electrical measure measurements were recorded using an SMU (B2902A, Keysight).

III. RESULTS AND DISCUSSIONS

A. Morphological Analysis:

The surface morphology of the as-deposited MnO_2 NR array were analysed by FESEM image (tilted view) is depicted in Fig 2(a). The estimated average

length of the NR array is ~ 83 nm. The formation of NR array is mainly due shadowing effect that occurs in GLAD. In GLAD method, at first the incoming vapour flux is condensed and nucleated on the Si substrate surface. These nucleated materials forms separate islands due to shadowing effect [1, 6, 9]. As deposition progresses theses nucleated islands become larger in length normal to the surface. With further deposition, this method yields MnO_2 NR array on the Si substrate as depicted in Fig. 2 (a).

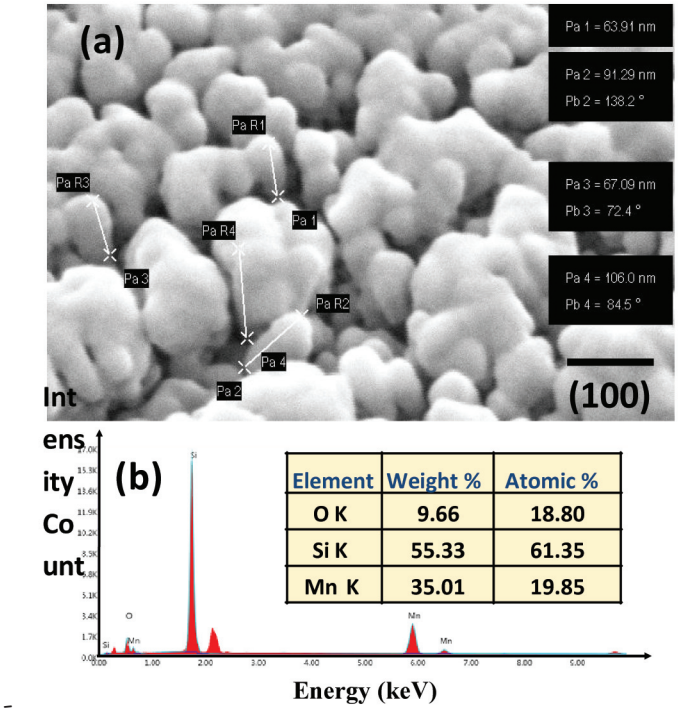

Figure-2: a) FESEM image (Tilted view) of MnO_2 NR, b) EDAX report.

It may be observed that all the NRs are not symmetrical in length and breadth. It occurs because in GLAD method due to competitive growth of material islands there forms unequal shadowing region. This results in few undergrown NRs [6, 9].

These undergrown NRs have much lesser dimension from the fully-grown NRs. The growth orientation of the NR array is vertically upwards from the Si substrate. The FESSM image is supporting our made-up structure. As an analytical method, EDAX is used to characterize the sample's elemental

composition as well as to map out its distribution within the area under investigation. The proportion of the composition of the MnO_2 NRs component constituents are shown in Fig. 2(b), which ensures the presence of Mn, O, Si.

B. Optical Absorption Analysis:

Optical analysis is carried out using UV-visible spectroscopy at room temperature. We deduced from the absorption spectrum (Fig. 3 (a)) that more amount of light absorption were took place for visible range. From the, absorption spectrum it can be seen that for the as-grown MnO_2 NR arrays the maximum optical absorption occurs at 287 nm.

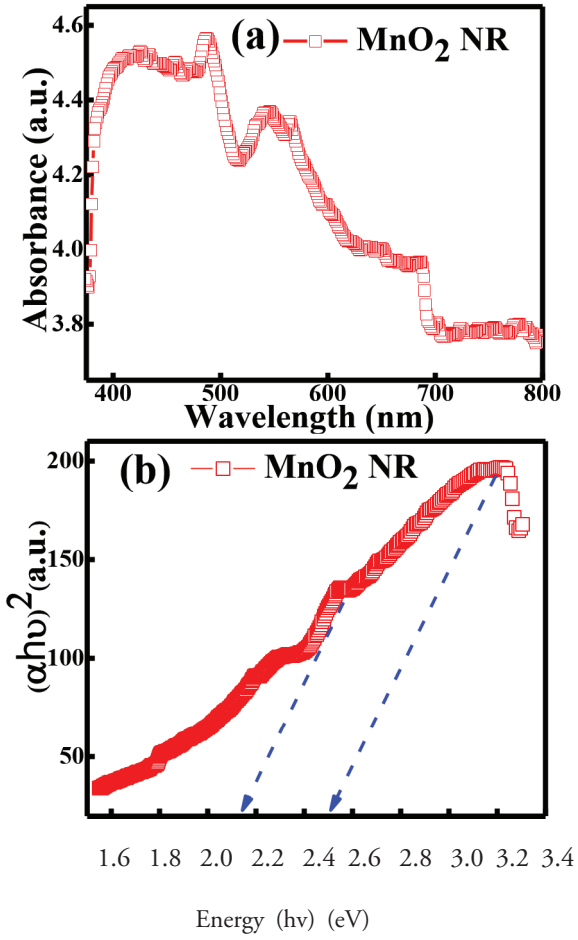

Figure-3: a) optical absorption characteristics, b) Tauc Plot.

The absorption spectra shows other peaks, which are caused by defects in NRs, which cause various hopping mechanisms in which electrons jump from one energy level to another [1011]. The optical bandgap was determined using the Tauc plot $((\alpha h\upsilon)^2$ vs. $(h\upsilon))$ method as shown in Fig. 3(b) , where where α = absorption coefficient, $h\upsilon$ = Incident light energy. The estimated main bandgap of MnO_2 NR was 2.5 eV. Another sub-bandgap of ~2.1 eV was found in the tauc plot, which corresponds to the electron transition from defect states [1011].

C.Electrical Response Analysis:

Fig. 4(a) displays the current vs. voltage characteristics of the as-deposited Ni/ MnO_2 NR device structures, which vary from - 10 to 10 V. The I-V graph displays rectifying behaviour, which suggests that a Schottky contact has formed between the Ni and the MnO_2 NR. Due to high amount of traps states at the surface NR, at dark situations have a lower dark current. Less intense dark currents show that surface states traps the carriers in the NR array. Additionally, the Schottky barrier forms a larger space charge region between Ni and MnO_2 NR results in and a decreased dark current[11,12]. Further, the MnO_2 NR device was inspected under dark and white light, which shows a good improvement in light-current than dark-current under reverse bias and forward bias. With forward biasing and under illumination on the device a huge amount of free electrons are produced because of light scattering of inside the vertically aligned nanorods arrays on the MnO_2 NR array device. The photogenerated electron-hole pairs greatly increases the number of majority carriers. This decreases the schottky barrier height, and increases the amount of photocurrent [13, 14]. While in reverse bias condition under white light illumination the hole trapping in Ni/MnO_2 interface plays key role in reverse current conduction due to reduction in depletion width. The Ni/MnO_2 NR interface has hugh amount of surface trap states due to the high stress of the NRs. These states traps holes from the valance band. Additionally, the light scattering of inside the vertically aligned NRs array structure rises the photo absorption and photo-generated charge carriers [13]. Hence, the depletion width at the Ni/MnO_2 NR interface is greatly lowered as which highly increases the value of photocurrent of the Ni/ MnO_2 NR device [14]. The photosensitivity of the device is calculated using Eq. 1 [11,12] as follows:

Photosensitivity = (Light Current - Dark Current)/ (Dark Current) …… (1)

The maximum photosensitivity of the device is found to be ~31 at -2.7 V (Fig. 4(c)). High amount of photo-current generation under light and reduction in depletion width results in high value photosensitivity of the device.

4. CONCLUSIONS

In conclusion, the MnO_2 NR array has been successfully synthesized on n-Si substrate using GLAD-assisted e-beam evaporation. The FESEM and EDAX analysis confirms the formation of the MnO_2 NR array on the Si substrate. Ni schottky contact has been fabricated on the MnO_2 NR array. The optical absorption analysis of the MnO_2 NR array reveals that the maximum light absorption occurs at 287 nm which falls under the visible range of light.

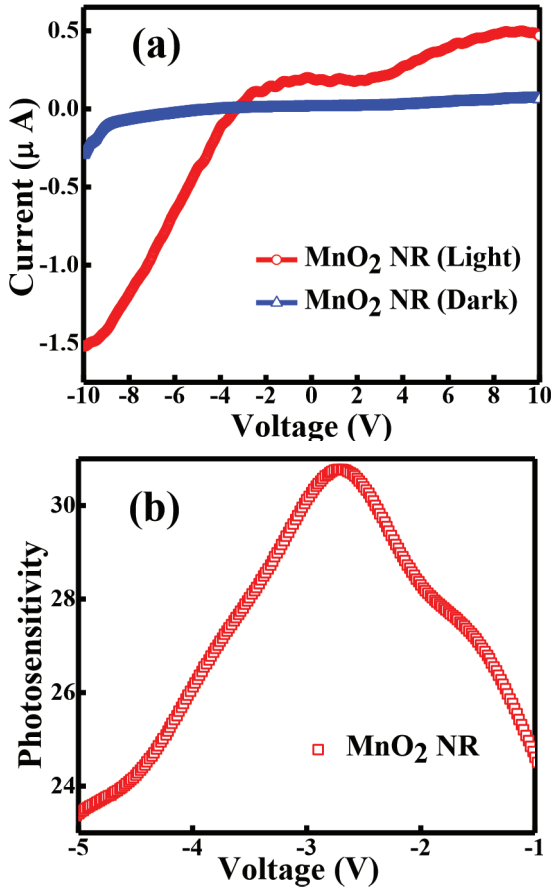

Figure-4: a) I vs. V characteristics (in light and dark condition), b) Photosensitivity Characteristics.

The estimated value of the bandgap from the tauc plot analysis is 2.5 eV. The currentvoltage characteristics of the Ni/ MnO_2 device were measured under white light illumination and dark conditions. There is a significant enhancement in the photo-current value which is mainly due to the presence of the huge amount of interfacial trap states and high absorption of light by multiple scattering in the MnO_2 NR array device. The maximum photosensitivity of the Ni/ MnO_2 device was recorded at -2.7 V, which mainly occurs due to a reduction in depletion width and enhancement in photocurrent. Therefore, the Ni/ MnO_2 NR array device may be very useful in next generation optoelectronics applications.

ACKNOWLEDGEMENT

We would like to express our gratitude to CIC, Tripura University for providing us the FESEM and EDAX facility and SAIF, IIT Madras for providing us the UV-Vis spectroscopy facility.

REFERENCES

1. Nath A., Mahajan B. K., and Sarkar M. B., "Ag nanoparticles sheltered
2. In_2O_3 nanowire as a capacitive MOS memory device," IEEE Trans. Nanotechnol., Vol. 19, 2020, pp. 856–863.
3. Zu X. et al., "Self-powered UV photodetector based on heterostructured
4. TiO_2 nanowire arrays and polyaniline nanoflower arrays," Synth. Met., Vol. 200, 2015, pp. 58–65.
5. Choudhuri B., Mondal A., and Saha A., "Enhanced photodetection from TiO_2-SiO_x-TiO_2 one-dimensional device," J. Electron. Mater.,Vol. 45, no. 8, 2016, pp. 4208–4214.
6. Jassem E. K., Majeed A. M. A. and Umran N. M. "The Effect of Temperature on Structural and optical properties of Manganese Oxide Nanoparticles," Journal of Physics: Conf. Series 1279 (2019), 012004 .
7. Wang Z., Wang F., Li Y., Hu J., Lu Y. and Xe M., "Interlinked multiphase Fe-doped MnO_2 nanostructures: a novel design for enhanced pseudocapacitive performance," Nanoscale, Vol. 8, No 13, 2016, pp. 7309-7317.
8. Lynrah S.A, Pooja P, Chinnamuthu P, "Scrutinizing and collating the broadband photo-detection properties of isotype n- MnO_2/TiO_2 nanostructure", IEEE Sensors Journal, vol. 21, no. 2, pp. 1485-1492
9. Brus V.V, Kovalyuk Z. D. and Maryanchuk P. D. "Optical Properties of

10. TiO2– MnO2 Thin Films Prepared by Electron Beam Evaporation", Technical Physics, 2012, Vol. 57, No. 8, pp. 1148–1151
11. M. A. Awad, N. M. A. Hadia, "Towards understanding the morphological, magnetic, optical and electrical properties of MnO_2 nanowires for magneto-and optoelectronic applications", J Mater Sci: Mater Electron, 29, P. No. 20695–20702.
12. Lynrah S.A, Chinnamuthu P , "Spectral response of the MnO_2 thin-film photodetector based at room Temperature", Materials Today: Proceedings,Vol. 68, 2022, P. No. 256-261.
13. Raman R., Nath A., Nanda R. K., Das A., Vishwas S. and Sarkar M. B., "Fast Response UV Detector by Vertically Allied ZrO_2 Nanowire Array Through Glancing Angle Deposition," IEEE Photonics Technology Letters, vol. 33, no. 12, 2021, pp. 631-634.
14. Pooja P. and Chinnamuthu P., "Robust Ultraviolet Photodetection by Tailored Polycrystalline In_2O_3 Nanowire Synthesized Using Glancing Angle Deposition," in IEEE Sensors Journal, vol. 21, no. 12, 2021, pp. 13192-13199.
15. Das A., Nath A., Pawar S., Singh N. K., Sarkar M. B., "Superior photosensing performance by Ag nanoparticles textured Al_2O_3 thin film based device," J Nanopart Res, Vol. 25, No. 5, 88 (2023).
16. Chinnamuthu P., Mondal A., Dhar J. C. and Singh N. K., "Visible light detection using glancing angle deposited TiO_2 nanowire arrays," Jpn. J. Appl. Phys. 54, 2015, 06FJ0.
17. Shougaijam B., Swain R., Ngangbam C. and Lenka T. R., "Enhanced Photodetection by Glancing Angle Deposited Vertically Aligned TiO_2 Nanowires," in IEEE Transactions on Nanotechnology, Vol. 15, No. 3, 2016, pp. 389-394.

9

Gadolinium Nanoparticle Sensitized TiO_2 Nanowires for Enhanced UV–Vis Absorption

Rajib Kumar Nanda, Shubhajit Vishwas, Mitra Barun Sarkar

Abstract

Gadolinium (Gd) nanoparticles (NPs) were synthesized by glancing angle deposition (GLAD) technique on titanium dioxide (TiO2) nanowires (NWs) over n-type Si substrate. The morphological analysis of the two distinct samples: bare-TiO2 NW and Gd NPs coated TiO2 NW samples, were performed using Field emission scanning electron microscopy (FESEM) and the corresponding energy dispersive x-ray spectroscopy (EDS). The top view and the tilted view of the samples obtained from FESEM reveal the presence of well-developed and densely packed vertical nanowires. The presence of all elements was confirmed by analysis of the EDS spectra. Based on the top diameter histogram analysis, the top diameter of the TiO2 NWs was determined to be 30.8 nm. A UV-Vis spectrophotometer was used to analyse the samples' optical properties. The absorbance of the Gd NPs coated TiO2 NW sample was 1.45-fold and 1.36-fold higher than that of the bareTiO2 NW sample in the UV and visible regions, respectively.

Keywords: Titanium dioxide, Gadolinium, Nanowire, Nanoparticle, GLAD, FESEM, UV-Vis absorption

INTRODUCTION

The constant pursuit of efficient and adaptable materials for optoelectronic applications has accelerated breakthroughs in disciplines ranging from photovoltaics and light-emitting devices to sensors and photodetectors. In this context, using nanomaterials to manipulate and control light-matter interactions has emerged as an appealing strategy for improving the performance of optoelectronic devices.

Metal oxide semiconductors possess notable advantages in terms of their exceptional stability and straightforward fabrication processes, making them highly suitable for the development of diverse optoelectronic devices. Nevertheless, these materials often encounter challenges, primarily characterized by their limited and sluggish photo response when exposed to light. Among the various metal oxides, titanium dioxide (TiO_2) holds a unique position due to its notable electrochemical characteristics, promising chemical durability, non-hazardous properties, and potential for commercial applications [1]. It is an n-type semiconductor material with a band gap of 3.2 eV in the anatase phase and 3.0 eV in the rutile phase. These properties, along with its high electron-transport characteristics, render it a promising material for various applications such as chemical sensors, photocatalysts, lithium batteries, solar cells, and photodetectors [2].

TiO_2 nanowires (NW), in particular, have garnered substantial attention for their remarkable characteristics, such as high surface-to-volume ratio, efficient charge transport, and tuneable bandgap [3]. However, their inherent limitations in absorbing light across the ultraviolet to visible (UV-Vis) spectrum have prompted the exploration of innovative strategies to extend their spectral absorption range and bolster their performance in diverse optoelectronic applications. One compelling strategy involves the incorporation of plasmonic metal nanoparticles (NPs) like Copper (Cu), Gold (Au), Silver (Ag) etc, onto semiconductor substrates, which has demonstrated success in improving light absorption by inducing localized surface plasmon resonances [4]. However, there is hardly any report available on the use of Gadolinium (Gd) NPs for enhancing optical absorption.

In this work, two distinct samples, bare-TiO_2 NW and Gd NPs coated TiO_2 NW, were synthesized on an n-type silicon (Si) substrate using a simple and inexpensive Glancing angle deposition (GLAD) assisted electron beam evaporation technique. Morphological analysis of the fabricated samples

was done by Field emission scanning electron microscopy (FESEM) and the corresponding energy dispersive x-ray spectroscopy (EDS). Optical analysis of the samples was done by UV-Vis spectrophotometer (Lambda 950, Perkin Elmer).

2. EXPERIMENTAL DETAILS

The GLAD technique was implemented inside the e-beam chamber in order to fabricate Gd NPs coated TiO_2 NW over ntype Si substrate. Before beginning the deposition process, the Si substrates were cleaned using the standard cleaning method Subsequently, they were dried and placed into the e-beam chamber. Initially, a layer of TiO_2 TF of 70 nm thick was deposited on top of the Si substrate. The TiO_2 TF serves as a seed layer, playing an important role in the nucleation and vertical growth orientation of the NW. The deposition was accomplished by evaporating 99.99% pure TiO_2 source materials (Ultrananotech Pvt Ltd). The substrates were positioned at a distance of 25 cm away from the source material. After that, TiO_2 NWs of length 350 nm and diameter ~30 nm was grown over the TiO_2 TF while the substrate was kept at an oblique angle of 85° with respect to the source. The substrate was also rotated azimuthally at a constant speed of 460 rpm. Subsequently, the same GLAD configuration, i.e., the same substrate rotation and orientation as used for TiO_2 NWs, was used to deposit Gd NPs (10 nm) on top of the TiO_2 NWs to synthesize the Gd NPs coated TiO_2 NW sample. All depositions mentioned above were conducted at a base pressure of 1×10^{-5} mbar. The growth rate remained constant at 0.12 nm/sec, which was monitored using a quartz crystal installed inside the chamber and a digital thickness monitor (DTM).

3. RESULTS AND DISCUSSION

A. Morphological Analysis:

Field emission scanning electron microscopy (FESEM) and the corresponding energy dispersive x-ray spectroscopy (EDS) (Carl Zeiss, Sigma) have been performed to examine the morphology of both the bare-TiO_2 NW sample and Gd NPs coated TiO_2 NW sample, as well as to confirm the presence of various elements on the samples. Figure-1(a) shows the tilted view and top view (inset) FESEM images of the bare-TiO_2 NW sample.

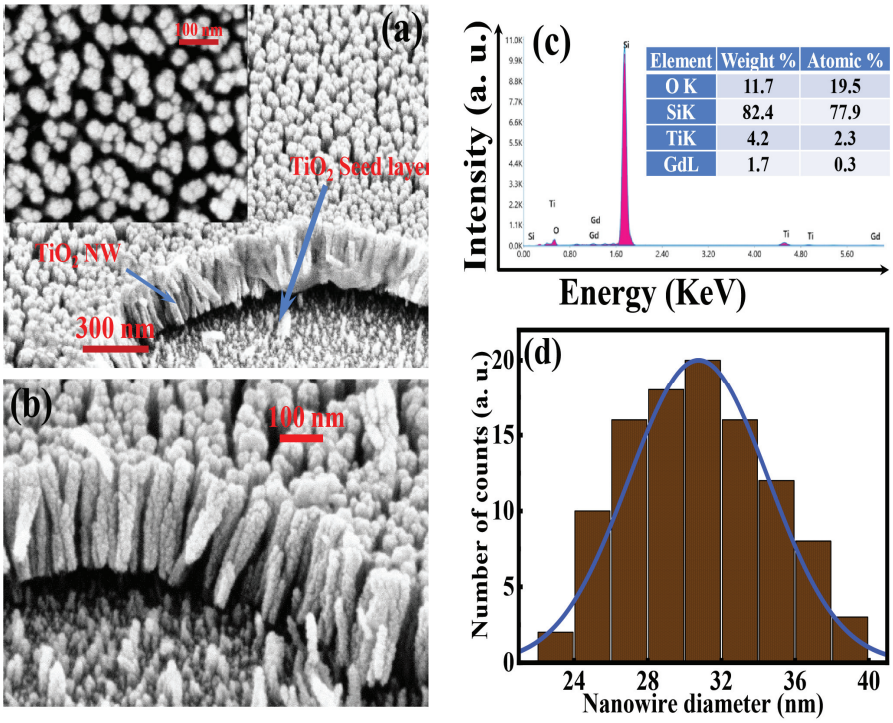

Figure-1: (a) Tilted view FESEM image of bare-TiO_2 NW sample (inset top view FESEM image of bare-TiO_2 NW), (b) Tilted view FESEM image of Gd NPs coated TiO_2 NW sample (c) EDS spectra of Gd NPs coated TiO_2 NW sample, and (d) top diameter histogram of bare-TiO_2 NW sample.

Figure-1(b) shows the tilted view of the Gd NPs coated TiO_2 NW sample, revealing the presence of Gd NPs on the surface of TiO2 NW. The top view and tilted view of the bare-TiO_2 NW sample show the formation of densely packed vertical NWs with an uneven surface. Figure-1(c) shows the EDS spectra of the Gd NPs coated TiO_2 NW sample. The samples exhibited the presence of molecules such as silicon (Si), titanium (Ti), oxygen (O), and gadolinium (Gd), as illustrated in Figure-1(c). The proportion of elements present in the sample was determined based on the specific scanning region of the sample (shown in the inset of Figure-2(c)). Aside from Si, Ti, O, and Gd, no other additional element peak has been identified. Furthermore, the EDS spectra indicated emissions from the Si K, Ti K, O K, and Gd L shells. The histogram for the TiO_2 NW top diameter is shown in Figure-1(d). The average top diameter of the TiO_2 NW is calculated to be 30.8 nm.

B. Optical absorption analysis:

Optical absorption studies using UV-Vis spectroscopy were conducted at ambient temperature for both the bare-TiO_2 NW sample and the Gd NPs coated TiO_2 NW sample within the wavelength range of 200 nm to 800 nm. Figure-2(a) shows the wavelength vs absorption plot for both the samples. An enhancement in absorption spectrum has been observed for the Gd coated TiO_2 NW sample as compared to bare-TiO_2 NW sample both in the UV and visible region.

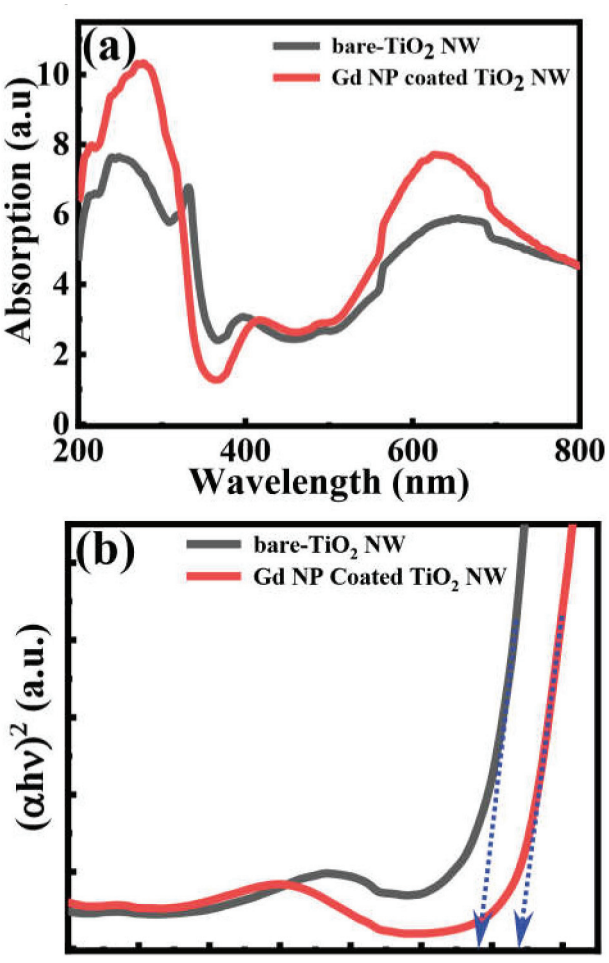

Figure-2: (a) Optical absorption spectroscopy, and (b) $(\alpha h\nu)^2$ versus bandgap energy

(E_g) plot of bare-TiO_2 NW and Gd NPs coated TiO_2 NW

The Gd NPs coated TiO_2 NW sample exhibits a 1.45-fold and 1.36-fold enhancement in absorption over the bare-TiO_2 NW sample in the UV region and visible region, respectively. The enhanced UV-Vis absorption observed in Gd NPs coated TiO_2 NW sample can be attributed to a phenomenon known as plasmon-enhanced absorption [5]. The addition of Gd NPs on the surface of TiO_2 NWs can cause localized surface plasmon resonances (LSPR). This plasmon resonance in Gd NPs may generate high electric fields in their proximity. These enhanced electric fields can extend into the surrounding TiO_2 NWs, increasing the probability of light interacting with the nanowires. This increased interaction boosts the absorption of UV and visible light by the TiO_2 NWs [6].

The bare-TiO_2 NW sample exhibits two broad absorption peaks centered at 248 nm and 654 nm in the UV and visible region, respectively. The addition of Gd NPs caused a red-shift of 30 nm in the absorption peak of the bare-TiO_2 NW sample in the UV region, and a blue-shift of 28 nm in the visible region. The peak broadening observed in both the samples may be attributed to the oxygen vacancies formed in the TiO_2 during synthesis [7]. Apart from that another sharp absorption peak is also observed in case of the bare-TiO_2 NW sample at 332 nm.

The bandgaps of both samples can be determined from the tauc-plot, employing the famous Tauc-equation (Eq. 1) [8].

$$(\alpha h\nu) = A\,(h\nu - E_g)^n \qquad \ldots\ldots (1)$$

Where α is the absorption coefficient, $h\nu$ is the photon energy. The factor ***n*** is determined by the type of electron transition (½ or 2 for direct and indirect band gaps, respectively).

Figure-2(b) shows the $(\alpha h\nu)^2$ vs. bandgap energy (E_g) plot for the bare-TiO_2 NW and Gd NP coated TiO_2 NW samples. The linear parts of the curves are extrapolated to the energy axis, yielding E_g of ~3.56 eV for the TiO_2 NW sample and ~3.67 eV for the Gd coated TiO_2 NW sample, which corresponds to the material's main bandgap transition [9]. This ~0.11 eV bandgap reduction in the Gd coated TiO_2 NW samples could be attributed to a changed dielectric

function at the interface of Gd NPs and TiO_2 NWs [10].

CONCLUSIONS

In this work, two distinct samples: bare-TiO_2 NW and Gd NPs coated TiO_2 NW, were synthesized on n-Si substrate by using GLAD assisted e-beam evaporation technique. The samples were then morphologically and optically characterized by FESEM and UV-Vis spectrophotometer. The study of the histogram for the top diameter indicated that the TiO_2 NWs have an average top diameter of 30.8 nm. The Gd coated TiO_2 NW sample showed an enhancement of 1.45-fold and 1.36-fold in absorption over the bare-TiO_2 NW sample in the UV region and visible region, respectively. The enhanced UV-Vis absorption TiO_2 NW due to the presence of Gd nanoparticles can be attributed to the Localized Surface Plasmon Resonance induced by the Gd NPs.

REFERENCES

A. Irrera et al., "Quantum confinement and electroluminescence in ultrathin silicon nanowires fabricated by a maskless etching technique," Nanotechnology, vol. 23, no. 7, 2012, doi: 10.1088/09574484/23/7/075204.

A. Mondal, A. Ganguly, A. Das, B. Choudhuri, and R. K. Yadav, "The Ag Nanoparticles/ TiO2 Thin Film Device for Enhanced Photoconduction and Role of Traps," Plasmonics, vol. 10, no. 3, pp. 667–673, 2015, doi: 10.1007/s11468-014-9852-7.

E. Hutter and J. H. Fendler, "Exploitation of localized surface plasmon resonance," Adv. Mater., vol. 16, no. 19, pp. 1685–1706, 2004, doi: 10.1002/adma.200400271.

M. Ge et al., "A review of one-dimensional TiO2 nanostructured materials for environmental and energy applications," Journal of Materials Chemistry A, vol. 4, no. 18. pp. 6772–6801, 2016. doi: 10.1039/c5ta09323f

P. Chinnamuthu, J. C. Dhar, A. Mondal, A. Bhattacharyya, and N. K.

P. Makuła, M. Pacia, and W. Macyk, "How to Correctly Determine the Band Gap Energy of Modified Semiconductor Photocatalysts Based on UV-Vis Spectra," J. Phys. Chem. Lett., vol. 9, no. 23, pp. 6814–6817, 2018, doi: 10.1021/acs.jpclett.8b02892.

S. Reghunath, D. Pinheiro, and S. D. Kr, "Applied Surface Science Advances A review of hierarchical nanostructures of TiO2: Advances and applications," vol. 3, no. January, https://doi.org/10.1016/j.apsadv.2021.100063

Singh, "Ultraviolet detection using TiO2 nanowire array with Ag Schottky contact," J. Phys. D. Appl. Phys., vol. 45, no. 13, 2012, doi: 10.1088/0022-3727/45/13/135102.

T. Itoh, Y. S. Yamamoto, and Y. Ozaki, "Plasmon-enhanced spectroscopy of absorption and spontaneous emissions explained using cavity quantum optics," Plasmon-enhanced

spectroscopy of absorption and spontaneous emissions explained using cavity quantum optics - Chemical Society Reviews (RSC Publishing), Jun. 27, 2017. https://pubs.rsc.org/en/content/articlelanding/2017/cs/c7cs00155j

Vacancies - Topics in Catalysis," SpringerLink, Aug. 13, 2020. https://link.springer.com/article/10.1007/s11244-020-01349-1

X. Chen and S. S. Mao, "Titanium dioxide nanomaterials: Synthesis, properties, modifications and applications," Chemical Reviews, vol. 107, no. 7. pp. 2891–2959, 2007. doi: 10.1021/cr0500535

Y. Li, C. Wang, C. Zhang, and H. He, "Formaldehyde Oxidation on Pd/TiO2 Catalysts at Room Temperature: The Effects of Surface Oxygen

10

Fabrication of β-Ga_2O_3 Nanowire Arrays on p-Si using GLAD as a Dielectric for MOS Capacitor

*Michael Cholines Pedapudi, Sudem Daimary and Jay Chandra Dhar**

Abstract

This paper presents the fabrication of symmetrical b-Ga2O3 nanowires on p-Si substrate through glancing angle deposition (GLAD) technique inside the RF/DC sputtering chamber. With the help of FE-SEM and HR-TEM analysis the structural analysis of nanowire arrays and single nanowire was obtained respectively. Moreover, the capacitive behaviour of the p-Si/b-Ga2O3 nanowire arrays device was analysed by evaluating the electrical properties i.e capacitance-voltage (C-V) and conductance-voltage (G-V) characteristics by varying frequencies from 20 KHz to 1 MHz. It shows a higher capacitance of 20.2 pF and conductance of 36.28 μS at 1MHz frequency. The fabricated p-Si/b-Ga2O3/Ag device's estimated interface state density (Dit) as 2.84×1010 eV−1 cm−2 at 1 MHz and it exhibited a low leakage current of 1.9×10-9 A at +1 V.

Keywords: β-Ga_2O_3, **GLAD, Nanowires, RF/DC Sputtering.**

Introduction

The metal oxide semiconductor (MOS) capacitor plays an important role

in chip technology for designing low power high efficient MOSFETs [1]. One of the promising candidate for MOS dielectric is the one dimensional (1-D) β-Ga_2O_3 metal oxide. This material stands out due to its remarkable properties a favourable dielectric constant (~10), wide band gap (4.7 eV), and impressive thermal stability on silicon substrates among the all available phases of the β-Ga_2O_3 [2]. Moreover, the extensive exploration of capacitive memory effects across different materials has highlighted the exceptional attributes of 1-D β-Ga_2O_3 metal oxides. The synthesis of β-Ga_2O_3 has been extensively explored by researchers, utilizing a variety of techniques such as sputtering [3], spray pyrolysis [4] and metal-organic chemical vapor deposition (MOCVD) [5]. Notably, a straightforward and efficient method known as Glancing Angle Deposition (GLAD) has gained importance. This catalyst-free technique allows for precise control over large-area growth and has been employed successfully to fabricate 1-D β-Ga_2O_3 nanowires. By involving the advantageous properties of β-Ga_2O_3 nanowires like high crystallinity, quantum confinement effect, charge radial transport and high surface to volume ratio which helps in the fabrication of nanoscale-based charge storage device applications [6]. An interesting aspect of β-Ga_2O_3 is its capability to offer a substantial band offset when it formed a p-n junction with p-Si substrate. To further enhance this band offset, researchers have inventively employed β-Ga_2O_3 nanowires as clear from the band gap of nanoscale devices increases from bulk structures. This strategy effectively increases the conduction band discontinuity, holding promise for advanced electronic applications [7,8]. Based on these insights, the concept of β-Ga_2O_3 nanowires has been extended to the development of capacitive memory devices. Notably, this represents the pioneering utilization of the GLAD technique to fabricate such devices. Furthermore, by increasing the band offsets of the β-Ga_2O_3 fabricating on p-Si substrate established the development of capacitive memory devices based on nanowires enhanced dielectrics. Thus, paving the way for exciting advancements in good MOS capacitor.

Our study focuses on investigating the storage capacity of a β-Ga_2O_3 nanowire arrays device through capacitance-voltage (C-V) and conductance-voltage (G-V) measurements. We analyzed the morphology of the β-Ga_2O_3 nanowires using techniques such as X-ray diffraction (XRD), Field Emission Scanning Electron Microscopy (FE-SEM) and High-Resolution Transmission Electron Microscopy (HR-TEM). To comprehensively assess the device, we conducted various measurements including dark current-voltage (I-V) characteristics, capacitance-voltage (C-V) and conductance-voltage (G-V)

characteristics. These measurements were performed using a semiconductor parameter analyzer, specifically the Keithley 4200-SCS model.

Experimental Section

β-Ga_2O_3 nanowires were synthesized on p-Si substrate via the GLAD technique using in RF/DC sputtering machine (smart coat 3.0, HHV, INDIA). Initially, cleaning of the p-type Si <100> substrates done using RCA method, then depositing β-Ga_2O_3 material from a 99.99% pure target onto the substrates. The distance between target and substrate holder was maintained at 10 cm, with rotating substrate holder at 70 rpm with 85° GLAD angle. Sputtering gas argon (Ar) was controlled at 10 sccm with maintaining chamber pressure at 3×10^{-3} mbar. The RF power of 150 W and growth rate of 0.5/sec used for producing β-Ga_2O_3 nanowire arrays. Furthermore, ~40 nm silver (Ag) layer was sputtered (using DC sputtering) on top of the β-Ga_2O_3 nanowires using a shadow mask with circular diameter of 1.19 mm with 5 mA DC current and 350 V voltage for making a metal contact.

Results and Discussion

Structural and morphological analysis

The structural study of the developed symmetrical β-Ga_2O_3 nanowires on p-type Si substrate was investigated using FE-SEM imaging. Fig.1 shows a cross-sectional view of the constructed β-Ga_2O_3 nanowire array with an 85° GLAD orientation. Over the substrate, a well-separated and vertically oriented nanowires with an average length of ~ 270 nm are formed. The top view of the FE-SEM image of the β-Ga_2O_3 nanowire arrays is shown in inset of Fig.1 confirming that the nanowires were porous and developed to a diameter of ~ 91 nm.

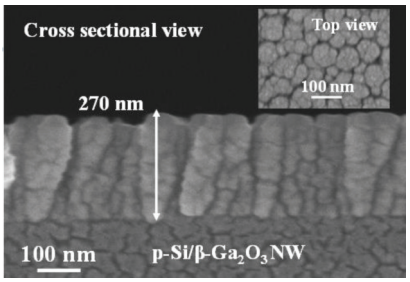

Fig.1. Cross-sectional and Top view (inset) FE-SEM image of β-Ga_2O_3 nanowire arrays.

HR-TEM is a technique used for analysing the structural attributes of fabricated β-Ga_2O_3 nanowire sample. Fig.2(a) provides a illustration of a TEM image showcasing an individual β-Ga_2O_3 nanowire fabricated through the GLAD technique within the confines of the RF sputtering chamber. The resultant nanowire lengths of ~270 nm. Highlighted within the image is the growth orientation of the nanowire as indicated by the blue arrow. Furthermore, the symmetry of the nanowire is evident with closely matching upper and lower diameters of ~90 nm each. Furthermore, the fabricated β-Ga_2O_3 sample crystallite structure and its phase analysis were determined using the XRD measurement technique. Also, Fig.3(b) shows the XRD pattern for β-Ga_2O_3 nanowires grown on p-Si substrate. The fabricated sample has diffraction peaks at (34.53°), (48.11°) and (57.05°) corresponding to (111), (003) and (-313) orientation respectively for β-Ga_2O_3 [9]. Apart from these peaks, other peak corresponding to the (100) orientation for Si substrate was also observed [10].

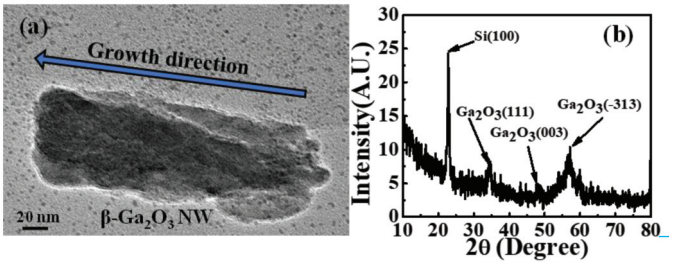

Fig. 2 (a) TEM image of single β-Ga_2O_3 nanowire (b) XRD pattern of β-Ga_2O_3 nanowire arrays sample.

Current and Voltage characteristics

Fig.3(a) shows the current (I)-voltage (V) characteristics of p-Si/β-Ga_2O_3 nanowire sample under dark condition and it's inset shows the schematic diagram of p-Si/β-Ga_2O_3 nanowire arrays device. The device structure shows that the Ag metal contact deposited on top of the vertical β-Ga_2O_3 nanowire arrays. Moreover, the β-Ga_2O_3 is a wide band gap metal oxide semiconductor with a work function of ~4.26 eV [11] and its top metal contact silver (Ag) with work function of ~4.26 eV [12] creates a metal-semiconductor ohmic contact. And the device shows non-linear rectifying characteristics with a dark current of 1.9 nA at 1 V. This non-linear rectifying characteristics can be attributed to

the p-n junction formed between β-Ga_2O_3 and p-Si substrate. It is also seen that the dark current is lower than that some of the recently reported devices [13,14].

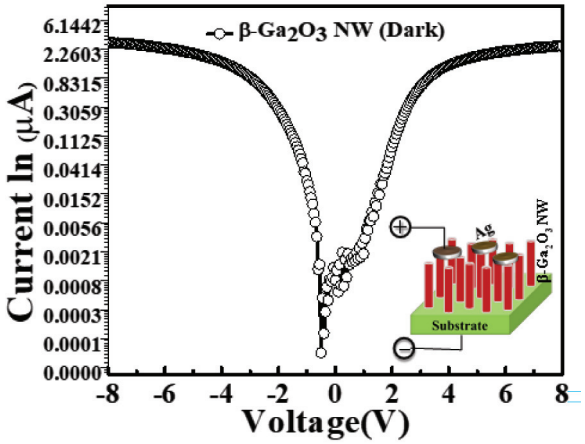

Fig.3 I-V Characteristics for p-Si/β-Ga_2O_3 nanowire device (in dark) and inset depicts the device structure diagram.

C. Capacitance-Voltage (C-V) Characteristics

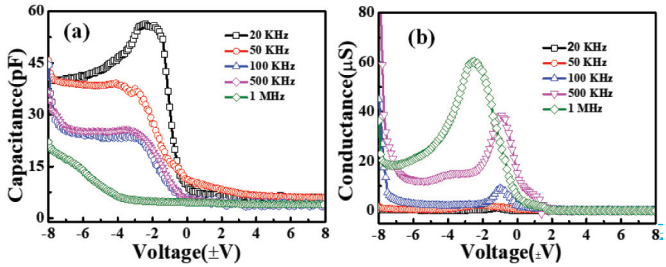

Fig.4(a) Capacitance versus voltage (C-V) and (b) conductance versus voltage (G-V) characteristics at different frequency of p-Si/β-Ga_2O_3 nanowire arays device.

Capacitance-voltage (C-V) measurements was determined to find the charge storage capability which is dependent on both the voltage as well as the frequency. Fig.4(a) depicts that the C-V characteristics for p-Si/β-Ga_2O_3 nanowire arrays device at different frequencies (20 KHz, 50 KHz, 100 KHz, 500 KHz, 1 MHz) by sweeping the voltages from -8 to +8 V under dark conditions. Furthermore, C-V graph exhibits three distinct modes named as accumulation, depletion, and inversion regions with typical p-type behaviour. In the accumulation region, under a specific bias voltage, the capacitance follows

a distinct pattern with varying frequencies. It decreased from 20 kHz to 1MHz indicating a frequency-dependent response. This behaviour in the accumulation region can be attributed to the frequency dependent series resistance restricting from oxide charges [15]. These charges exist at the interface (p-Si/β-Ga_2O_3) between the semiconductor and high band gap material which act as dielectric at the junction. Here, the accumulation capacitance in Fig.4(a) depicts the capacitance at dark condition for p-Si/β-Ga_2O_3 nanowire arrays device obtained at 20.2 pF at 1 MHz frequency. Moreover, owing to the existence of interface states at p-Si/β-Ga_2O_3 interface follows the ac signal and thus produces an additional capacitance at low frequencies. In case of high frequencies, the behaviour of interface states deviates from the AC signal response due to the presence of ample carrier interface traps [16]. Consequently, these interface states do not contribute to the MOS capacitance. However, in the inversion layer formed by minority charge carriers originating within the depletion region gets swept to the surface by a strong electric field [17]. Furthermore, the capacitance values exhibit a hump at a frequency of 20 kHz. This peculiar hump tends to reduce as the frequency increases. This behaviour suggests the presence of diverse interface states with varying lifetimes. While these states can effectively fallow an AC signal at low frequencies.

Fig.4(b) shows variation of the conductance (G) with applied voltage (V) characteristics of p-Si/β-Ga_2O_3/Ag device for different frequencies ranging from 20 KHz to 1 MHz. Moreover, it shows higher conductance value of 36.28 μS at 1 MHz frequency. The determined conductance follows a clear pattern where higher frequencies are correlated with higher conductance and lower frequencies are associated with lower conductance. This is attributed to the oxide capacitance works in series with the capacitance associated with interface trap resistance in MOS devices, which increases the conductance in increase in frequency [18]. Besides, the interface trap density ($D_{it}D_{it}$) was calculated from the G-V curves for the fabricated device determined using the Hill-Coleman technique [19] from equation (1).

$$D_{it}D_{it} = \frac{(\frac{2}{qA})(\frac{G_{m\,max}}{w})}{((\frac{G_{m\,max}}{wC_{ox}})\,2 + (1-\frac{C_m}{C_{ox}})2)} \qquad (1)$$

Where q,A,$G_{m\,max}$,ω,$C_{ox}$and C_m are the charge of an electron, device area, maximum measured conductance, angular frequency, capacitance in the

accumulation region and maximum capacitance corresponding to the $G_{m\ max}$, value respectively. The value of D_{it} at 1 MHz is found to be 2.84×10^{10} eV^{-1} cm^{-2}. The higher value of the D_{it} indicates more amount of interface trap density. The calculated D_{it} value allowed to quantify the impact of defects and traps at the semiconductor-oxide interface. This value serves as a valuable metric for evaluating the quality of the device's fabrication and its potential impact on overall performance.

Conclusions

In summary, GLAD equipped RF/DC sputtering method was used for fabrication of p-Si/β-Ga_2O_3/Ag nanowire arrays capacitive device. C-V and G-V characteristics were obtained for the devices at various frequencies ranging from 20 kHz to 1 MHz. Nanowire structure increases the surface-to-volume ratio between the high band gap β-Ga_2O_3 and Ag metal which results in high capacitance value. At 1 MHz, a high D_{it} of 2.84×10^{10} eV^{-1} cm^{-2} was obtained p-Si/β-Ga_2O_3 nanowire arrays device.

Acknowledgement

We would like to thank the SERB project (EMR/2017/00 1863), DST Govt. of India for providing fabrication facilities, CSIR-NEIST JORHAT for for FE-SEM, SAIF NEHU, Shillong for HR-TEM analysis. And also, NIT Nagaland for XRD facility and TEQIP-III FOR funding this research.

REFERENCES

1. Yu, X., Marks, T.J. and Facchetti, A., 2016. Metal oxides for optoelectronic applications. Nature materials, 15(4), pp. 383-396.
2. Lyle, L.A., 2022. Critical review of Ohmic and Schottky contacts to β-Ga_2O_3. Journal of Vacuum Science & Technology A, 40(6).
3. Tadjer, M.J., Luna, L.E., Cleveland, E., Hobart, K.D. and Kub, F.J., 2018. Fabrication and characterization of β-Ga_2O_3 heterojunction rectifiers. ECS Transactions, 85(7), p. 21.
4. Raphael, R. and Anila, E.I., 2021. Investigation of photoluminescence emission from β-Ga_2O_3: Ce thin films deposited by spray pyrolysis technique. Journal of Alloys and Compounds, 872, p.159590.
5. Alema, F., Hertog, B., Mukhopadhyay, P., Zhang, Y., Mauze, A., Osinsky, A., Schoenfeld, W.V., Speck, J.S. and Vogt, T., 2019. Solar blind Schottky photodiode

based on an MOCVD-grown homoepitaxial β-Ga_2O_3 thin film. APL Materials, 7(2).

6. Pedapudi, M.C. and Dhar, J.C., 2022. A novel high performance photodetection based on axial NiO/β-Ga_2O_3 pn junction heterostructure nanowires array. Nanotechnology, 33(25), p.255203.
7. Zhou, K., Shang, G., Hsu, H.H., Han, S.T., Roy, V.A. and Zhou, Y., 2023. Emerging 2D Metal Oxides: From Synthesis to Device Integration. Advanced Materials, p. 2207774.
8. Suo, H., Wang, Y., Zhang, X., Zheng, W., Guo, Y., Li, L., Li, P., Yang, Y., Wang, Z. and Wang, F., 2023. A broadband near-infrared nanoemitter powered by mechanical action. Matter.
9. Y.M. Juan, S.J. Chang, H.T. Hsueh, S.H. Wang, W.Y. Weng, T.C. Cheng, C.L. Wu, Effects of humidity and ultraviolet characteristics on β-Ga_2O_3 nanowire sensor, RSC Adv. 5 (103) (2015) 84776–84781
10. P. Deb, J.C. Dhar, Low dark current and high responsivity UV detector based on TiO2 nanowire/RGO thin film heterostructure, IEEE Trans. Electron Devices 66 (9) (2019) 3874–3880
11. Meitei, S.R., Rajkumari, R. and Singh, N.K., 2020. Post deposition annealing effect on the electrical properties of β-Ga_2O_3 Nanowire. Journal of Materials Science: Materials in Electronics, 31(22), pp. 20378-20386.
12. Lefort, A., Akbi, M. and Parizet, M.J., 1994, May. Experimental determination of work function of silver alloys. In XVI International Symposium on Discharges and Electrical Insulation in Vacuum (Vol. 2259, pp. 486-490). SPIE.
13. C. Wu, C. He, D. Guo, F. Zhang, P. Li, S. Wang, A. Liu, F. Wu, W. Tang, Vertical α/β-Ga_2O_3 phase junction nanorods array with graphene-silver nanowire hybrid conductive electrode for high performance self-powered solar blind photodetectors, Mater. Today Phys. 12 (2020), 100193.
14. Atilgan, A., Yildiz, A., Harmanci, U., Gulluoglu, M.T. and Salimi, K.U.R.O. α., 2020. β-Ga_2O_3 nanoflakes/p-Si heterojunction self-powered photodiodes. Materials Today Communications, 24, p.101105.
15. K. Shubham, R. Khan, Electrical characterization of TiO_2 insulator based Pd/ TiO_2/ Si MIS structure deposited by solegel process, J. Nano Electron. Phys. 5 (2013), 01021e010215.
16. A. B. Selçuk, "On the dielectric characteristics of Au/SnO_2/n-Si capacitors," Physica B: Condensed Matter 396. 1-2 (2007), pp. 181-186.
17. Preier, H., 1968. Different mechanisms affecting the inversion layer transient response. IEEE Transactions on Electron Devices, 15(12), pp.990-997.
18. McAdams E.T., Henry P., Anderson J.M. and Jossinet J., Optimal electrolytic chloriding of silver ink electrodes for use in electrical impedance tomography, Clin. Phys. Physiol. Meas. 1992 Vol. 13, Suppl. A.
19. Lahiri, R. and Mondal, A., 2018. Superior memory of Er-doped TiO_2 nanowire MOS capacitor. IEEE Electron Device Letters, 39(12), pp. 1856-1859.

11

GLAD Synthesized ZnO Nanowires for Capacitive Memory Application

*Sudem Daimary, Michael Cholines Pedapudi and Jay Chandra Dhar**

Abstract

Using glancing angle deposition (GLAD) technique the authors have fabricated vertical ZnO NWs over the Si substrate. The fabricated ZnO NWs exhibited crystalline nature when examined using X-ray diffraction measurement. The field emission scanning electron microscopy (FE-SEM) performance show vertical heterostructure (HS) nanowires (NWs). The capacitive behaviour of the device and the sample was investigated by assessing the capacitance-voltage (C-V) and conductance-voltage (G-V) characteristics at a range of frequencies from ± 8V for the sample. The device demonstrated a heightened capacitive memory with an interface trap density of ~ 10 x 10^9 $eV^{-1}cm^{-2}$, charge storage density of ~ 5.1 x 10^9 cm^{-2}, and a memory window of ~ 0.78 V under the ± 8V sweeping voltage at 1 MHz.

Keywords: ***GLAD, ZnO, Nanowire and capacitive memory***

Introduction

In the last two decade, semiconductor metal-oxides based capacitive memory has been explored extensively including ZnO material and many other types of material [1]. Nowadays, one-dimensional (1D) metal oxides have been

gaining an excellent attention because of their high storage density and reduced power consumption in comparison to their bulk counterpart more specifically nanowires (NW) [2]. 1D device generates more electric fields surrounding its surfaces. Because, the NW shape strengthens the local electric field, the filament production site is restricted, improving switching stability and repeatability of non-volatile stored information [2]. However, lowering dielectric thickness increases leakage current and is substituted by high-k materials like TiO_2, ZrO_2, HfO_2, SnO_2, WO_3 and ZnO etc. [3]. Owing to this, ZnO is one of them high-k property, comparable dielectric constant (~ 10), high electron mobility (200 cm^2/Vs), a wide band gap (3.37 eV), and high binding energy of 60 meV with great thermal and chemical stability making it a promising material for capacitive memory applications [4].

Moreover, to grow the vertically well aligned 1D nanowire is a challenging task for a dominant metal oxide based memory devices. Large group of researchers have been utilized a wide variety of techniques in order to prepare ZnO NWs some of these techniques include sputtering [5], hydrothermal [6], MOCVD [7], and others. To create 1D ZnO NWs, a process called as glancing angle deposition (GLAD) has been used. It is a catalyst free fabrication technique and has a good control mode for NW deposition which can increase surface roughness resultant in a large number of oxygen vacancies as a consequence may an increase in the leakage current [4]. Therefore, reduction of dark current in a device is a challenging task, which extended the next study of our work for high-performance capacitive memory device applications. Owing to this, in this study we have investigated technique to grow vertical ZnO NWs that can be utilized as a dielectric so that we could deploy ZnO NWs for non-volatile memory applications.

In this study, we explore for the first time using a GLAD technique grounded on vertically oriented ZnO NWs as a dielectric based capacitive memory application. Studies of capacitance-voltage (C-V) and conductance-voltage (G-V) measurements exhibited to learn more about the surface's localized electronic states. These phases may arise in ZnO NWs due to the formation of oxide layer, lattice disruption and the accumulation of impurities. Field emission scanning electron microscopy (FE-SEM) and X-ray diffraction (XRD) were used to examine the structural and morphological studies of ZnO NWs. Current-voltage (I-V) and capacitance-voltage (C-V) properties were measured. The C-V hysteresis of the device was also studied for a variety of bias voltages, memory windows, and charge storage densities.

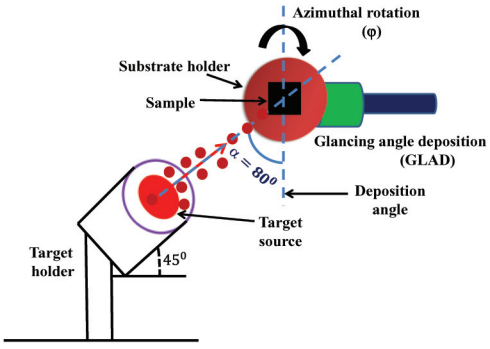

Figure-1: Schematic diagram of GLAD technique embedded inside the RF magnetron sputtering system.

Materials and Methods

Material and Device Fabrication Technique

The vertical ZnO NWs were fabricated employing the RF magnetron sputtering integrated with GLAD (Smart Coat 3.0, HHV India). Initially, RCA (Radio Corporation of America) clean Silicon (Si) (100) substrates (1×1 cm^2) were place onto the substrate holder and then loaded inside the high vacuum sputtering chamber. High purity Zinc Oxide (ZnO, 99.999%) target was used as source material in order to develop the vertical NWs. Prior to fabrication, the base pressure was maintained at ~ 4 x 10^{-6} mbar, a constant rate of 10 sccm (standard cubic centimeter per minute) Argon (Ar) (sputtering gas) and RF power of 150 W. Next, the substrate holder maintained a distance from target source around 10 cm and it was kept at an angle (GLAD angle) of 80° normal to the target and constantly revolved azimuthally at 70 rpm in order to grow vertically aligned uniform ZnO NWs over the Si. Moreover, silver (Ag) contacts of ~ 50nm thickness were grown above the ZnO NWs by using shadow mask (1.5 mm diameter) to measure the device performance. A DC current of 0.5 A was maintained in order to deposit the Ag contacts along with 15 sccm Ar was used.

Characterization techniques like X-ray diffraction (XRD) (Rigaku Ultima, Cu K , =1.54 Å), Field emission scanning electron microscopy (FESEM) (Zeiss Ultra 55), current–voltage (I-V) and capacitance (C) – voltage (V) analyses were performed in order to study the vertical ZnO NWs based capacitive memory device. Finally, the device analysis (I-V and C-V) were carried

out via semiconductor parameter analyzer (Keithley 4200 Semiconductor Characterization System (SCS)).

Results and Discussion

Structural and Morphological Analysis

Figure 2 shows the XRD analysis of a ZnO NWs sample deposited on the Si substrate. From XRD spectra it is observed that ZnO NWs sample exhibited sharp diffraction peak at 34.32° corresponding to (002) orientation for ZnO hexagonal wurtzite structure along with c-axis (JCPDS data 00-036-1451) [8]. Moreover, the fabricated sample shows a small peak at 62.59° corresponding to (103) orientation for ZnO [8].

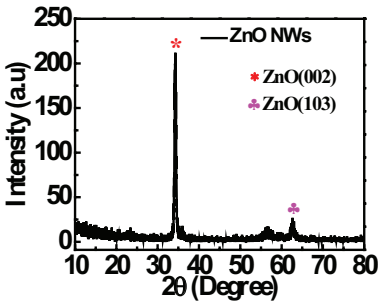

Figure-2: XRD analysis for ZnO NWs sample.

The XRD output confirms that sample was polycrystalline in nature. Further, we have calculated crystallite size (D), micro-strain (e) and dislocation density (d) for dominant intense peak (002) plane using the following equations as given in reference [9] and found to be 0.37 nm, 0.09 and 7.30 nm^{-2}. However, the calculated e and d were found to be higher than some reported literature [4], respectively.

Figure 3 (a) and (b) shows cross-sectional and top-view FE-SEM images that were carried out to analyse the structural information of ZnO NWs sample. From fig. 2, it is observed that the total length of ZnO NWs is found to be ~ 372 ± 2 nm which is deposited over the Si substrate. Moreover, the average diameter and porosity is found to be ~ 91 ± 9 nm and ~ 38 ± 6 nm indicated with dotted arrow. Fig. 3 (c) displays peak emission from O (oxygen), Si (silicon), Cu (copper), and Zn (zinc) K shells can be seen in an EDS spectrum taken from the cross-section of the ZnO NWs, indicating that only these elements are present.

As an additional feature, an inset table with the estimated atomic and weight percentages of the sample is presented in Fig. 3 (c).

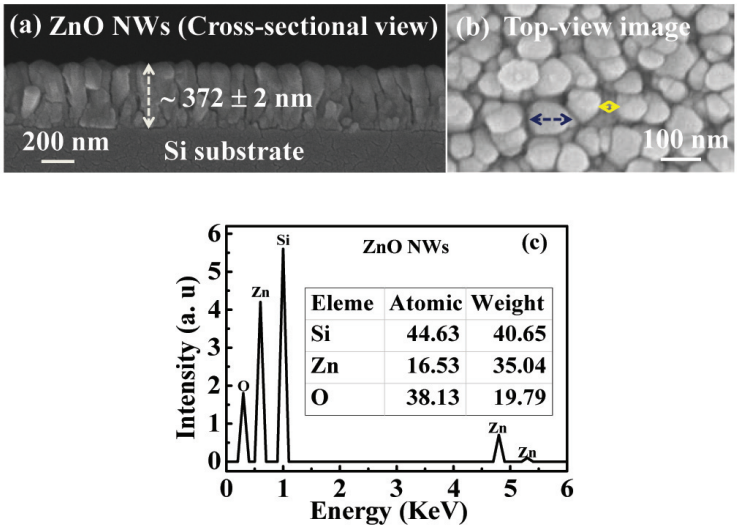

Figure-3: FE-SEM image of (a) Cross-section (b) Top-view and (c) EDS spectra of ZnO NWs sample.

2. Current (I)-Voltage (V) Measurement for ZnO NW Arrays PD

Figure 4 (a) shows schematic diagram of the fabricated ZnO NW arrays sample. Fig. 4 (b) depicts the I-V characteristics of the fabricated sample and it is observed that ZnO NWs sample has shown a dark current of ~ 2.07 nA at -1V bias voltage. However, the exhibited dark current is little bit higher as compared to recently reported literature [4]. The higher dark signified that higher number of trap state present in the sample which can increase the dark current of the device [10]. In addition, the photoresponse (I_{Light}/I_{Dark}) of the sample exhibits a linear increase from lower to higher voltage as shown in fig. 4 (c), indicating that the produced electron-hole pairs were efficiently captured by the strong electric field, hence lowering the recombination rate. As a result, the photocurrent increased proportionally with the applied voltage, as more of the produced carriers are collected.

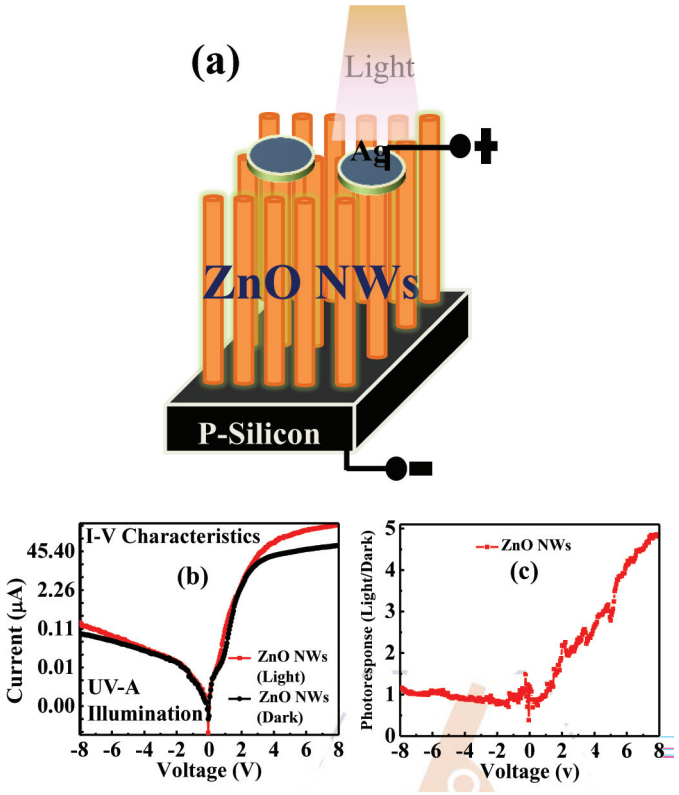

Figure-4: (a) Schematics diagram of the device (b) I-V characteristics and (c) photoresponse for ZnO NWs sample.

3. Capacitance (C)-Voltage (V) Characteristics

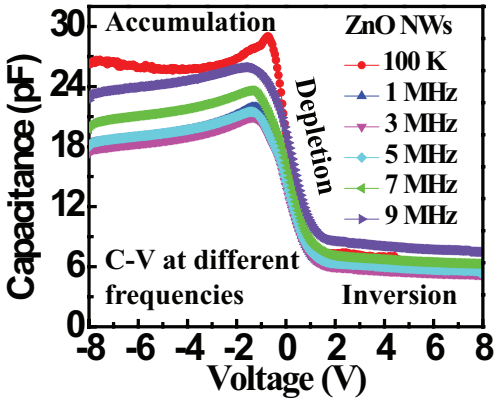

Figure-5: C-V characteristics of ZnO NWs at ambient temperature.

Figure 5 shows the C-V characteristics of ZnO NWs sample taken at various frequencies ranging from 100 KHz to 9 MHz at room temperature under dark conditions. The sweeping voltage bias measured from -8 to +8 V at difference frequencies. The C-V characteristic was carried out to understand the trap density present in the sample. From the C-V graph, as shown in Fig. 5, it is observed that it has three modes of operation namely accumulation, depletion, and inversion identifying from MOS capacitor. The accumulation region the capacitance density is increases as frequency increases from 100 KHz to 9 MHz. In MOS capacitor, the frequency dependence of capacitance is typically characterized by the impact of parasitic capacitance or junction capacitance at higher frequencies [2]. The capacitance varies as a function of frequency due to series resistances and the presence of oxide charges in the dielectric material and at the interface between the substrate and dielectric (Si/ZnO) [3]. At high frequency, the change in capacitance density is observed might be due to the inhomogeneous layer of Si/ZnO. This can cause the flat band voltage to move higher when the frequency is raised.

4. Conductance (G)-Voltage (V) Characteristics

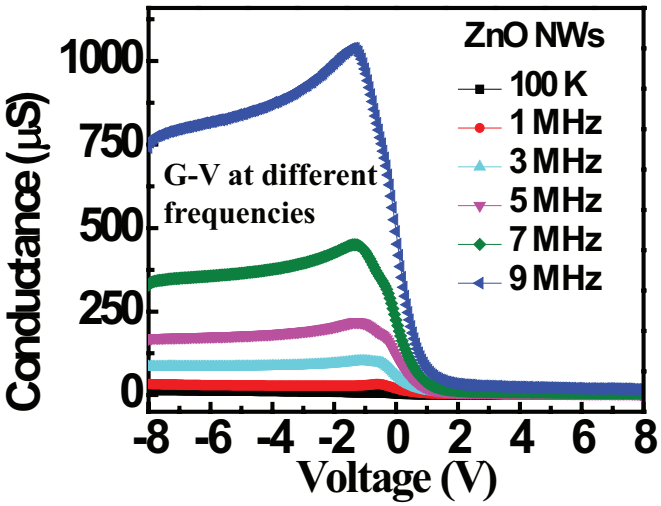

Figure-6: G-V characteristics of ZnO NWs at ambient temperature.

Figure 6 depicts the G-V characteristics of the fabricated ZnO NWs sample at different frequencies from 100 KHz to 9 MHz under dark condition. The G-V is increasing with increased frequency this behaviour may be explained

by the interactions between oxide capacitance in series and interface trap-resistance capacitor of the metal-oxide [3]. The interface trap density (D_{it}) has been calculated by using the following Hill-Coleman formula equation (1) [11] at 1 MHz frequency.

$$D_{it} = \frac{(\frac{2}{qA})(\frac{G_{m\,max}}{\omega})}{(\frac{G_{m\,max}}{\omega C_{ox}})^2 + (1-\frac{C_m}{C_{ox}})^2} \quad (1)$$

Where, q, A, C_m, C_{ox} C_{ox}, and w denotes electronic charge, device area, maximum capacitance associated to the G_{mmax}, capacitance in strong accumulation site and angular frequency. The calculated D_{it} was found to be ~ 10 x 10^9 eV^{-1} cm^{-2} at 1 MHz frequency. The calculated D_{it} value was lower than some recently reported literature [2-3] [11], which signified that at higher frequency interface trap density does not follow the alternating current. The D_{it} value identifies the presence of trap density in the sample. However, the D_{it} value is somewhat better than some reported metal-oxide like Er_2O_3 doped SnO_2 nanowires [12].

5. Hysteresis Performance for ZnO NWs at 1 MHz

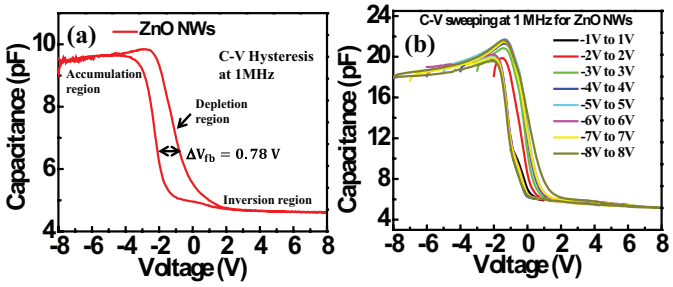

Figure-7:(a) C-V hysteresis (b) sweeping voltage of ZnO NWs at 1 MHz

Figure 7 (a) and (b) displays C - V hysteresis analysis carried out for the ZnO NWs sample at 1 MHz with sweeping voltage from ±1 to ± 8V in room temperature under dark condition for memory window. Higher the memory window, higher the charge storage capability, and signifying capacitance swings forward and backward in opposite directions. This might be an indication of the presence of defects in the oxide layer or trapped charge carriers at the interface of the device [13]. Moreover, from C-V hysteresis, we have calculated the flat-band

voltage shift (ΔV_{fb}) under the sweeping voltage of ± 8V and found it to be ~ 0.78 V at 1 MHz. Basically, it indicates that charge carrier trapping at the junction between metal-oxide and Si interfaces is a possible cause of the sweeping of the voltage [14]. Moreover, we have taken C-V sweeping voltages as shown in fig. 7 (b), it is observed that memory window is increasing with higher sweeping voltage which signified that numbers of charge storage capacity is increased. Further, the electron-hole trapping charge density (N) has been calculated using following equation (2).

$$N = \frac{\Delta V C_{ox}}{qA} \quad (2)$$

Where, q, A,ΔV, and C_{ox}represents the electron charge (1.602 x 10^{-19} C), area of device (1.13 x 10^{-2} cm^2), different of flat band voltage sweeping under forward and reversed gate voltage, and oxide capacitance respectively. On calculation, N was found to be ~ 5.1 x 10^9 cm^{-2}. The calculated trap charge density is found to be quite lower than some reported literature [11] [13-14]. This signified that a stable accumulation capacitance at the junction which can be a good candidate for flash memory.

Conclusions

The GLAD technique incorporated inside the RF/DC magnetron sputtering chamber was used to grow the vertical ZnO NWs for the capacitive memory device. By sweeping the voltage bias (±8V), the capacitive impact of the pure ZnO NWs was determined at a variety of frequencies during the C-V and G-V studies. The C-V and G-V characteristics reveal that charges are trapped by the existence of interface states at the ZnO NWs/Si interface. Interface trap density (D_{it}) of ~ 10 x 10^9 $eV^{-1}cm^2$ and an enhanced memory window of ~ 0.78 V at 1MHz frequency, the ZnO NWs could be suitable candidate for nanoscale MOS capacitor.

Acknowledgements

The authors would like to extend their heartfelt appreciation to the SERB (DST) project (EMR/2017/001863), Government of India for providing fabrication facilities and funds. NCPRE at IIT Bombay for FE-SEM analysis, India. National Institute of Technology Nagaland for providing the X-ray diffraction facility (Department of Physics) and current (I) – voltage (V) characterization and other assistance.

REFERENCES

1. Cao X, Li X, Gao X, Liu X, Yang C, Yang R, Jin P. All-ZnO-based transparent resistance random access memory device fully fabricated at room temperature. Journal of Physics D: Applied Physics. 2011 Jun 9; 44(25):255104, DOI 10.1088/0022-3727/44/25/255104.
2. Pooja P, Chinnamuthu P. Improved Capacitive Memory in Glancing Angle Electron-Beam Synthesized Isotropic Bilayer n-TiO 2/In 2 O 3 Nanowires Array. IEEE Transactions on Nanotechnology. 2023 Feb 7;22:70-5.
3. Lahiri R, Mondal A. Superior memory of Er-doped TiO 2 nanowire MOS capacitor. IEEE Electron Device Letters. 2018 Oct 8;39(12):1856-9.
4. Daimary S, Dhar JC. Ultrafast photoresponse using axial n-ZnO/p-CuO heterostructure nanowires array-based photodetectors. IEEE Transactions on Electron Devices. 2022 May 26;69(7):3768-74.
5. Mamat MH, Malek MF, Hafizah NN, Asiah MN, Suriani AB, Mohamed A, Nafarizal N, Ahmad MK, Rusop M. Effect of oxygen flow rate on the ultraviolet sensing properties of zinc oxide nanocolumn arrays grown by radio frequency magnetron sputtering. Ceramics International. 2016 Feb 15;42(3):4107-19.
6. Rajamanickam S, Mohammad SM, Hassan Z. Effect of zinc acetate dihydrate concentration on morphology of ZnO seed layer and ZnO nanorods grown by hydrothermal method. Colloid Interface Sci Commun 38: 1–13.
7. Roge V, Guignard C, Lamblin G, Laporte F, Fechete I, Garin F, Dinia A, Lenoble D. Photocatalytic degradation behavior of multiple xenobiotics using MOCVD synthesized ZnO nanowires. Catalysis Today. 2018 May 15;306:215-22.
8. Costas A, Florica C, Preda N, Kuncser A, Enculescu I. Photodetecting properties of single CuO–ZnO core–shell nanowires with p–n radial heterojunction. Scientific reports. 2020 Oct 29;10(1):18690.
9. Chetri P, Dhar JC. Improved photodetector performance of SnO2 nanowire by optimized air annealing. Semiconductor Science and Technology. 2020 Mar 5;35(4):045014.
10. Chetri P, Dhar JC. Capacitive memory using GLAD synthesized annealed SnO2 nanowires array as a dielectric. In2022 IEEE VLSI Device Circuit and System (VLSI DCS) 2022 Feb 26 (pp. 139-142). IEEE.
11. Rajkumari R, Ngangbam C, Singh NK. Presence of capacitive memory in GLAD-synthesized WO 3 nanowire. Journal of Materials Science: Materials in Electronics. 2021 Feb;32:3191-200.
12. Panigrahy S, Dhar JC. Non-volatile memory application of glancing angle deposition synthesized Er2O3 capped SnO2 nanostructures. Semiconductor Science and Technology. 2020 Apr 9;35(5):055035.

13. Deb P, Dhar JC. Graphene oxide charge blocking layer with high K TiO2 nanowire for improved capacitive memory. Journal of Alloys and Compounds. 2021 Jul 5;868:159095.
14. Lahiri R, Mondal A. Improved capacitive memory of Er: TiO2 TF based MOS device. Journal of Alloys and Compounds. 2019 Jul 5;792:679-83.

12

Thermochromic property Analysis of Hydrothermally Synthesized VO_2

Arka Dey, Iman Biswas, Subrata Saha and Aniruddha Mondal

Abstract

In this study, we present a straightforward and cost-effective method for synthesizing VO_2 (M) through a hydrothermal process. The results of our temperature-dependent optical investigations yield crucial insights into the phase transition behaviour of this material. During both the heating and cooling processes, the transition temperature is notably observed at 60.5 and 47.1 °C, respectively. Impressively, this transition temperature, measured at 53.8 °C, is lower than the previously reported value for VO_2 crystals (approximately 68 °C). Furthermore, the thin film of VO_2 demonstrates a rapid and substantial metal-to-semiconductor transition, with a transmittance change of nearly two orders of magnitude. These findings underscore the successful one-step hydrothermal synthesis of monoclinic VO_2 and, importantly, offer valuable perspectives on its potential applications in advanced technologies such as infrared smart windows.

Keywords: Thermochromic material, hydrothermal reaction, VO2 films, metal–semiconductor transitions, smart windows

Introduction

The Vanadium dioxide, specifically in its monoclinic phase (VO_2 (M)), possesses a captivating combination of electrochromic and thermochromic characteristics, making it an ideal choice for dynamic coatings in smart window

applications [1, 2]. Additionally, it offers the advantage of blocking ultraviolet (UV) radiation while modulating infrared (IR) light [3]. Crystalline VO_2 undergoes a notable phase transition, known as thermochromism, occurring around 68 °C. This transition involves a shift in its crystalline structure from a semiconducting monoclinic phase to a conductive tetragonal phase. This intriguing property, discovered by Morin in 1959 [1], has garnered substantial attention from researchers due to its reversible nature. VO_2 exhibits a distinct, temperature-driven, and reversible first-order semiconductor-to-metal transition (SMT) [4]. VO_2 (M) stands out as a promising thermochromic material, particularly for smart window applications, as its crystalline phases interchange between monoclinic and rutile at the transition temperature (T_{SMT}) of approximately 338 K. This transition leads to significant changes in its electrical and optical properties [1, 5]. Below the T_{SMT}, VO_2 (M) behaves as a semiconductor, partially transmitting infrared light, while above T_{SMT}, it transforms into a metallic phase with high infrared reflectance [6-8]. Consequently, there is a critical need to modulate T_{SMT} to room temperature, not only for smart windows but also for various practical applications. VO_2 (M) has also found relevance in the realm of lithium-ion batteries due to its remarkable electrochemical properties [9]. Moreover, other metastable phases, including VO_2 (D) and VO_2 (P), have gained significance as they can be readily transformed into the VO_2 (M) phase through post-annealing treatments [10, 11].

In the quest to synthesize VO_2 nanoparticles, various methods have been developed, such as RF sputtering, pulsed laser deposition, chemical vapour deposition, and wet chemical processes (including thermolysis, sol-gel, spray pyrolysis, pyrolysis of precursor powders, and hydrothermal synthesis) [12-16]. Among these methods, pyrolysis processes are often challenging, energy-intensive, and involve complex procedures for fabricating the vanadium precursor [14]. Among the available synthesis techniques, the hydrothermal process stands out due to its environmental friendliness, flexibility, cost-effectiveness, simple mass production setup, and the ability to control grain growth [17]. The hydrothermal technique has gained significant attention from researchers for its capability to fabricate diverse structures of VO_2 nanostructured materials, such as nanorods (NRs), nanowires (NWs), nanobelts (NBs), and nanotubes (NTs), all with high-quality crystallinity. This synthesis process has garnered considerable interest owing to its appealing physical and chemical properties and its potential applications in various fields, including nano-devices [18-20].

This paper focuses on thesynthesis of VO_2 by hydrothermal process and the fabrication of thin film comprising the monoclinic phase of VO_2 (M). This work provides a comprehensive characterization of its physical attributes. Furthermore, the study delves into the temperature-dependent optical properties, offering valuable insights into this material's behavior under varying thermal conditions.

Materials and Methods

Preparation of VO_2 powder

To prepare VO_2 particles we go through hydrothermal synthesis process, followed by thermal annealing. The process of hydrothermal synthesis of VO_2 has been shown in a schematic diagram (Fig. 2). In a typical procedure, we used commercial vanadium pentoxide (V_2O_5) powder as the source of vanadium, oxalic acid dehydrate ($H_2C_2O_4$–$2H_2O$) as reducing reagent as well as the morphology controller, dissolved in distilled water (20 mL). Then the mixture was stirred for 18 h at room temperature. Later, into a Teflon container with capacity of 50 ml the generated precursor (dark blue solution) was transferred and then sealed it into a stainless steel container. The whole system was kept at 180 °C for 24 h and then cooled down gradually to Room temperature and produced black precipitate was then collected.

Deposition of VO_2 powder using Spin Coater

After annealing the obtained VO_2 particles, synthesized via hydrothermal method were deposited onto precleared bare quartz substrate via spin coating technique. The spinning speed was 3000 rpm for 45 seconds. It was dried at 150 ^oC to remove the solvent, and as well as to stimulate the formation of VO_2 film. After the drying, the same process was repeat for two times more to fabricate the consequent layers of VO_2. After spinning as mentioned particular speed and time that films were annealed in a quartz tube furnace. The annealed atmosphere was maintained at 550 ^oC temperature in the controlled Argon gas flow of 100 standards cubic per centimeter (SCCM) through a mass-flow controller for 2 hours. After the annealing, we collect the final thin film of VO_2 which we used for further characterization.

Instrumentation

The ZEISS Sigma Field Emission Scanning Electron Microscopic (FESEM) was used to collect scanning electron micrographs.The optical analysis of the TF of VO_2 powder were performed by a UV-Vis-NIR spectrophotometer made by PerkinElmer (model: Lambda 365+) furnished with an integrating sphere. A custom-made stage was used in spectrophotometer to conduct in situ measuring temperature dependent transmission.

Results and Discussion

Field Emission Scanning Electron Microscopy (SEM) Analysis

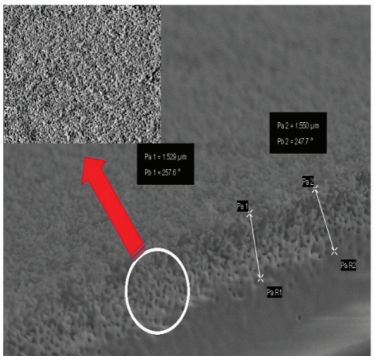

Figure-1: FESEM image of VO2 thin film.

Typical FESEM image of thin film of VO_2 powder samples were presented in Fig. 1. The thickness of thin film was measured ~ 1.5 µm, represented in Fig. 1. The inset of Fig. 1. Shows the homogenous distribution of synthesized materials

Temperature Dependent optical study of VO_2 Thin film

The thermochromic characteristic of the VO_2 thin film was analysed by measuring transmittance in a UV-vis spectrophotometer. The transmittance spectrums of VO_2 thin film represents vivid modifications in IR region (~800 nm - 1100 nm) as presented inset of Fig. 2 and indicate high-quality thermochromic properties.

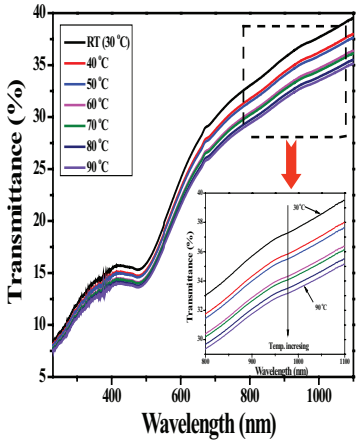

Figure-2: Temperature Dependent Transmittance spectrum and elaborated graph at IR region (inset) of VO_2 thin films.

According to the Fig. 2, the changes on transmittance with the temperature is minimum at the visible range. Whereas, at the NIR range that changes are clearly visible. From the transmission spectra, it can be found that the transmission at IR region (1100 nm) is 40% and 33% at 30 °C and 90 °C respectively. From the difference of transmittance, the thermochromic properties can be analysed. In this regard the hysteresis curve for a constant wavelength (1100 nm) as a function of temperature were obtained and then evaluated.

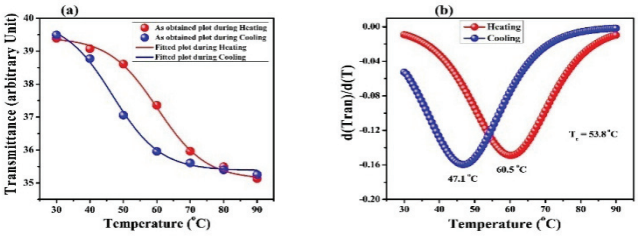

Figure-3:(a) Hysteresis loop of as obtained and fitted plot and (b) d(Tran)/d(T) vs. Temp curve for the VO_2 thin films at wavelength of 1100 nm.

Fig. 3(a) demonstrates the hysteresis curve due to thermal cycle generated during the observing transmittance of VO_2 thin film at 1100 nm. The hysteresis curve of VO_2 thin film presented with gentle slope. The transition was characterized by analysing the derivative of the Transmission in terms of

temperature (d (resistance)/dT). The results were fitted for both heating and cooling cycles (Fig. 3b). The lowest values of first-order differential of hysteresis loops were considered as the Semiconductor to Metal Transition temperature (T_{SMT}) in Fig. 3b. The transition temperature of heating (T_h) and cooling (T_C) process is found to be 60.5 °C and 47.1 °C, respectively. The thermal hysteresis, $\Delta T (T_h - T_C)$, define as the difference between the transition temperature obtained at heating and cooling cycle. For our fabricated thin film 13.4 °C is obtained as the thermal hysteresis. The T_{SMT}, average value of the transition temperature in heating and cooling cycles called as the phase transition temperature.

$$T_{SMT} = 1/2 (T_h + T_C)$$

Hence calculated value of T_{SMT} is 53.8 °C. In our experiment the obtained value of T_C is lower than that of the T_h.

These hysteresis characteristics highly correlated with propagation of MIT through grain boundaries [21]. The hysteresis difference of VO_2 thin film might be attributed with the film particulates.

Conclusion

This study presents a streamlined approach for synthesizing VO_2 (M) particles utilizing a one-step hydrothermal process. The resulting material was characterized by X-ray diffraction, affirming its single-phase nature. Remarkably, the thin film of VO_2 displayed the well-documented transition from semiconductor to metal behavior, elucidated through the temperature-dependent infrared transmittance measurements. These transmittance measurements revealed a striking phase transition profile, showcasing a nearly two-order-of-magnitude shift in transmittance. The critical parameters of this phase transition were determined, with the transition temperature (T_{SMT}) pinpointed at 53.08 °C and a corresponding thermal hysteresis (ΔT) of 13.4 °C. These findings collectively affirm the viability of the procedure in yielding highly crystalline VO_2 thin films with a uniform grain distribution. Furthermore, the acquired temperature-dependent transmittance data, along with the observed hysteresis change, unveil the intriguing optical switching properties inherent to our material. In summation, this study underscores the efficacy of the outlined methodology in producing high-quality VO_2 thin films while shedding light on their compelling optical characteristics.

REFERENCES

1. F. J. Morin, Oxides which Show a Metal-to-Insulator Transition at the Neel Temperature. Phys. Rev. Lett. 3 (1959) 34-36. http://dx.doi.org/10.1103/PhysRevLett.3.34.
2. B. Harbecke, Coherent and incoherent reflection and transmission of multilayer structures, Appl. Phys. B 39 (1986) 165-170. https://doi.org/10.1007/BF00697414.
3. S. Qin, Y. Fan, X. Qiu, G. Gou, K. Zhang, Q. Feng, G. Gan, W. Sun, Modulation of the Phase Transition Behavior of VO2 Nanofilms by the Coupling of Zr Doping and Thickness-Dependent Band Gap, ACS Appl. Electron. Mater. 4 (12) (2022) 6067–6075. https://doi.org/10.1021/acsaelm.2c01202.
4. A. E. Serebryannikov, A. Lakhtakia, G. A. E. Vandenbosch, E. Ozbay, Transmissive terahertz metasurfaces with vanadium dioxide split-rings and grids for switchable asymmetric polarization manipulation, Sci Rep 12 (2022) 3518. https://doi.org/10.1038/s41598-022-07265-6.
5. J. H. Park, J. M. Coy, S. Kasirga, C. Huang, Z. Fei, S. Hunter, D. H. Cobden, Measurement of a Solid-State Triple Point at the Metal–Insulator Transition in VO2, Nature 500 (2013) 431–434. doi: 10.1038/nature12425.
6. Z. Yu, Z. Wang, B. Li, S. Tian, G. Tang, A. Pang, D. Zeng, G. Sankar, Facile Solution Process of VO2 Film with Mesh Morphology for Enhanced Thermochromic Performance, Materials (Basel) 15 (2022) 4129. doi: 10.3390/ma15124129.
7. N. Inomata, T. Usuda, Y. Yamamoto, M. H. Zoellner, I. Costina, T. Ono, Effects of temperature and doping concentration on the piezoresistive property of vanadium dioxide thin film, Sensors and Actuators A: Physical 346 (2022) 113823. https://doi.org/10.1016/j.sna.2022.113823.
8. Y. Xuea, S. Yin, Element doping: a marvelous strategy for pioneering the smart applications of VO2, Nanoscale 14 (2022) 11054-11097. https://doi.org/10.1039/D2NR01864K.
9. N. Numan, I.G. Madiba, B.S. Khanyile, Z. M. Khumalo, M. Maaza, Hydrothermal synthesis and characterization of undoped and W-doped vanadium dioxide nanorods for thermochromic application, Journal of Crystal Growth 590 (2022) 126702. https://doi.org/10.1016/j.jcrysgro.2022.126702.
10. Y. Zhang, W. Xiong, W. Chen, Y. Zheng, Recent progress on vanadium dioxide nanostructures and devices: Fabrication, properties, applications and perspectives, Nanomaterials 11 (2021) 1–45. https://doi.org/10.3390/nano11020338.
11. J. Kim, T. Paik, Recent Advances in Fabrication of Flexible, Thermochromic Vanadium Dioxide Films for Smart Windows, Nanomaterials 11 (2021) 2674. DOI: 10.3390/nano11102674.
12. X. Li, C. Cao, C. Liu, W. He, K. Wu, Y. Wang, B. Xu, Z. Tian, E. Song, J. Cui, G. Huang, C. Zheng, Z. Di, X. Cao, Y. Mei, Self-rolling of vanadium

dioxide nanomembranes for enhanced multi-level solar modulation, Nature Communications 13 (2022) 7819. https://doi.org/10.1038/s41467-022-35513-w.

13. W. Zeng, N. Chen, W. Xie, Research progress on preparation methods of VO2 nanoparticles and its application in smart windows, Cryst Eng Comm 22 (2020) 851–869. https://doi.org/10.1039/C9CE01655D.
14. D. Zomaya, W. Z. Xu, B. Grohe, S. Mittler, P. A. Charpentier, Bimodal Size Distribution of VO2 Nanoparticles in Hydrophilic Polymer Films for Temperature-Triggered Infrared Transmission Control, ACS Appl. Nano Mater. 3 (2020) 6645. DOI: 10.1021/acsanm.0c01072.
15. C. Kindle, A. Castonguay, S. McGee, J. A. Tomko, L. D. Zarzar, Direct Laser Writing from Aqueous Precursors for Nano to Microscale Topographical Control, Integration, and Synthesis of Nanocrystalline Mixed Metal Oxides, ACS Appl. Nano Mater. 2 (2019) 2581–2586. DOI: 10.1021/acsanm.9b00360.
16. L. Li, H. Chen, Y. Shi, D. Xing, Human-Body-Temperature Triggerable Phase Transition of W-VO2@PEG Nanoprobes with Strong and Switchable NIR-II Absorption for Deep and Contrast-Enhanced Photoacoustic Imaging, ACS Nano 16 (2022) 2066–2076. https://doi.org/10.1021/acsnano.1c07511.
17. J. Zhou, Y. Gao, X. Liu, Z. Chen, L. Dai, C. Cao, H. Luo, M. Kanahira, C. Sun, L. Yan, Mg-doped VO2 nanoparticles: hydrothermal synthesis, enhanced visible transmittance and decreased metal-insulator transition temperature, Phys. Chem. Chem. Phys. 15 (2013) 7505–7511. https://doi.org/10.1039/C3CP50638J.
18. B. Mondal, P. K. Gogoi, Nanoscale Heterostructured Materials Based on Metal Oxides for a Chemiresistive Gas Sensor, ACS Applied Electronic Materials 4 (2022) 59-86. Doi: 10.1021/acsaelm.1c00841.
19. J. M. Gonçalves, M. I. da Silva, L. Angnesa, K. Araki, Vanadium-containing electro and photocatalysts for the oxygen evolution reaction: a review, J. Mater. Chem. A 8 (2020) 2171-2206. https://doi.org/10.1039/C9TA10857B.
20. R. Chen, L. Miao, C. Liu, J. Zhou, H. Cheng, T. Asaka, Y. Iwamoto, S. Tanemura, Sci. Rep. 5, 14087 (2015). https://doi.org/10.1038/srep14087.
21. J. Chaillou, Y-F. Chen, N. Émond, T. Hajlaoui, B. Torriss, K. D. Malviya, E. Orgiu, M. Chaker, ACS Applied Electronic Materials 4, 1841-1851 (2022). https://doi.org/10.1021/acsaelm.2c00080.

13

VO2 as Smart Material and its Application in Spacecraft Thermal Control Device

Subrata Saha, Arka Dey,Iman Biswas, Arjun Dey, Aniruddha Mondal

Abstract

Short description about properties of VO2, its various deposition techniques and applications presented. The requirement of space technology sector, challenges in thermal control of nano, micro satellites and new methods of thermal control is discussed. Recent progress in developing the smart radiative device also presented.

Keywords: electrical impedance tomography, EIT, gold electrode array, phantom, reconstructed image, EIDORS

Introduction

Vanadium dioxide (VO2) is a material that has been extensively studied due to its unique semiconducting to metallic phase transition behaviour near room temperature accompanied by a change in the crystal structure of VO2 from monoclinic to tetragonal that leads to substantial and a reversible alteration in its electrical resistivity, optical characteristics, and thermal properties. This transition can be induced by a range of external factors, including temperature,

stress, pressure, electric field, voltage, current, and even laser pulses. This extraordinary flexibility has spurred extensive research into unlocking and harnessing the unique properties of VO2 for a wide array of potential applications e.g., optical, electrical and ultrafast photonic switches, attenuators and modulators, resonators, spintronics, piezo-electricity, strain driven switches, non-volatile memory devices, Infrared (IR) bolometers, Optical filters, Smart radiative coatings for applications such as smart windows or spacecraft [**Haddad 2022**]. This article discusses a short review on deposition techniques of VO2, its application in various fields with the challenges, special requirement of space technology sector and recent progress in VO2 based smart devices by various groups.

Deposition techniques and challanges of VO2

Deposition Methods: VO2 thin film on various substrates can be deposited by chemical, physical and electro-chemical methods. Chemical methods include spin coating, chemical vapor deposition, hydrothermal methods, dip coating etc. The physical methods e.g., sputtering, e-beam evaporation, pulsed laser deposition, ion-beam deposition etc. can be used to deposit VO2 from vanadium (V), vanadium di-oxide (VO2), vanadium pentoxide (V2O5), vanadium nitride (VN) precursors in suitable environment. Post deposition annealing in controlled environment plays important role in controlling grain size, crystallinity, microstructure which is manifested in its transitional properties. A schematic diagram depicting the different routes to produce VO2 is shown in **figure 1**.

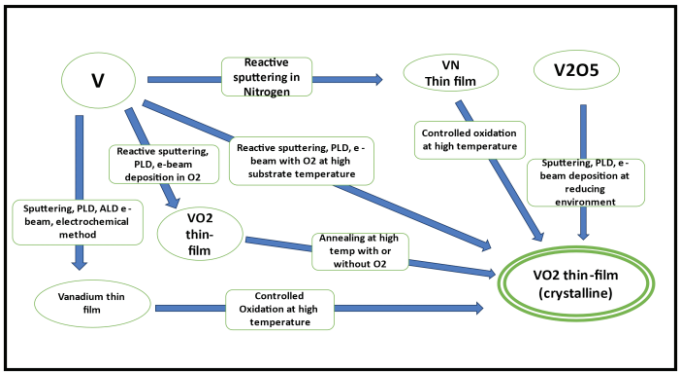

Figure-1: Schematic of VO2 deposition pathways

Challanges

Oxidative sputtering of V, and pulsed laser deposition of V in oxygen environment are well researched method to produce VO2. Though its high repeatability, the instruments involved are very costly. A substantial amount of research gap is there in producing high quality and uniform VO2 thin film from low-cost precursor on a large sized substrate. For the fields of applications e.g., smart window, smart radiation device for

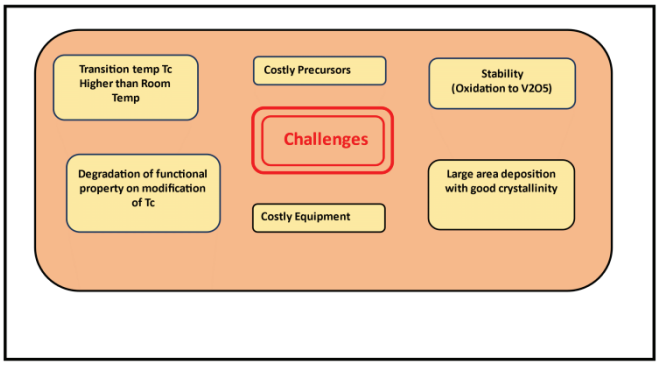

Figure-2: Challenges in VO2 deposition and potential application

spacecraft requires large area but uniform thickness. As the modern technologies emerging the need for miniaturisation is in high demand, one sector where requirement is the most is space technology sector. In space technology sector all the components should be robust, reliable, higher performance from small sized components is required.

Spacecraft thermal control and its challenges

One of the most crucial space technology segments is thermal control of satellite. Current thermal management of spacecraft and space systems is a subsystem of it, that greatly influences the overall performance and durability of space payloads. Spacecrafts experience a significant variation in external temperatures due to fluctuations in incident radiation, ranging from approximately -150°C in dark space to +150°C under direct solar radiation as shown in **figure 3**.

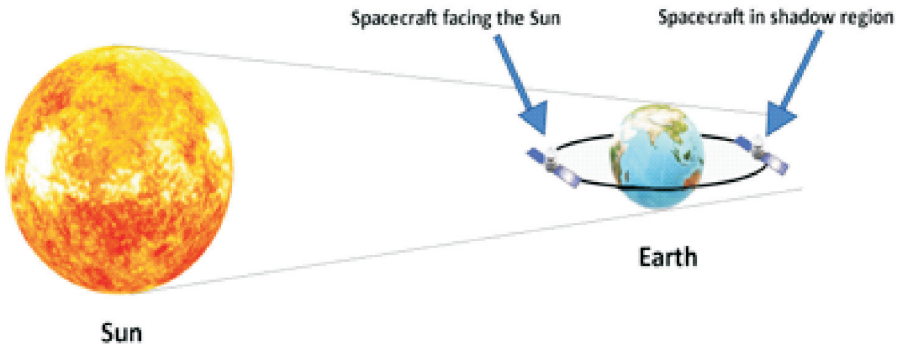

Figure-3: Spacecraft facing Sun (hot) side and Deep space (cold)

In addition due to this high temperature gradient, it becomes very critical to maintain different payloads of a spacecraft at their respective optimum temperature range typically between -10°C and 30°C. Thermal control of satellite is sub-divided into two types- active components and passive components. Active components like heaters, louvers, micro louvers, heat pipes play a vital role in controlling the temperature at cost of electrical power and increase in overall weight of the satellite. The chances of electrical and mechanical failure is there which may stop of reduce the overall functionality of the satellite.

Modern methods to cater the challenges in spacecraft thermal control

The development of miniaturized satellites, such as micro- and nano-satellites, requires smaller thermal control sub-systems. These spacecrafts are special satellites, designed to be much smaller and lighter than the traditional ones, demand unique thermal instrumentation compared to conventional.

To address these limitations, an innovative solution is proposed - "adaptive" or "smart" thermal control of spacecraft based on variable emittance coatings. These coatings can alter the effective infrared emissivity in response to external stimuli like temperature (thermochromic) or electric voltage (electrochromic), thereby regulating the radiative heat transfer rate. The added capability

of automatic modulation enhances their potential in meeting the specific requirements of miniaturized and highly crucial spacecrafts effectively. **(Gilmore 1994).**

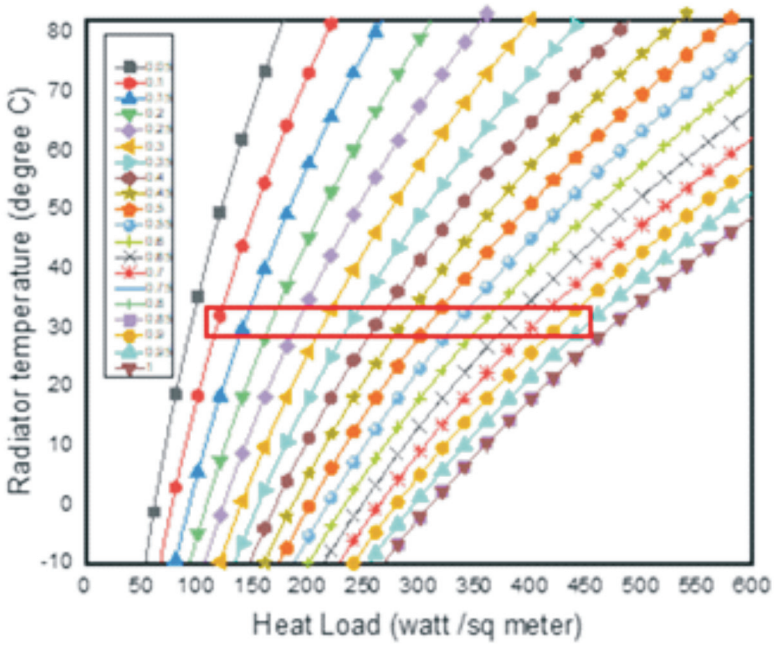

Figure-4: Radiator temperature vs heat-load at different emissivity surface

The steady state temperature of spacecraft can be expressed by the following energy balance equations (1) and (2)

$$SA_p\ \alpha = \sigma \varepsilon A T^4 \qquad \text{.....(1)}$$

$$T = \left[\frac{SA_p\ \alpha}{\sigma \varepsilon A} \right]^{1/4} \qquad \text{.....(2)}$$

where, T is the absolute temperature of the spacecraft, S is the solar constant (e.g., the yearly average value at Earth is 1366 W m-2), σ is the Stefan–Boltzmann constant (56.7×10-9 Wm-2 K–4), A_p is the projected surface area of the spacecraft perpendicular to solar rays, A is the total surface area of the spacecraft; α is the solar absorptance and ε is the thermal emittance

of the exposed surface.Basic understanding towards passive control relies on the equilibrium temperature of the radiator surface on different heat load for different intensity. [Figure 4]. It is understandable that is emissivity of the radiator may be varied from 0.2 to 0.8 it can possibly maintain the spacecraft temperature with a heat load varied from 100 W/m2 to 400 W/m2 (In actual situation this range may be different based on other factors).

Currently, three primary micro-mechanical miniaturization methods are under consideration:

MEMS micro louvers **(Osiander et al., 1999**),

Micro heat pumps **(Birur et al., 2001),**

Electrostatic thermal switches **(Biter et al., 2002).**

These are some recent works by few research groups presented in table 1.

Table -1

Device structure	Emissivity Switching	Reference
VO2/Si	0.28	[Saitzek2008]
VO2/Ag periodic staking layer	0.53 (simulated)	[Voti 2013]
VO2/SiO2/Al/Quartz substrate	0.48, Alpha solar=0.43	[Hendaoui2013]
V00.989W0.021O2/SiO2/Al/Quartz substrate	0.43	[Hendaoui2013]
VO2/HfO2/Ag/Si Substrate	0.55	[Wang2015]
Au/BaF2)/m-VO2/Si substrate	0.46	[kim2019]
CeO2/SiO2)/V0.98W0.02O2/CeO2/Ag/Si	0.38	[Dudon2021]
a-Si/SiO2/VO2/SiO2/Au/Quartz	0.46 Alpha sol= 0.28	[Hendaoui2022]

Conclusions

It is understandable that smart radiator device is the best solution to replace many current technologies in spacecraft specially for micro or nano satellites. It is clearly understandable there is lack of studies in achieving the performance of the smart radiator device in commercial aspect. To realise it the objectives towards the target should be

1. Adopt and optimize the deposition methods to deposit VO2 on large area.

2. Deposition temperature also needed to reduce so that a large variety of flexible substrates, eg. FEP, Polyimide (Kapton) or polyimide sheets etc.
3. Though some results showed improved tuneability obtained with a special interface layer, still the required tunability to cater large heat load variation still remained locked.

And the final aspect is the reduction of cost. The overall process to development of SRD should be done keeping in mind to use easily available materials, low-cost fabrication techniques, scalability of the process etc.

REFERENCES

1. Haddad E, Kruzelecky RV, Murzionak P, Jamroz W, Tagziria K, Chaker M and Ledrogoff B (2022) Review of the VO2 smart material applications with emphasis on its use for spacecraft thermal control. *Front. Mater.* 9:1013848. doi: 10.3389/fmats.2022.1013848
2. Osiander, R., Champion, J., Darrin, M., Allen, J. J., Douglas, D., and Swanson, T.(1999). Micro-machined shutter arrays for thermal control radiators on ST5. AIAA-2002-0359. doi:10.2514/6.2002-359
3. Birur, G. C.,Waniewski Sur, T., Paris, A., Shakkottai, P., Green, A., Haapanen, S., et al. (2001). "Micro/nano spacecraft thermal control using a MEMS-based pumped liquid cooling system"," in Presented at SPIE conference on Micromachining and Microfabrication, San Francisco, USA, October 21-24, 2001.
4. Biter, W., Oh, S., and Hess, S. (2002). "Electrostatic switched radiator for space based thermal control," in Proceedings of the Space Technology and Applications International Forum; (STAIF), Albuquerque, NM.
5. Gilmore, D. G. (1994). Satellite thermal control handbook. El Segundo, California: The Aerospace Corporation Press
6. Sébastien Saitzek, Frédéric Guinneton, Guillaume Guirleo, Laurent Sauques, Khalifa Aguir, Jean-Raymond Gavarri,
7. VO2 thin films deposited on silicon substrates from V2O5 target: Limits in optical switching properties and modeling,
8. Thin Solid Films,Volume 516, Issue 6,2008,Pages 891-897,https://doi.org/10.1016/j.tsf.2007.04.129.
9. *R. Li Voti, MC Larciprete, GL Leahu, M. Bertolotti, C. Sibilia,* Optimization of thermochromic VOR2-based structures with tunable thermal emissivity,*Nanoforum 2012 - VIII edition, pp.23-33, DOI: 10.1393/ncc/i2013-11504-8*
10. A. Hendaoui, N. Émond, S. Dorval, M. Chaker, E. Haddad,

11. VO2-based smart coatings with improved emittance-switching properties for an energy-efficient near room-temperature thermal control of spacecrafts, Solar Energy Materials and Solar Cells, Volume 117, 2013, Pages 494-498, https://doi.org/10.1016/j.solmat.2013.07.023.
12. Xiao Wang, Yunzhen Cao, Yuzhi Zhang, Lu Yan, Ying Li,
13. Fabrication of VO2-based multilayer structure with variable emittance, Applied Surface Science, Volume 344,
14. 2015, Pages 230-235, 0169-4332, https://doi.org/10.1016/j.apsusc.2015.03.116.
15. Kim, H., Cheung, K., Auyeung, R.C.Y. *et al.* VO_2-based switchable radiator for spacecraft thermal control. *Sci Rep* **9**, 11329 (2019). https://doi.org/10.1038/s41598-019-47572-z
16. Jean-Paul Dudon, Corinne Marcel, Laurent Dubost, Alice Ravaux, Pierre-Henri Aubert, et al. Development of variable emissivity coatings for thermal radiator. *ICES 2021 - 50th International Conference on Environmental Systems*, Jul 2021, Virtual event, United States. (hal-03327635)

14

Exploring the Performance of AuNi/MWCNT Anode Catalyst in Direct Methanol Fuel Cell

Chandan Kumar Raul, Soumen Basu, and Ajit Kumar Meikap

Abstract

This study presents a comprehensive investigation into the performance of AuNi/MWCNT (Gold-Nickel/Multi-Walled Carbon Nanotube) composite catalysts as anode candidates in direct methanol fuel cell (DMFC). The need for effective and sustainable energy sources has spurred research into improving the catalytic activity of anode materials for DMFC. In this study, the synthesis, characterization, and electrochemical evaluation of AuNi/MWCNT catalysts are discussed. The results demonstrate the promising potential of these catalysts for enhancing the performance of DMFC, highlighting their significance in the pursuit of cleaner and more efficient energy conversion technologies.

Keywords: Bimetallic, electrocatalyst, MWCNT, DMFC, Electrooxidation

Introduction

Direct methanol fuel cells (DMFCs) have gained considerable attention as a promising alternative for portable and stationary power applications due to their high energy density, low operating temperature, and reduced environmental impact. The anode electrocatalyst plays a crucial role in the electrochemical oxidation of methanol, significantly affecting the overall DMFC performance

[1-5].In this context, bimetallic catalysts have garnered substantial attention due to their ability to tune electrocatalytic properties by altering the composition and structure of the catalyst. Gold (Au) and nickel (Ni) are two metals that have shown promising catalytic activity for methanol oxidation. Combining these metals as bimetallic nanoparticles supported on carbon nanotubes (CNTs) holds great potential for achieving enhanced catalytic performance. Multi-Walled Carbon Nanotubes (MWCNTs) serve as an ideal support material due to their high surface area, excellent electrical conductivity, and chemical stability [6-8]. The combination of Au and Ni with MWCNTs, denoted as AuNi/MWCNT, presents a potential catalyst for enhancing methanol oxidation kinetics.

Materials and Methods

Materials and reagent

MWCNT (length:10-30 μm and diameter:<8 nm) was purchased from SRL Pvt. Ltd. $HAuCl_4$ was purchased from LOBA CHEMIE PVT.LTD. $Ni(NO_3)_2.6H_2O$, $NaBH_4$, $C_6H_5Na_3O_7.2H_2O$,KOH, NaOH, C_2H_5OH, $C_2H_6O_2$was purchased from MERCK, India.

Catalyst Synthesis

The AuNi/MWCNT catalystis synthesized using two step reduction technique. Fig. 1 illustrates the synthesis procedure of AuNi/MWCNT electrocatalyst.

Characterization

The physical characterization of prepared electrocatalyst is carried out using various techniques, including scanning electron microscopy (SEM), X-ray diffraction (XRD), and energy-dispersive X-ray spectroscopy (EDS), to investigate their morphology, crystal structure, and elemental composition.

Electrochemical Evaluation

Electrochemical performance was assessed using a standard three-electrode electrochemical cell setup(PGSTAT302N, Autolab, Metrohm Electrochemistry Workstation) with the synthesized AuNi/MWCNT catalysts as the working electrode. Cyclic voltammetry (CV), electrochemical impedance spectroscopy (EIS) and chronoamperometry (CA) measurements were conducted to evaluate

the catalyst's electrocatalytic activity and stability.

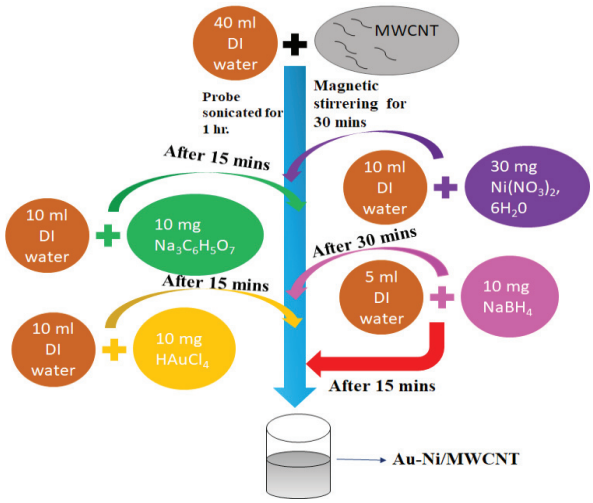

Figure-1: Synthesis route of Au-Ni/MWCNT Np's

Results and Discussion

Fig. 2 displays the XRD micrograph of prepared electrocatalyst. In the catalysts, the first pronounced diffraction peak appeared at an angle of 2θ=25.84°, signifying its association with the (002) hexagonal graphite structures present in Multi-Walled CarbonNanotubes (MWCNT) with a JCPDS No. of 75-1621. The remaining five prominent diffraction peaks, located at approximately 2θ=38.6°, 44.51°, 64.69°, 77.82°, and 82.04°, precisely matched the crystallographic planes of face-centered cubic gold: (111), (200), (220), (311), and (222), respectively. This alignment demonstrated a strong agreement with the well-established gold diffraction patterns.The prominent peaks observed in AuNi/MWCNT closely matched those of Au/MWCNT, even though there were no discernible diffraction peaks attributable to either nickel or its oxide. This phenomenon is likely attributed to the selective crystallization of gold atoms within the AuNi nanoparticles, while nickel remains in an amorphous state as adsorbed Co atoms on the gold crystal, as suggested in previous studies [2]. The presence of nickel has been further confirmed through Energy-Dispersive X-ray Spectroscopy (EDS) analysis. The calculated average crystallite size (D) is 10 nm using Debye – Scherrer formula[2],

$$D = \frac{K\lambda}{\beta \cos\theta} \qquad (1)$$

where K is a constant = 0.94, β is the FWHM, λ is thewavelength of X-ray(1.54 for Cu Kα radiation).

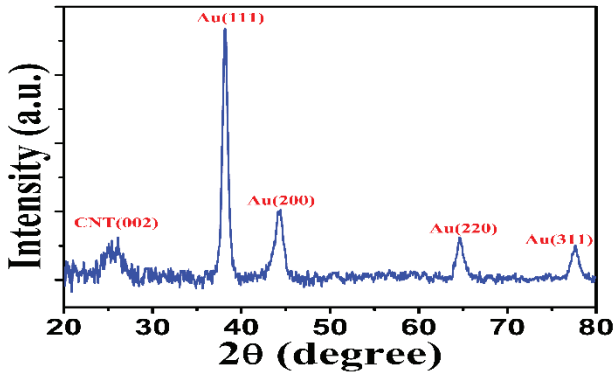

Figure-2: Room temperature XRD configuration of the sample

Fig. 3 shows the SEM image of the catalyst where a uniform distribution of spherical gold particles is observed.

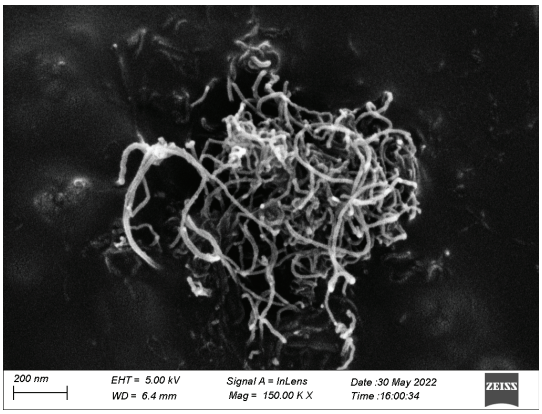

Figure-3: SEM image of the sample

Fig. 4 displays the energy dispersive X-ray (EDX) pattern of synthesized catalyst. From this spectra, the existence of Au, Ni, C and O is confirmed.

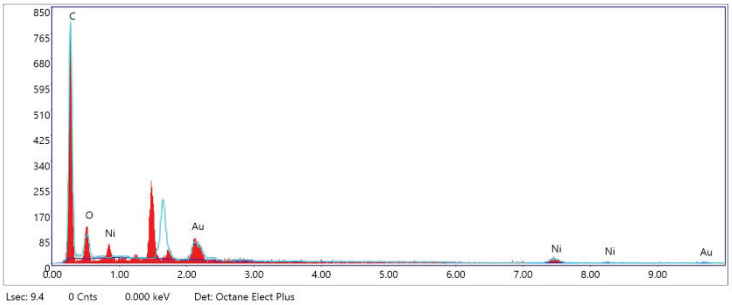

Figure-4: EDX spectra of the sample

Figure 5 depicts the CV curves obtained within a solution comprising CH_3OH and KOH at 100 mV/s. In the process of methanol oxidation, methanol undergoes complete oxidation to form CO_2 (or CO_3^{2-}) as indicated by equations (2-4) [6-8].

$$CH_3OH + 8OH^- \rightarrow CO_3^{2-} + 6H_2O + 6e^- \quad (2)$$

$$CH_3OH + 5OH^- \rightarrow HCOO^- + 4H_2O + 4e^- \quad (3)$$

$$HCOO^- + 3OH^- \rightarrow CO_3^{2-} + 2H_2O + 2e^- \quad (4)$$

During the forward scan, a distinct and broad oxidation peak at approximately 0.35 V was observed, which can be attributed to the presence of recently chemisorbed methanol. Conversely, in the reverse scan, we observed a distinct oxidation peak at 0.1 V, signifying the elimination of partially oxidized carbonaceous compounds that persisted from the preceding forward scan [7-9]. The initiation of this potential shift occurred at approximately -0.1 V, with the peak potential reaching its maximum at 0.3 V during the methanol oxidation process in alkaline environment.The specific activity of the preapared catalyst is 46 $mA.cm^{-2}$.

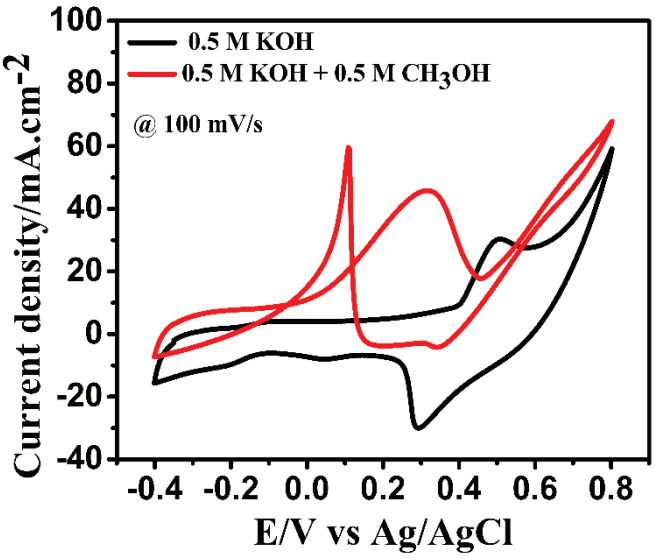

Figure-5: CV study of the sample at 100 mV/s scan rate

Fig.6 shows the EIS spectra recorded in 0.5 M KOH and 0.5 M CH_3OH solution. EIS offers a robust method for studying the rate of charge transfer in electrochemical reactions.The plots, particularly in the high-frequency domain, exhibited a distinctive arc-shaped pattern. In regard to catalytic performance, the magnitude of this impedance arc is directly linked to the charge transfer resistance (Rct) at the electrolyte-electrode

interface. In the Electrochemical Impedance Spectroscopy (EIS) plot, we can discern a semicircular impedance arc within the high-frequency region. Its size corresponds to the resistance encountered in the transfer of electrons at the boundary between the electrode and the electrolyte solution during the process of methanol oxidation. In the low-frequency region, we observe Warburg impedance, indicative of diffusion control. Notably, there is no linear impedance observed at lower frequencies in Figure 8. This finding highlights the fundamental importance of charge transfers at the electrode/electrolyte interface and provides further evidence of a charge-transfer-limited process. A smaller impedance arc diameter signifies a decreased R_{ct} value, a pivotal element contributing to the improved electron transfer kinetics and electrical conductivity of an electrocatalyst [3-5,7,9]. The calculated values of solution resistance (R_s) is 22.89 ohms and R_{ct} is 212 ohms.

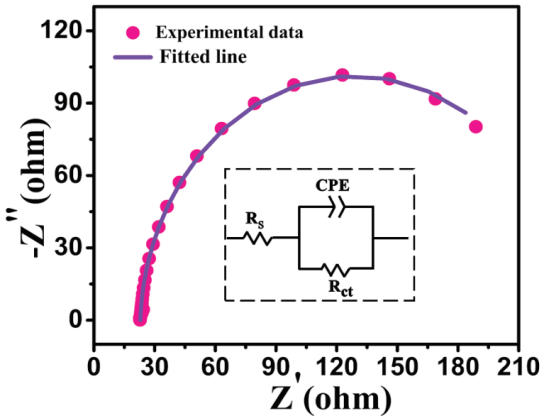

Figure-6: EIS spectra of the sample at potential 0.4 V (Inset shows corresponding equivalent circuit)

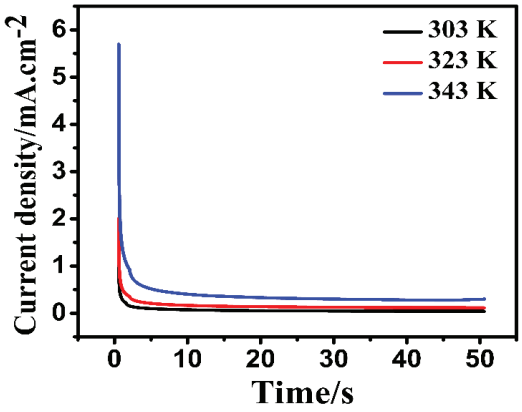

Figure-7: CA curve of the sample

To assess the catalysts' resilience against poisoning, we perform CA experiment, and the result is presented in Figure 7. The outcome suggests that the incorporation of nickel into the Au-based catalyst enhances the ability of Au/MWCNT to withstand poisoning during methanol oxidation. So, the CA curve suggests the stability of prepared catalyst [4,7-9].

Conclusions

Here, MWCNT supported Gold-Nickel bimetallic electrocatalyst is successfully synthesized by simple chemical reduction method. The prepared AuNi/MWCNT electrocatalyst showed highest peak current density (46 $mA.cm^{-2}$) and lowest charge transfer resistance (212 ohms) as compared to Au/MWCNT. These findings suggest that AuNi/MWCNT could serve as a highly promising candidate for anode catalysts in direct methanol fuel cells.

REFERENCES

1. Yan, S., Gao, L., Zhang, S., Gao, L., Zhang, W. and Li, Y., 2013. Investigation of AuNi/C anode catalyst for direct methanol fuel cells. *International journal of hydrogen energy*, *38*(29), pp.12838-12846.
2. Raul, C.K., Dey, S., Halder, M., Karmakar, R., Basu, S. and Meikap, A.K., 2023. Synthesis of AuxCo100– x/MWCNT nanoparticles as an efficient anode electrocatalyst for borohydride oxidation in alkaline medium. *Journal of Applied Electrochemistry*, *53*(5), pp.977-990.
3. Ali, S., Khan, I., Khan, S.A., Sohail, M., Ahmed, R., ur Rehman, A., Ansari, M.S. and Morsy, M.A., 2017. Electrocatalytic performance of Ni@ Pt core–shell nanoparticles supported on carbonnanotubes for methanol oxidation reaction. *Journal of Electroanalytical Chemistry*, *795*, pp.17-25.
4. Chen, W., Zhang, Y. and Wei, X., 2015. Catalytic performances of PdNi/MWCNT for electrooxidations of methanol and ethanol in alkaline media. *International Journal of Hydrogen Energy*, *40*(2), pp.1154-1162.
5. Borkowska, Z., Tymosiak-Zielinska, A. and Nowakowski, R., 2004. High catalytic activity of chemically activated gold electrodes towards electro-oxidation of methanol. *Electrochimica acta*, *49*(16), pp.2613-2621.
6. Hsieh, C.T. and Lin, J.Y., 2009. Fabrication of bimetallic Pt–M (M= Fe, Co, and Ni) nanoparticle/carbon nanotube electrocatalysts for direct methanol fuel cells. *Journal of Power Sources*, *188*(2), pp.347-352.
7. Sarwar, E., Noor, T., Iqbal, N., Mehmood, Y., Ahmed, S. and Mehek, R., 2018. Effect of Co Ni ratio in graphene based bimetallic electro catalyst for methanol oxidation. *Fuel cells*, *18*(2), pp.189-194.

8. Kaur, A., Kaur, G., Singh, P.P. and Kaushal, S., 2021. Supported bimetallic nanoparticles as anode catalysts for direct methanol fuel cells: A review. *International Journal of Hydrogen Energy*, *46*(29), pp.15820-15849.
9. Maya-Cornejo, J., Garcia-Bernabé, A. and Compañ, V., 2018. Bimetallic Pt-M electrocatalysts supported on single-wall carbon nanotubes for hydrogen and methanol electrooxidation in fuel cells applications. *International Journal of Hydrogen Energy*, *43*(2), pp.872-884

15

Investigation on resistive memory of sequentially vapour deposited $Cs_2AgBiBr_6$

Iman Biswas and *Aniruddha Mondal*

Abstract

In this study, we have developed a memristor device utilizing $Cs_2AgBiBr_6$-based material. We employed a three-step thermal evaporation method to create a thin-film of $Cs_2AgBiBr_6$, and subsequently examined its phase purity and film quality through XRD and SEM analyses. Additionally, the optical properties were explored via UV-Vis absorption spectra, revealing an optical bandgap of approximately 2.0 eV. Finally, we conducted a comprehensive investigation of the I-V characteristics of the Au/$Cs_2AgBiBr_6$/ITO device across 100 cycles to assess the resistive memory's stability and reversibility.

Keywords: double perovskite, sequential vapour deposition, resistive memory, halide memristor, I-V hysteresis

Introduction

The explosion of data storage has driven widespread research into resistive random-access memory (RRAM) due to its simple structure, non-volatility, and low power consumption.[1–3] The cross-bar array structure, known for high storage density, is seen as a potential solution to overcome the von Neumann bottleneck.[4–7] Memristors, or memristive systems, have been introduced as the

fourth basic circuit element, conceptually symmetrical with resistors, inductors, and capacitors, as proposed by Leon Chua.[8]The human brain shows an absolute advantage over modern computers due to its highly parallel computation and ultralow power consumption.[9]Synaptic plasticity is essential for learning and memory.[10]Thememristor (short for memory resistor) is a two-terminal circuit element characterized by a pinched hysteresis loop inthe I–V plane and plastic resistance.[11] Hence, the memristorcan work as an artificial synapse and offers novel applications in neuromorphic computing,[12-13] information storage,[14]and hardware security.[15]Halide perovskite materials, exemplified by $CH_3NH_3PbI_3$ ($MAPbI_3$), have shown potential for RRAM devices, with point defects like interstitials, vacancies, and cation substitutions forming shallow defect levels in $MAPbI_3$'s valence and conduction bands.[16-17] However, lead halide perovskites suffer from stability and lead toxicity issues.[18-19] $Cs_2AgBiBr_6$, with its excellent structural stability, resistance to heat and moisture, and cubic double perovskite structure, emerges as a promising alternative among these materials.[20-21] Despite its potential, $Cs_2AgBiBr_6$ has primarily been considered for light harvesting applications.

Herein, we investigated the resistive memory properties of sequentially vapor-deposited $Cs_2AgBiBr_6$ thin-film for the first time. We measured the I-V characteristics of an Au/$Cs_2AgBiBr_6$/ITO device over 100 voltage sweeping cycles and examined the memory's stability and reversibility during 30 minutes of continuous sweeping.

Materials and Methods

The $Cs_2AgBiBr_6$ double perovskite thin-film (DPTF) was synthesized via a three-step evaporation process in a thermal evaporator (Pro-Vac, India). Initially, a 2 cm × 1 cm glass plate coated with Indium Tin Oxide (ITO) served as the substrate, which was cleaned sequentially with acetone, isopropanol, and distilled water, then dried with N_2 gas. This cleaned substrate was then positioned on the substrate holder inside the TE chamber. Subsequently, we evaporated the precursors—Silver Bromide (AgBr, ≥ 99%, Sigma Aldrich), Bismuth (III) Bromide ($BiBr_3$, ≥ 98%, Sigma Aldrich), and Cesium Bromide (CsBr, ≥ 99.99%, Sigma Aldrich)—onto the substrate in a layer-by-layer fashion at a 1:1.5:2 molecular weight ratio.The substrate holder rotated continuously at 300 rpm during each deposition to ensure film uniformity. Chamber pressure was maintained at ~8×10^{-6} mbar throughout the depositions. Afterward, we annealed the as-grown samples in a quartz tube furnace at 573 K for 10 hours

under a constant flow of Argon (Ar) gas (100 SCCM). The DPTF transitioned from light yellow to bright yellow after annealing. Finally, we deposited gold (Au) dot electrodes with an area of ~ 0.03 cm^2 on the $Cs_2AgBiBr_6$ DPTF within the vacuumed TE chamber. Figure 1 illustrates the fabrication process flow of DPTF PD.

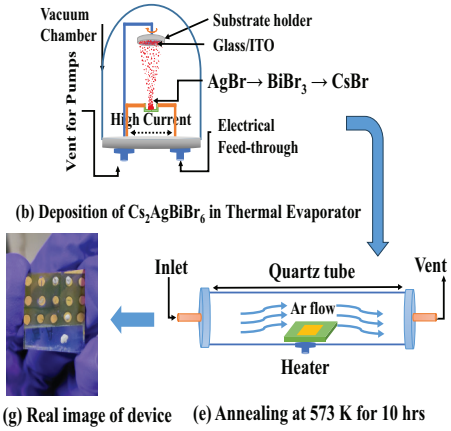

Figure-1: Process Flow for fabricating the $Cs_2AgBiBr_6$ Double Perovskite Thin-Film (DPTF) Device.

Results and Discussion

Structural Characterisations

The crystal structure and phase purity of the DPTFs were studied using X-ray diffraction (XRD) with Brucker Advanced equipment and Cu Kα radiation (1.54 Å wavelength). The peaks shown in Figure 3(a) are in good agreement with the standard JCPDS (File number: 01-084-8699), suggesting a cubic structure (α= 11.26Å), which is consistent with previously reported data.[22-23]The (#) indicates the position of reflections from the side phases AgBr ((JCPDS:6-438) and $Cs_3Bi_2Br_9$ (JCPDS:01-070-049), respectively. Average crystallite size was calculated to be ~ 190 nm from Debey-Scherrer equation.[24]

The surface morphology and film thickness of the synthesized DPTF were analysed with a Carl ZEISS Sigma field emission gun-scanning electron microscope (FEG-SEM) shown in Figure 2(b). The cross-sectional view image shows two successive layers: the bottom layer being the Indium Tin Oxide

(ITO) substrate and the top layer being the thermally deposited DPTF, both around 800 nm thick.

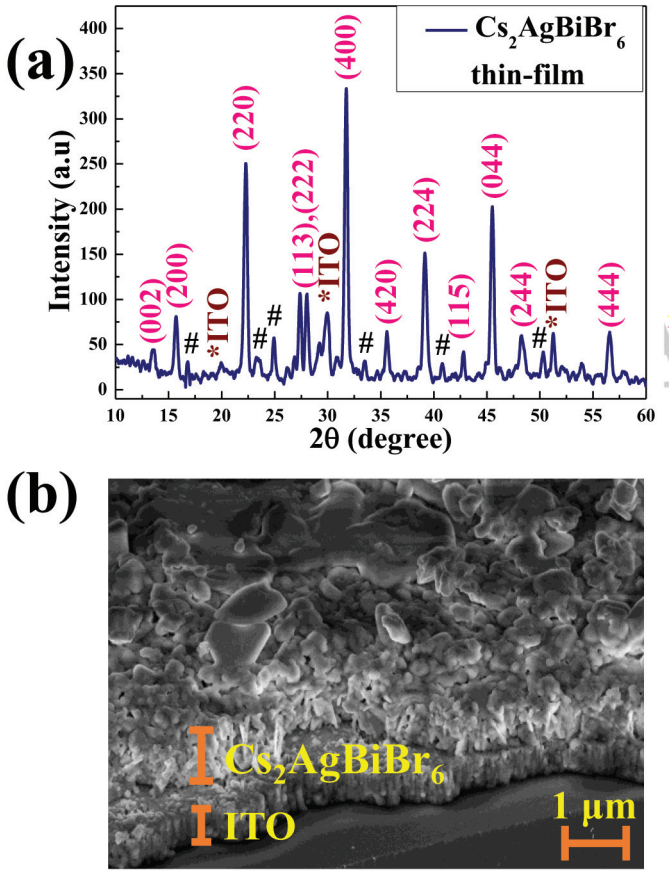

Figure-2: (a) XRD pattern of DPTF**(b)**FESEM image of synthesized $Cs_2AgBiBr_6$/ITO.

Optical Characterisation

Optical properties of the synthesized DPTF were explored by PerkinElmer Lamda365+ UV-Visible absorption spectrometer in the 400-1100 nm range shown in Figure 3.Tauc's equation was utilized,[25] with *n*= for indirect bandgap to calculate the bandgap shown in inset of Figure 3. The optical bandgap was calculated to be ~ 2.0 eV, which corresponds absorption in visible range.

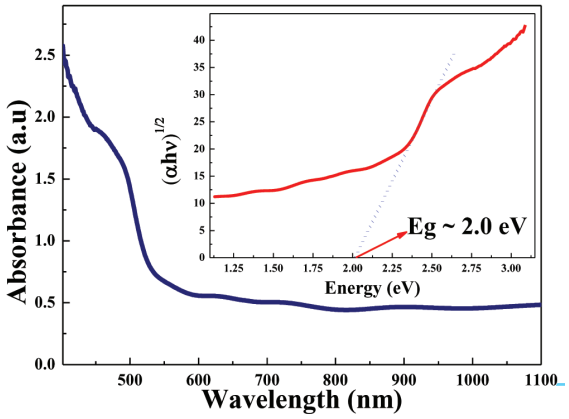

Figure-3: UV-Visible absorption spectra[Tauc's plot for bandgap calculation in the inset]

Electrical Response

The I-V characteristics of the device is measured by a Keithley 2450 source meter unit (SMU) by sweeping the voltage from -5V to 5V. The ITO was connected to (-ve) terminal was the SMU and Au-dot electrode was connected to the (+ve) terminal of the SMU. A persistent hysteresis was observed on both side of the device with more prominent separation in the current at (+ve) voltages. To ensure the stability of the device, we ran up to 100 cycles of I-V data and the device was working fine. A typical I-V characteristics of the device with 100 cycles is shown in Figure 4.

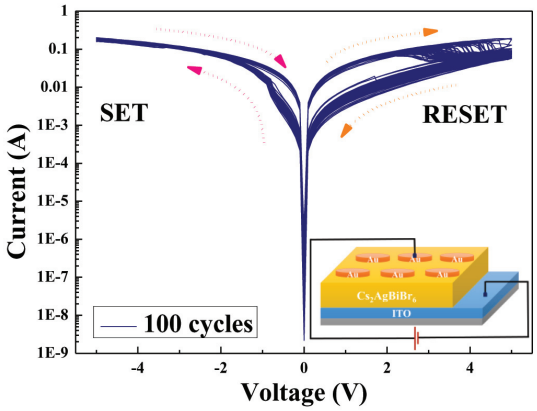

Figure-4: I-V Characteristics of the device with 100 cycles [Schematics of our working device in the inset]

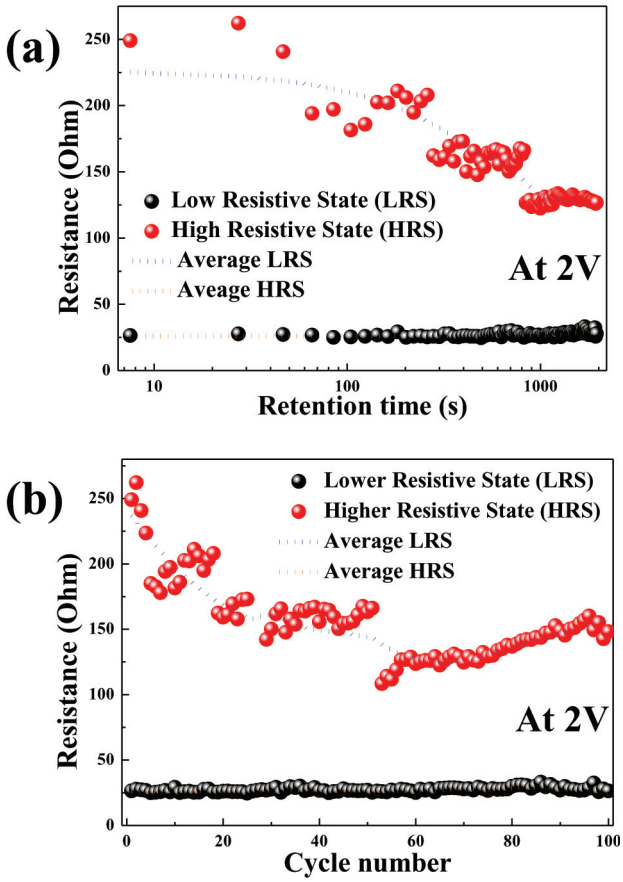

Figure-5: **(a)** Resistive memory with retention time **(b)** Resistive memory with cycle number

To get a better understanding of this memristor property, we took a voltage where the difference between the higher resistive state (HRS) and lower resistivity state (LRS) is maximum and analyse the stability of the resistive memory with time and cycle numbers. The memory retained its 50% value after 100 cycles and over 30 min. The values are promising to consider that no high dielectric media were used in our device. The resistive memory was solely due to the $Cs_2AgBiBr_6$ layer sandwiched between two dissimilar electrodes. This explains the asymmetric nature of the memory. The origin of this resistive memory can be associated with uneven distribution of Br atoms across the bulk of the material. The sweeping voltage between twocontacts separates electron from

the Br^- ion ($Br^0 + e^-$) and theBr ions diffuses from higher concentration region to lower concentration region. Due to the change in population of Br vacancies near the top and bottom metal electrodes, the Fermi level pinning between the halide perovskite layer and the metal is being altered resulting the set and reset condition. Therefore, we believe, by controlling the vacancy concentration and distribution, the results can be further improved. The HRS to LRS with cycle number and retention time is shown in Figure 5.

Conclusions

We successfully demonstrated the formation of $Cs_2AgBiBr_6$ thin-film by sequential evaporation method onto an ITO/Glass substrate. The phase purity and surface morphology were examined by XRD and SEM. The UV-Vis spectroscopy exhibited the material as a candidate for optoelectronic devices. The I-V characteristics revealed the property of a memristor with moderate set and reset values. The resistive memory was stable and reversible up to 100 cycles of voltage sweeping, with 50% retention of its resistive memory after 30 minutes. Further studies and experiments need to be performed in future to understand the characteristics of this relatively new material. The performance can be improved by fabricating two successive perovskite layers with different halogen concentrations sandwiched between two metal contacts. The material can be a potential candidate for digital memory, logic circuits, biological and neuromorphic systems like artificial synaptic devices.

REFERENCES

1. D. Akinwande, C. Huyghebaert, C.-H. Wang, M. I. Serna, S. Goossens, L.-J. Li, H.-S. P. Wong and F. H. L. Koppens,Nature, 2019, 573, 507–518.
2. Y. Liu, W. Yang, Y. Yan, X. Wu, X. Wang, Y. Zhou, Y. Hu, H. Chen and T. Guo, Nano Energy, 2020, 75, 104930.
3. S. Ham, S. Choi, H. Cho, S. I. Na and G. Wang, Adv. Funct. Mater., 2019, 29, 1806646.
4. N. R. Hosseini and J.-S. Lee, Adv. Funct. Mater., 2015, 25, 5586–5592.
5. F. Zhou, Z. Zhou, J. Chen, T. H. Choy, J. Wang, N. Zhang, Z. Lin, S. Yu, J. Kang, H.-S. P. Wong and Y. Chai, Nat. Nanotechnol., 2019, 14, 776–782.
6. H. Ling, M. Yi, M. Nagai, L. Xie, L. Wang, B. Hu and W. Huang, Adv. Mater., 2017, 29, 1701333.
7. J. Liang, Y. Feng, L. Liu, S. Li, C. Jiang and W. Wu, J. Mater. Chem. A, 2019, 7, 15960–15968.

8. L. Chua, IEEE Trans. Circuit Theory, 1971, 18, 507–519.
9. Ielmini D. Micro-electron Eng, 2018, 190, 4
10. Bliss T V P, Collingridge G L. Nature, 1993, 361(6407),31
11. Chua L. Resistance switching memories are memristors. Appl. Phys A, 2011, 102(4), 765
12. Yao P, Wu H, Gao B, et al. Fully hardware-implemented memristor convolutional neural network. Nature, 2020, 577(7792), 64
13. Cai F, Correll J M, Lee S H, et al. Nat Electron, 2019, 2(7), 290
14. Qian W H, Cheng X F, Zhou J, et al. InfoMat, 2019
15. Pang Y, Gao B, Lin B, et al. Memristors for hardware security applications. Adv Electron Mater, 2019, 5(9), 1800872
16. X. Zhu, J. Lee and W. D. Lu, Adv. Mater., 2017, 29, 1700527.
17. H. Chen, R. Hegde, J. Browning and M. D. Dadmun, Phys. Chem. Chem. Phys., 2012, 14, 5635–5641.
18. M. Grätzel, The light and shade of perovskite solar cells. Nat. Mater. 2014, 13, 838. https://doi.org/10.1038/nmat4065
19. P. V. Kamat, J. Bisquert, J. Buriak, ACS Energy Lett. 2017, 2, 904.https://doi.org/10.1021/acsenergylett.7b00246
20. F. Cao, L. Li, Adv. Funct. Mater. 2020, 31, 2008275. https://doi.org/10.1002/adfm.202008275
21. X. Yang, W. Wang, R. Ran, W. Zhou, Z. Shao, Energy & Fuels 2020, 34, 10513. https://doi.org/10.1021/acs.energyfuels.0c02236
22. N. Daem, J. Dewalque, F. Lang, A. Maho, G. Spronck, C. Henrist, P. Colson, S. D. Stranks, R. Cloots, *Solar RRL*2021**,** *5*, 2100422. https://doi.org/10.1002/solr.202100422
23. G. Abiram, F. H. Gourji, S. Pitchaiya, P. Ravirajan, T. Murugathas, D. Velauthapillai, Sci. Rep. 2022, 12, 2455. https://doi.org/10.1038/s41598-022-06319-z
24. P. Scherrer, Göttinger Nachrichten Gesell., Vol. 2, 1918, p 98.
25. Tauc, J. (1968). Materials Research Bulletin. 3: 37–46. doi:10.1016/0025-5408(68)90023-8.

16

Low Temperature Characteristics of Ga_2O_3 NWs based Schottky Diode

Ankita Choudhury, Iman Biswas and Aniruddha Mondal

Abstract

In this article, the growth of Ga_2O_3 nanowires (NWs) by electron beam evaporation method and analysis of its electrical properties has been reported. Au/ Ga_2O_3 NWs based devices on Si substrate was fabricated. The optical band gap (Eg) for both the Ga_2O_3 NWs was estimated to be 3.1 eV and 4.1 eV from UV-Vis spectrum. The temperature dependence current (I)–voltage (V) characteristics of Ga_2O_3 based device shows a gradual decrease of conductivity with the decrease of temperature. The temperature dependent ideality factor of Ga_2O_3 NWs devices was studied. Here, Ideality factor decreases and Barrier height increases linearly with decreasing temperature. A decrease in the ideality factor and an almost linear increase in the barrier height are observed with the increasing temperature. The calculated series resistance of Ga_2O_3 NWs based device also shows an anomalous increasing behaviour with the increasing of temperature.

Keywords: Au/Ga_2O_3 NWs,Low temperature, Electron beam evaporation,Schottky diode.

Introduction

High Performance Power Switching Semiconductors (HPPs) are in high demand in Renewable Energy Systems (RE), Smart Grid Systems (SWG), Transportation Electrification (TEN), Electric and Hybrid Electric Vehicles (HEV), Industrial Machinery Control (IMC), Power Generation, Military Systems (MPS), Power Electronics (PES) [1]. Power Electronics are responsible for Con Trolling and Converting Electrical Power to Provide the Perfect Conditions for Transmission, Distribution, and Load-side Consumption. Renewable energy accounted for more than half of all new power capacity added worldwide in 2015 [2]. In these new applications as well as in existing applications such as consumer chargers forsmartphones, laptops and TVs, there is a growing interest in the use of SiC/GaN power devices [3]. Ga_2O_3 has a large breakdown field of approximately 8 M.V.cm^{-1}, which has attracted a lot of interest in power converters based on WBG (4.5 eV-4.9 eV) [4] semiconductors that are more efficient, lightweight and reliable [5]. Ga_2O_3 is a promising candidate for high voltage, low frequency conditions [6]. Bulk crystal growth of monoclinic β-Ga_2O_3 is relatively well advanced and large area wafers are commercially available.Wide bandgap semiconductor switches, like Ga_2O_3, have higher power densities, higherefficiency, low-cost melting method and thermal tolerances than Si, reducing the need for costly bulky cooling systems [7]. A major drawback of Ga_2O_3 is its low thermal conductivity. This might be mitigated by transferring devices to another substrate or thinning down the substrate and using a heatsink as well as top-side heat extraction, as used for GaN [8]. Thermally stable Schottky contacts for these rectifiers are also needed to ensure stability in power conversion systems [9]. For instance, in order to realize high quality devices, investigation of metal/β-Ga_2O_3 contacts is extremely important. In 2017 He et al. investigated the Schottky barrier height was estimated at temperatures ranging from room temperature to 150 °C [10]. In 2019 Fares et al. reported on the electrical effects of vertical Ga_2O_3 diodes using Au as the metal contact before and after device operation up to 500 °C. Instead of this, there is a lack of thermally stable schottkey diode at low temperature [11].

In this paper, we report on the electrical conductivity of vertical Ga_2O_3 diodes using Au as the metal contact within the temperature ranges from room temperature to 25K. We have demonstrated the low temperature effect on Ga_2O_3 nanowires (NWs) based device. We have analyzed the temperature-dependent electrical properties of this device by measuring some device parameters like barrier height ($_b$), ideality factor ( ), and series resistance (Rs) to understand

the low temperature stability of Ga_2O_3 NWs based Schottky device. This type of low temperature device is very useful in a cold weather emergency, Security system, to stop microbial growth and proliferation and also pharmaceuticals and biotechnology industry [12].

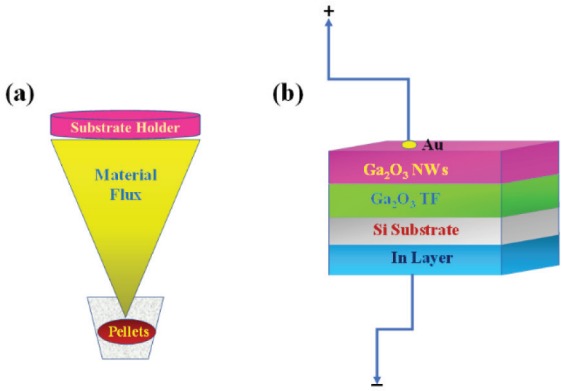

Schematic-1: Schematic representation of the fabrication procedure of the Ga_2O_3 NWs device using E-beam evaporation technique.

Materials and Methods

We have deposited Ga_2O_3 Nanowires (NWs) on P-type Si (100) substrate (1 – 30 Ω cm) in Ted Pella (USA). The schematic diagram of the device fabrication process using the EB (Electrobeam Evaporation) method is shown in Fig. 1. Pellets are prepared using 99.99% Ga_2O_3 nanopowder. The pellet preparation method is described elsewhere. As-prepared, the pellet is air-annealed at a temperature of about 250 °C in free air for a period of 30 min. The annealed pellet is placed in a Graphite crucible within the EB chamber. The E-beam evaporation method is used to deposit thin films (TFs) on the P-type Si substrate (100). The base pressure of the EB chamber is maintained at approximately 10^{-6} mbar. The evaporation rate is kept constant at a constant rate of about 1.2 Å /s (observed from Digital Thickness Monitor (DTM)). Then we fabricated Ga_2O_3 nanowires (NWs) of length >65 nm on TFs at the same deposition rate and at0 the same base pressure. GLAD (EB Evaporation cum Glancing Angle deposition) is a physically vapor deposition technique that offers the nano-structures for a wide variety of optical and electrotechnical applications. Three-dimensional nano-structures can be fabricated using this system. In this process, substrates are held on substrate holders at 85° angle and the deposition rate was 20 rpm. Then In are deposited on the substrate back. Circular gold

(AU) contacts (Diameter >1.2 mm) are deposited on top of the grown NWs through Al mask using GLAD (Thermal Evaporation technique). The device area is approximately 1.13×10^{-2} cm^2. The process is described elsewhere. After that, Sample is annealed for 30 min duration at oxygen environment of 250 °C.

Results & Discussion

Structural characterization

Field Emission Scanning Electron Microscopy (FESEM, Carl ZEISS Sigma, NIT Durgapur) was used for confirmation of growth of the NWs. crystalline structure was determined by XRD (Brucker Advanced) to confirm the beta phase of the device. To obtain the optical bandgap (Eg) the reflectance spectra of the NWs were recorded using a UV–vis (PerkinElmer Lambda 365+) spectrophotometer. For the measurement of the temperature-dependent electrical properties of the Au/Ga2O3/p-Si/In device a Keysight (B2912A) precision source/measure unit was used.

Fig. 1 (a) and (b) shows the FESEM top-view images and cross-section views (45° tilting) of our deposited Ga_2O_3 NWs to confirm the height and width of the grown NWs.

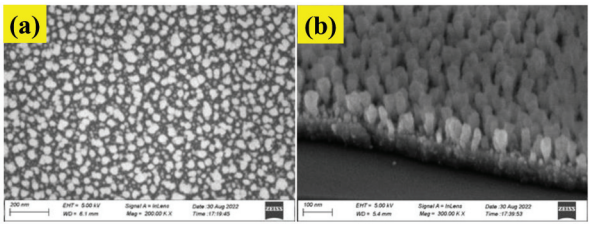

Figure-1: FE-SEM images of Ga2O3 NWs (a) top view and (b) cross sectional view.

B. Electrical characteristics of the Schottky diode

Fig. 2 (a) shows the C-V curves for Au/Ga_2O_3 NWs/p-Si/In device at 1 MHz frequency at 25 K. The room temperature C-V measurements were performed by sweeping the applied voltage from −10 V to +10 V. Three different regions are distinctly visible as shown, namely inversion, depletion and accumulation regions. The accumulation capacitance for Au/Ga_2O_3 NWs/p-Si/In device at 1 MHz frequency is ~5.94 nF. The background concentration is determined from C-V measurements. The free carrier concentration (Nd) for the device is calculated from the slope of the linear fit of the (b) $1/C^2$-V plot at room temperature. The calculated values of Nd are 4.1×10^{17} cm^{-3} for the device.

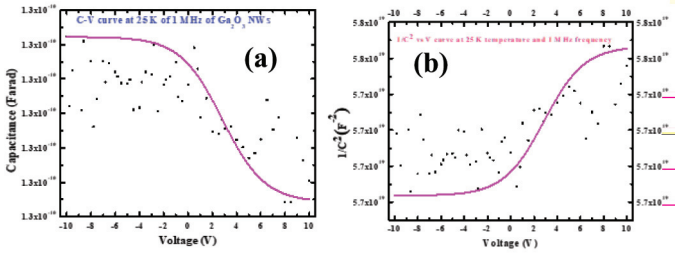

Figure-2: (a) C-V characteristics and (b) $1/C^2$ vs. V Curve of Ga_2O_3 NWs based device.

Fig. 3. shows the semi-logarithmic dark and light I–V characteristics of the Au/Ga_2O_3 NWs/p-Si Schottky diode over a wide temperature range (300 K–25 K).

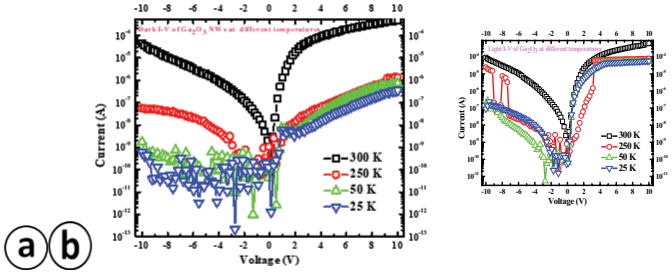

Figure-3: Temperature dependent dark (a) and (b) Light I–V characteristics (semi-logarithmic) of Au/Ga_2O_3 NWs/p-Si/In device over the temperature range 300 K - 25 K.

The I-V graphs of the Ga_2O_3 NWs based devices are shown in Fig. 3(a) and 3(b). Here, the current gradually increases with the increase of experimental temperature. It is quite a normal phenomenon, which can be described using the thermionic effect. Here the charge carriers can easily overcome the barrier by thermionic emission process after collecting energy from the supplied field or can tunnel through the thin metal-semiconductor interface of the device.

Considering the standard thermionic emission (TE) theory, for V > 3 kT/q, where q is the electronic charge, k is the Boltzmann constant, T is the absolute temperature of measurement, the diode characteristics are governed by (Eq. 1)

$$I = I_0 \exp\left(\frac{qV}{\eta KT}\right) \quad (1)$$

where I_0 indicates the reverse saturation current, which is obtained from the straight-line intercept of (ln I) -V curve and is defined by (Eq. 2) [13]

$$I_0 = AAT^2 exp\left(\frac{-q\phi B}{kT}\right) \quad \text{…….. (2)}$$

where η is the ideality factor of the diode, A is the effective area of the diode (≈ 1.13 × 10^{-2} cm^2),Φ_b is the barrier height and A* being the effective Richardson constant. The I_0 value is extracted from the intercept of the linear section of the (ln I) -V plot. This value is used to calculate Φ_b at different temperature. Higashiwaki et al. in 2016 reported the value of the A* (=55 A/cm^2 K^2) for Ga_2O_3 [6]. The ideality factor is extracted from the slope of the linear fit of the (ln I)-V plot in forward bias (near zero bias voltage)using (Eq.3):

$$\eta = \left(\frac{q}{KT}\right)\left[\frac{dv}{dln(I)}\right] \quad \text{…….. (3)}$$

Also, $_b$ is determined using the (Eq. 4)

$$\phi_B = \left(\frac{KT}{q}\right) ln\left[\frac{AA*T^2}{I_o}\right] \quad \text{…….. (4)}$$

The calculated values of η and Φ_b for Au/Ga_2O_3 NWs/p-Si /In Schottky diode are plotted in Fig. 4(a) for all temperatures.

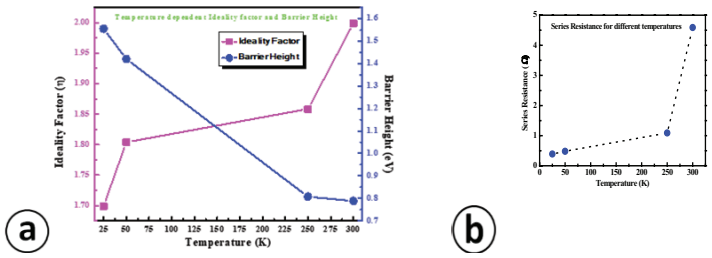

Figure-4: (a) variation in ideality factor (η) and barrier height with temperature for Au/Ga_2O_3 NWs/p-Si/In device and (b) series resistance of both undoped and doped devices.

Here, Ideality factor varies from 1.99 (300 K) to 1.69 (25 K) i.e decreases with temperature and Barrier height varies from 0.78 eV (300 K) to 1.55 eV (25 K); increases linearly with temperature. A decrease in the ideality factor and an almost linear increase in the barrier height are observed with the increasing temperature. The lowering ideality factor of the device from room

temperatures to 25K implies the decreasing of hole trapping with the deceasing of temperatures [14]. As shown in Table, the apparent ideality factor and the barrier height were found to be strongly temperature dependent and consistent with the earlier study [15].

Table 1: Comparative study among morphological parameters.

Temperature (K)	Ideality factor (η)	Barrier Height (Φ_b) (eV)	Series resistance (R_s) (Ω)
300	1.99	0.78	4.59
250	1.85	0.80	1.09
50	1.80	1.42	0.48
25	1.69	1.55	0.39

For this device, the barrier height values increased when the temperature was decreased (Fig. 4(a)). This phenomenon can be explained by the phenomenon of barrier inhomogeneity at the junction [16]. From Fig.4(b), it can be clearly shown that for the device the series resistance (R_s) increases with increasing temperature. So, in our case, Rs is strongly temperature-dependent. Generation of a large number of free carriers from the interface defect levels and also the oxygen vacancies for Ga_2O_3 decreases the R_s gradually with decreases temperature. This phenomenon increases the energy difference between the conduction band minimum and the Fermi level and a decrease in the probability of tunnelling [17]. For this reason, R_S increases with increase in temperature for this device.

Conclusions

In conclusion, we have fabricated the Ga_2O_3 NWs by GLAD assisted electron beam evaporation method. The Ga_2O_3 NWs device is found to be a more ideal Schottky device at the low temperature range. In this device ideality factor decreases with decreasing temperature due to the decreasing of hole trapping at 25 K. Here, barrier height also increases with decreasing temperature due to barrier inhomogeneity at the junction. So, generation of large no of carriers at the interface level decreases the series resistance made the device more ideal at 25 K.

REFERENCES

1. Lee W., Li S., Han D., Sarlioglu B., Minav T. A., and Pietola M., A Review of Integrated Motor Drive and Wide-Bandgap Power Electronics for High-Performance Electro-Hydrostatic Actuators, IEEE Trans. Transportation Electrification, 4(2018), 684.
2. Johnson M., Wilson P. R., Empringham L., and Lillo L. D., IEEE ITRW Working Group Position Paper-Packaging and Integration: Unlocking the Full Potential of Wide-Bandgap Devices, IEEE Power Electronics Magazine, 5(2018), 26.
3. BacaA. G., ArmstrongA. M., AllermanA. A.,DouglasE. A., SanchezC.A., KingM. P., ColtrinM. E., FortuneT. R., and KaplarR. J., An AlN/$Al_{0.85}Ga_{0.15}N$ high electron mobility transistor, Appl. Phys. Lett., 109(2016), 033509.
4. Rafique S., Han L. and Zhao H., Ultrawide Bandgap β-Ga_2O_3 Thin Films: Growths, Properties and Devices. ECS Transactions, The Electrochemical Society, 80 (7) (2017)203-216.
5. MastroM. A., KuramataA., CalkinsJ., KimJ., RenF., and PeartonS. J., Perspective—Opportunities and Future Directions for Ga_2O_3, ECS J. Solid State Sci. Technol., 6,(2017) 356.
6. HigashiwakiM., KonishiK., SasakiK., GotoK., NomuraK., ThieuQ. T., TogashiR., MurakamiH., KumagaiY., MonemarB., KoukituA., KuramataA., and YamakoshiS., Current status of Ga_2O_3 power devices, Appl. Phys. Lett., 108(2016) 133503.
7. GalazkaZ., UeckerR., KlimmD., IrmscherK., NaumannM., PietschM., KwasniewskiA., BertramR., GanschowS., and BickermannM., Scaling-Up of Bulk β-Ga_2O_3 Single Crystals by the Czochralski Method, ECS J. Sol. State Sci. Technol., 6(2017)3007.
8. AndersonT. J., HobartK. D., TadjerM. J., KoehlerA. D., ImhoffE. A., HiteJ. K., FeygelsonT. I., PateB. B., Eddy Jr.C. R., and KubF. J., Nanocrystalline Diamond Integration with III-Nitride HEMTs, ECS J. Solid State Sci. Technol. 6 (2017) 3036.
9. MohamedM., IrmscherK., JanowitzC., GalazkaZ., ManzkeR., and FornariR., Schottky barrier height of Au on the transparent semiconducting oxide β-Ga_2O_3, Appl. Phys. Lett., 101 (2012) 132106.
10. He Q., Mu W., Dong H., Long S., Jia Z., Lv H., Liu Q., Tang M., Tao X., and Liu M.,Schottky Barrier Rectifier Based on (100)β-Ga_2O_3 and its DC and AC Characteristics, Appl. Phys. Lett., 110 (2017) 093503 .
11. Fares C., Ren F., and Pearton S. J., Temperature-Dependent Electrical Characteristics of β-Ga_2O_3 Diodes with W Schottky Contacts up to 500 C. ECS Journal of Solid State Science and Technology, 8 (7) (2019) 3007-3012.
12. AndersonR.L., HillJ.L., Low temperature electronics,Microelectronics Journal,19(4) (1988) 7-12.

13. .Choudhury A., Dalal A., Dwivedi S.M.M.D., Ghosh A., Halder N., Das S., Mondal A., Vapour transport grown photosensitive GeO_2 thin film, Materials Research Bulletin, 142 (2021) 111397.
14. GhoshA., MondalA., DasA., ChattopadhyayS., ChattopadhyayK. K., Removal of oxygen related defects from chemically synthesized In_2O_3 thin film doped with Er by spin-on technique, Journal of Alloys and Compounds. 695 (2017) 1260-1265.
15. Demir H. O., Caldıran Z., Meral K., ***Sahin*** Y., Acar M., Aydogan S., The effect of temperature on the electrical characterization of a poly(phenoxy-imine)/p-silicon heterojunction, e-Polymers.16 (1) (2016) 75–82.
16. DeyA., JanaR., DharJ., DasP., RayP.P., Gaussian Distribution of Inhomogeneous Barrier Height of Al/ZnS/ITO Schottky Barrier Diodes, Mater. Today: Proc.5 (2018)9958–9964.
17. Lin Y. J., Origins of the temperature dependence of the series resistance, ideality factor and barrier height based on the thermionic emission model for n-type GaN Schottky diodes, Thin Solid Films. 519 (2010) 829–832.

17

MXene – a 2D Material for Next Generation Energy Storage Application

Anurup Chakraborty

Abstract

The global demand for energy has seen a remarkable rise over the course of the last two decades. Accordingly, both energy harvesting and storage sectors have seen great revolutions in recent years. Batteries and supercapacitors are the frontiers in energy storage sectors. Among various new materials, MXenes, a family of metal carbides, nitrides and carbonitrides, have shown great potential in energy storage applications due to their attractive electrical and electrochemical properties. In this short article, we present a brief overview of different synthesis routes of MXenes and their composites as potential energy storage materials.

Keywords: MXene, Supercapacitor, Battery

Introduction

These days, environment and energy are global topics of discussion. More and more attention is being paid to the extraction and application of new energy resources like wind and solar energy. However, for uninterrupted power supply, development in energy storage technologies is crucial because renewable energy technologies like wind and solar electricity are unpredictable and discontinuous. Electrochemical energy storage devices like Lithium-

ion battery, sodium ion battery and electrochemical supercapacitors are considered to be promising technologies for storage of energy.

Two-dimensional (2D) materials have undergone extensive research since the first experimental realisation of graphene in 2004 owing to their distinctive physical and chemical characteristics. After graphene, several other numerous atomic-layer materials have also been produced in laboratories, including hexagonal BN, transition metal dichalcogenides (TMDs), silicene, germanene, and phosphorene. [ref]

In the year 2011, a group of scientists in Drexel University led by Prof. Yury Gogotsi have discovered a very interesting family of 2D materials consisting of nitrides, carbides, carbonitrides which they named as MXene [1,2]. Metal come under the family of MXene. MXenes have a general formula $M_{n+1}X_nT_x$ where M stands for transition metal (i.e Ti,Nb,Mo,Hf e.t.c) and X stands for carbide and nitride and T is the surface tramination group (e.g F,OH,O e.t.c). 2D material graphene is synthesized from graphite similarly MXene is also synthesized from its parent ternary carbide or nitride MAX by chemical etching.

1. Synthesis:

1.1 HF etching:

HF etching is the oldest method discarded by the scientist. Most of the synthesis protocol reported etching with 10 to 50 wt% of HF [4,5,6]. Mohamed Alhabeb [7] et.al have shown an systematic study with different concentration of HF from 5 wt% to 30 wt%. in general using low concentration acid is much more effective for different applications as the flakesizeremains large. They showed that with higher time even 5 wt% of HF can etch aluminium properly.

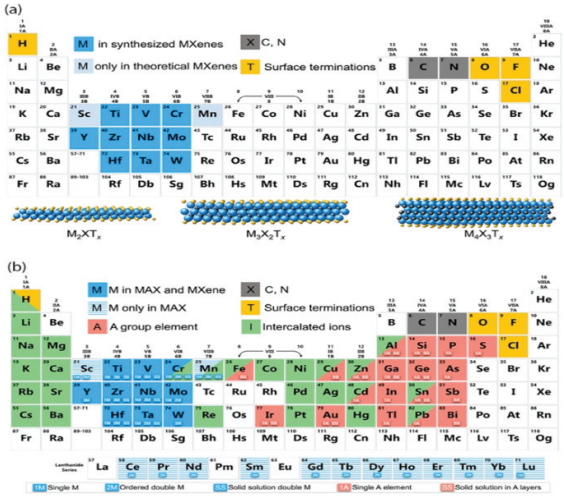

Figure 1. Periodic tables showing compositions of MXenes and MAX phases. (a) Elements used to build MXenes. The bright blue elements represent MXenes that have not been yet experimentally confirmed. The schematics of three typical structures of MXenes are presented at thebottom. (b) Elements used to build MAX phases, MXenes, and their intercalated ions. The elements with blue striped background are onlyreported in MXene precursors (MAX phases), and their MXenes have not yet been synthesized. The elements on the red background are the Aelements in MAX phases that can potentially be selectively etched to make MXenes. The green background shows the cations that have beenintercalated into MXenes to date. As per the legend at the bottom, 1M and 1A indicate the formation possibility of a single (pure) transitionmetal and A element MAX phase (and MXene). SS indicates the existence of solid solutions in transition metal atomic planes (blue) or A element planes (red); 2M shows the formation possibility of an ordered double-transition metal MAX phase or MXene (either in-plane or out-of-plane. Reused with permission from ref [3]

1.2 LiF/HCl etching:

In recent time MXene synthesis with LiF/HCl is far more famous than HF because direct HF acid is hazardous to health. Mohamed Alhabeb [7] et.al have shown the etching with different molar ratio of HCl and LiF salt. They concluded that for 0.5g MAX 0.8g of LiF and 10 ml of 9M HCl is optimised ratio for proper synthesis of MXene.

Apart from this two methods etching with NH_4HF_2[8], is also explored and proven to be very effective. After etching delamination is very important step. Organic polar solvent like DMSO [6], TBAOH, TMAOH [9]are used to delaminate Mxene. Using LiF/HCl for synthesis is very effective as Li is intercalated so just simple shaking enough for delamination of Mxene sheets .

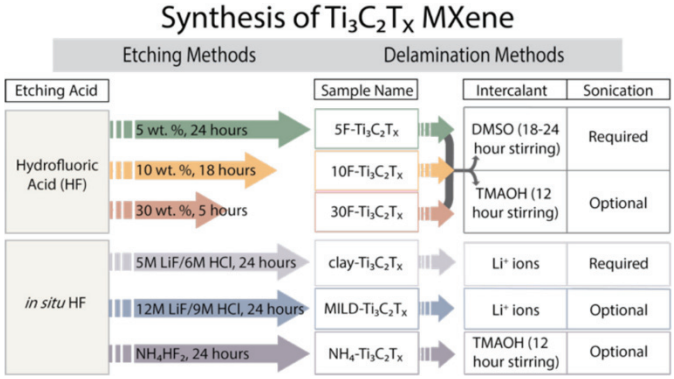

Figure-2: Different synthesis rout of Mxene. Reused with permission from ref[3]

Application

Mxene as Supercapacitor

The first application of Mxene investigated by the scientists was supercapacitive activity. Mxene has transition metal outside, which gives pesudocapacitive nature and the core is conductive carbon which provides supirior conductivity. So this material is a natural choice for supercapacitor application. Apart from this MXene shows good stability for M-X bond [10].

Wang et.al have synthesized MXene /nickel aluminium LDH composite [11]. The Ti_3C_2 material is used as conductive substrate and LDH layers have coated on MXene. So the electrons generated by the redox reactions, got a faster path way to reach the current collector. This MXene/LDH composite exhibits an higher capacitance of 1061F/g at 1A/g current density and a stability of 70% after 4000 cycles. Zhu et.al synthesized MXene/PPy freestanding electrode for supercapacitor application [12]. Polypyrrole (Ppy) flim suffers from poor mechanical stability and poor capacity. But in the composite Ppy is intercalated inside MXene layers, which makes it mechanically very stable . The bond between Ppy and MXene provide faster pathway for ion transport. The freestanding gives a good capacitance of208mF/cm^2 at 10mv/s and 100% capacity retention even after 20000 cycles

MXene as Battery

Liu et.al synthesized self assembled SnO_2 nanorod grown on the surface of the MXene[13]. The nanorods are self assembled to minimize their surface energy and makes ven der wall interaction with ,MXene. The syntergistic effect of transition metal oxide and MXene gives good performance for lithium ion storage of 720mAh/g at a currnt density 100mA/g. Lau et.al[14] have synthesize Sn^{2+} pillered Ti_3C_2 MXene for better sodium ion storage. The synthesis is done by a facile cetyltrimethylammonium bromide (CTAB) prepillaring (figure 4) followed by subsequent Sn^{2+} pillaring, serving as a stable matrix for high-performance dendrite-free Na metal anode. This material have a capacity of 100mAh/g at 2C.

Conclusions

MXene have emerged as a advanced material for energy storage devices than the other 2D materials. From the aspect of material synthesis for 2D material

the main focus is always to make the material thin using effective exfoliation technique. In case of MXene simple chemical etching can do the job. MXene have high surface area and high conductivity, which makes it a very efficient candidate for supercapacitor devices. The layer stacking of MXene helps the ion to intercalate and deintercalate easily and the high conductivity makes it a very good battery material. But still there are heavy challenges on the stability of MXene. There is a lot of scope to investigate and discover new way for energy storage with is newly discovered wonder material MXene.

REFERENCES

1. D. Chen, L. H. Tang, J. H. Li, Chem. Soc. Rev.2010, 39, 3157;
2. Tan, T. L.; Jin, H. M.; Sullivan, M. B.; Anasori, B.; Gogotsi, Y. High-Throughput Survey of Ordering Configurations in MXene Alloys Across Compositions and Temperatures. ACS Nano 2017, 11, 4407– 4418.
3. Gogotsi, Yury, and Babak Anasori. "The rise of MXenes." *ACS nano* 13.8 (2019): 8491-8494..
4.] Naguib, M.; Kurtoglu, M.; Presser, V.; Lu, J.; Niu, J.; Heon, M.; Hultman, L.; Gogotsi, Y.; Barsoum, M. W. Two-Dimensional Nanocrystals Produced by Exfoliation of Ti3AlC2. Adv. Mater. 2011, 23, 4248−53.
5. Naguib, M.; Gogotsi, Y. Synthesis of two-dimensional materials by selective extraction. Acc. Chem. Res. 2015, 48, 128–35.
6. Mashtalir, O.; Naguib, M.; Mochalin, V. N.; Dall'Agnese, Y.; Heon, M.; Barsoum, M. W.; Gogotsi, Y. Intercalation and delamination of layered carbides and carbonitrides. Nat. Commun. 2013, 4, 1716.
7. Alhabeb, Mohamed, et al. "Guidelines for synthesis and processing of two-dimensional titanium carbide (Ti3C2T x MXene)." *Chemistry of Materials* 29.18 (2017): 7633-7644.
8.] Feng, Aihu, et al. «Fabrication and thermal stability of NH4HF2-etched Ti3C2 MXene.» *Ceramics International* 43.8 (2017): 6322-6328
9. Ma, R. Z.; Sasaki, T. Two-Dimensional Oxide and Hydroxide Nanosheets: Controllable High-Quality Exfoliation, Molecular Assembly, and Exploration of Functionality. Acc. Chem. Res. 2015, 48, 136– 143.
10. S. Xu, G. Wei, J. Li, Y. Ji, N. Klyui, V. Izotov, W. Han, Binder-free Ti3C2Tx MXene electrode film for supercapacitor produced by electrophoretic deposition method, Chem. Eng. J. 317 (2017) 1026–1036
11. Y. Wang, H. Dou, J. Wang, B. Ding, Y. Xu, Z. Chang, X. Hao, Three-dimensional porous MXene/layered double hydroxide composite for high performance supercapacitors, J. Power Sources 327 (2016) 221–228

12. M. Zhu, Y. Huang, Q. Deng, J. Zhou, Z. Pei, Q. Xue, Y. Huang, Z. Wang, H. Li, Q. Huang, C. Zhi, Highly flexible, freestanding supercapacitor electrode with enhanced performance obtained by hybridizing polypyrrole chains with MXene, Adv. Energy Mater. 6 (2016), 1600969
13. Y. T. Liu, P. Zhang, N. Sun, B. Anasori, Q. Z. Zhu, H. Liu, Y. Gogotsi, B. Xu, Adv. Mater.2018, 30, 1707334;
14. Luo, Jianmin, et al. "Pillared MXene with ultralarge interlayer spacing as a stable matrix for high performance sodium metal anodes." *Advanced Functional Materials* 29.3 (2019): 180

18

Li-ZnO Thin Film Layer for Optoelectronic Device Applications: A Novel Derived Mathematical Model.

Sanat Kumar Das, Bibek Chettri, Prasanna Karki, Pronita Chettri, Bhakta Kunwar, Bikash Sharma

Abstract

We present a theoretical modelling for estimating the wavelength (λ) as a function of expected transmittance of crystalline or shapeless semiconductors and dielectric thin film layers for optoelectronic device applications. The given model develops the values of effective single oscillator energy (E0) of the undoped and Ag-zinc Oxide thin film layers with high agreement with existing theoretical models. We determined that when the Ag doping concentration in Zinc Oxide film layers increased from 0 % to 5 %, the effective single oscillator energy (E0) of Li-ZnO improved from 0.15 eV to 0.18 eV. Furthermore, we executed the new imitative model to reproduce other optical properties.

Keywords: Optoelectronic device, Refractive index, scattering energy, Nonlinear optical susceptibility, Doping

Introduction

Zinc Oxide (ZnO) thin films and nanostructures are promising candidates

for solar cell development and manufacture due to their high exciton binding energy (about 60 meV) [1-3]. Zinc Oxide is represented on the forefront of the edge list for optoelectronic and microelectronic devices due to its high thermal and automated consistency for the next generation [3].

The primary focus of this study is on the reliance of different properties (optical) of pure and Ag tampered with zinc oxide thin films on different Li concentrations for diverse applications such as lasers, sensors, absorption, and field emission devices [2,3].

Wemple -DiDomenico Model studies

The WDD single oscillator model is used to calculate the effective single oscillator energy (E_0) and dispersion energy (E_d) [1]. This model is based on three types of energies: E_0, E_d and h [4,5]. It introduces a physical examination of the examined quantities in Eq. (1).

$$(n^2 - 1) = \frac{E_d E_o}{E_o^2 - h\vartheta^2} \quad \ldots(1)$$

$$(n^2 - 1)^{-1} = \frac{E_o}{E_d} - \frac{1}{E_d E_o}\, h\vartheta^2 \quad \ldots (2)$$

$$\varepsilon_o = n_0^2 = 1 + \frac{E_d}{E_o} \ldots \quad \ldots (3)$$

E_d and E_0 provide an important role in determining the properties of ophthalmic materials for the design of dispersion and optical communication devices, which permit for the calculation of essential factors. The obtained values of E_0 and E_d can be used to calculate the dielectric constant and refractive index (0-frequency).

.By using the relation 4 and 5, We can additionally analyze M_{-I} and M_{-III}

$$E_o^2 = \frac{M_{-I}}{M_{-III}} \quad \ldots(4)$$

$$E_d^2 = \frac{M_{-I}^3}{M_{-III}} \quad \ldots(5)$$

Moments of the optical spectra of thin film layers are denoted by M_{-I} and M_{-III}.

After rearranging all the equation, it becomes:

$$(n^2 - 1) = \frac{S_o \lambda_o^2}{(1-\lambda_o^2)/\lambda^2} \quad \ldots(6)$$

From Table 1.1, we can analyze $\chi^{(I)}$ (linear optical susceptibility) values. The IIIrd-order optical susceptibility(nonlinear) $\chi^{(III)}$ and the refractive index (nonlinear) are articulated as [6,7],

$$x^{(III)} = 6.82 \times 10^{-15} \frac{E_d^4}{E_o^4} \quad \ldots (7)$$

$$n^2 = \varepsilon' = \varepsilon_\infty - \frac{1}{4\pi^2 \varepsilon_o} \left(\frac{e^2}{c^2}\right) \left(\frac{N_e}{m^*}\right) \lambda^2 \quad \ldots (8)$$

$$\varepsilon'' = \frac{1}{4\pi^3 \varepsilon_o} \left(\frac{e^2}{c^3}\right) \left(\frac{N_e}{m^*}\right) \left(\frac{1}{\tau}\right) \lambda^3 \quad \ldots (9)$$

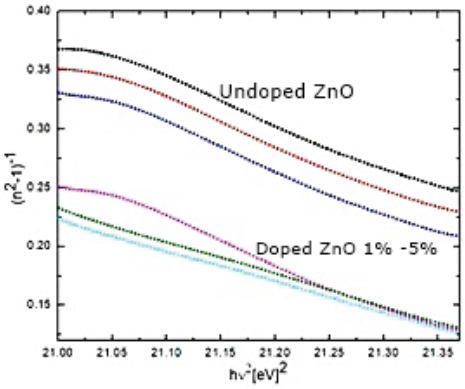

Figure-1.1 :versus of pure and Li (various doping concentration)– Zinc Oxide thin layers.

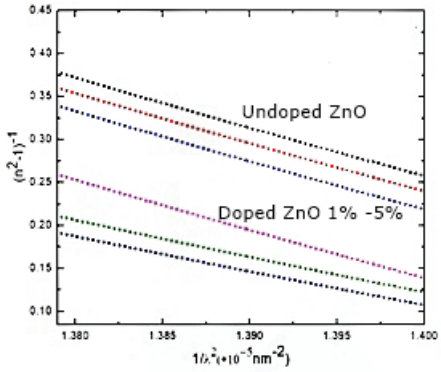

Figure-1.2:vs. of pure as well as Li (various doping concentration)– Zinc Oxide thin layers.

Where, e is the electronic charge, Nc is the charge transporter density, c is the light speed, ε″ is the imaginary part of the dielectric constant and m*(Carrier effective mass).Results.

Table 1.1: Different parameters for pure and Ag (15-5%) ZnO layers.

Sl. No	Parameter	Pure ZnO	1% Ag-ZnO	2% Ag-ZnO	3% Ag-ZnO	4% Ag-ZnO	5% Ag-ZnO
1.	E0 (eV)	0.125	0.142	0.149	0.161	0.174	0.179
3.	M–I	1.378	1.398	1.489	1.512	1.587	1.614
4.	$\chi^{(III)}$ 10-14 (esu)	1.235	2.325	4.279	14.135	25.245	34.146

Conclusion

We determined that increasing Ag concentration included (0 % to 5%) in Zinc Oxide thin film layers, E_0 increases from 0.125 eV to 0.179 eV, as predicted by the creation of stronger links among the components of the Li-doped thin films. Furthermore, the Ed increased from 2.425 eV to 3.264 eV, as seen in table 1.1. According to the same table, the dielectric constant (0-frequency) and refractive index of pure Zinc Oxide thin film layers are 2.345 and 3.141, respectively. When the Li strength is increased from 0% to 5 %, both metrics increase dramatically to 3.176 and 2.138, respectively.

Acknowledgements

The author (Sanat Kr. Das) acknowledges the TMA Pai University Research Fund-Award of Minor Grant, Sikkim Manipal Institute of Technology, Sikkim Manipal University, Sikkim (Sanction No.: 6100/SMIT/R&D/Project/12/2020, dated on 20th July 2020).

This work was supported by All India Council for Technical Education (AICTE) Govt. of India under Research Promotion Scheme for North-East Region (RPS-NER) vide ref.: File No. 8-139/RIFD/RPS-NER/ Policy-1/2018-19 (PI: Bikash Sharma).

REFERENCES

[1] Ü. Özgür, et al.: A comprehensive review of ZnO materials and devices.J. Appl. Phys. vol.98 , pp. 11 ,(2005).

[2] P. Wrobel, et al.: Plasmon-enhanced absorption in heterojunction n-ZnO nanorods/ p-Si solar cells. Metamaterials XII, International Society for Optics and Photonics, (2019).

[3] A.S. Hassanien, A.A. Akl,: Influence of composition on optical and dispersion parameters of thermally evaporated non-crystalline Cd50S50– xSex thin films.J. Alloys Compd. vol.648, pp. 280–290 ,(2015).

[4] P. Kumarasinghe, et al. Effect of post deposition heat treatment on microstructure parameters, optical constants, and composition of thermally evaporated CdTe thin films: Mater. Sci. Semicond. Process. vol. 58, pp. 51–60, (2017).

[5] E. Güneri, A. Kariper :Optical properties of amorphous CuS thin films deposited chemically at different pH values : J. Alloys Compd : vol. 516, pp.20-26 (2012) .

[6] H.A. Badran, et al.: Determination of optical constants and nonlinear optical coefficients of violet 1-doped polyvinyl alcohol thin film: Pramana, vol. 86 pp.1, (2016).

[7] M. Okutan, et al.: Investigation of refractive index dispersion and electrical properties in carbon nano-balls' doped nematic liquid crystals: Phys. B: Condensed Matter : vol.362, pp. 180-186, (2005).

Section 3

Sustainability and Energy

19

Rheological Investigation of Flow Parameter Around Circular Cylinders with a Single Groove at Low Reynolds Numbers Regime

Soumendu Gorai, Geeta Verma, Chandan Kumar Bharti, Rabindra Nath Burman

Abstract

In this study numerical simulationsusing the finite volume method were employed to analyze the flow characteristics of power- law based non-Newtonian fluids over a circular cylinder. This flow simulation was carried out to study the behavior of flow past a circular cylinder with a single groove. The flow was characterized at steady laminar flow at low Reynolds Number (10,20,30,40) with the shear thinning fluids (n=0.2 to 1). The flow physics around the cylinder was affected by the shape and size of the groove and their circumferential distribution. It was shown that the existence of a groove controls the dynamic behavior of the drag coefficients and wake length, depending on the shape of the groove and .The Drag Coefficient is less at groove cylinder than the smooth cylinder at all Reynolds number in n=0.2. And at groove cylinder, for shear thinning fluids, Wake length is increasing and for Newtonian fluid, Wake length is decreasing.

INTRODUCTION

When a fluid moves over a solid body. It exerts pressure force normal to the surface and shear forces parallel to the surface along the outer surface of the body. The component of the resultant of these two forces that acts in the flow direction is the Drag Force and that acts normal to the surface is known as the Lift Force [4]. To control this type of drag and lift force, some passive control techniques are used to have cylinder surface modification such as groove surface, which are generally square, triangular, dimple in shape.[1],[2] The objective of this work is to numerically investigate the flow around a circular cylinder with a square groove of identical depth and width at the position of in the anticlockwise sense in front of the cylinder. Here it is used in non-Newtonian shear thinning fluid at low Reynolds number regime (10,20,30,40). In this paper, the main intensity to compare the recirculation length and drag coefficient of smooth cylinder with the grooved cylinder.

METHODOLOGY AND NUMERICAL TECHNIQUES

It is considered a rectangular computational domain of 50D100D. And a cylinder of diameter D is located inside this domain. The cylinder has a square groove with k/D= 0.1, where k is the depth of the groove and D is the Diameter of the cylinder. Here it is considered as a diameter of the cylinder is 100mm.The walls of the domain are set as a slip wall and the walls of the cylinder are set to be in noslipcondition. The domain is rectangular in shape. The is the distance from the inlet of computational domain to the center of cylinder, is the distance between the center of cylinder and the outlet of computational domain. And is the vertical distance of the domain. numerical simulations are performed using the commercial software ANSYS Fluent and the equations are integrated by finite volume method by using a double precision method. The numerical model has been validated with the paper of [Dennis 1993], from which the present paper has been validated in the case Drag coefficient of smooth cylinder at Re 10 in all values on n (0.2-1). And in another case this paper has been validated with the works of [Dennis 1993] in the field of Wake length of smooth cylinder at Re 10, 20, 30, 40.The no of nodes of circular cylinder at the meshing have been considered as 93k after carrying out a domain independence test in the no of nodes at 58k,71k,93k and 112k.

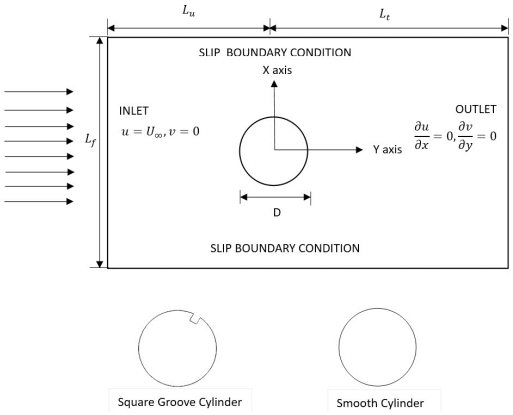

Figure1: Shape of the computational Domain

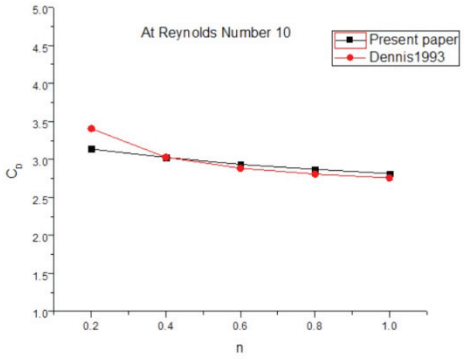

Figure 2: Validation of Drag coefficient a with present study with Dennis1993

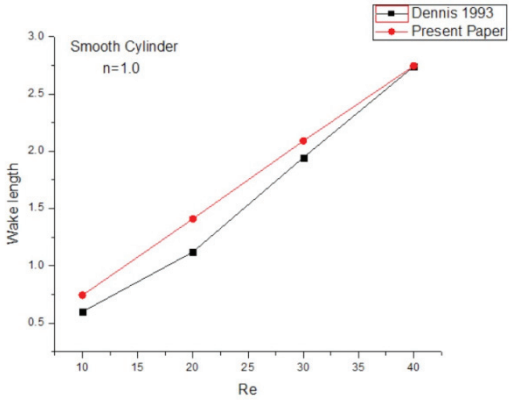

Figure 3: Validation of wake length with present study with Dennis1993

Result and Discussion

Drag Coefficients

In case of groove cylinder, the total drag coefficient is lower than the smooth cylinder in n=0.2 at all Reynolds number (10,20,30,40). The drag value is more in case of groove cylinder with respect to the smooth cylinder at low Re (10,20,30) in n=0.4,0.6,0.8,1. And when the Re value is 40, it shows effectiveness in n=0.2,0.4,0.6 but in n=0.8 and 1 the drag value again increase in smooth cylinder with respect to the groove cylinder.

Reynolds No.30			Reynolds No.40		
Smooth Cyl.	**Groove Cyl.**	**Percentage**	**Smooth Cyl.**	**Groove Cyl.**	**Percentage**
1.369	1.355	-1.088	1.156	1.137	-1.679
1.450	1.450	0.000	1.240	1.236	-0.286
1.549	1.549	0.001	1.343	1.343	-0.020
1.634	1.635	0.065	1.436	1.436	0.022
1.703	1.705	0.144	1.513	1.515	0.082

Wake Length-

For shear thinning fluids, wake length is increasing at the groove cylinder but for Newtonian fluid, wake length is increasing at the smooth cylinder with respect to the groove cylinder.

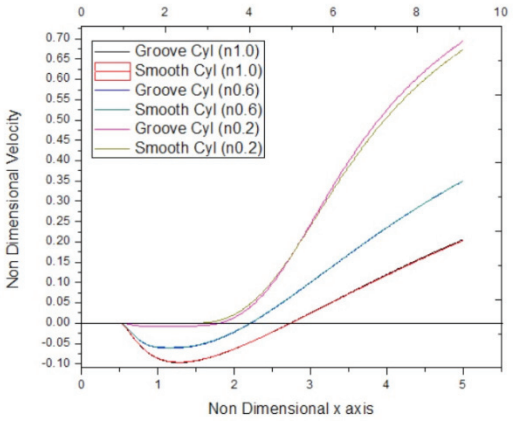

Figure 4: Variations of Wake length at Re 40 with the n values 0.2,0.6,1

Conclusion

The steady laminar flow of non-Newtonian shear thinning fluids across the groove cylinder and smooth cylinder are studied at the Reynolds Number 10,20,30 and 40. In the present study, the total Drag coefficients are more significant at the lower value on n (Shear Thinning fluid). And the Wake or Recirculation length shows a small effectiveness at lower Renolds number. And as Reynolds number increases the wake length value also be increased linearly for both Smooth and Groove cylinder.

REFERENCES

1. B Sharma, G Verma, R. N. Burman, "Steady flow of power-law fluids past a slotted circular cylinder at low Reynolds number", Physics of Fluids 34, 093615 (2022). https://doi.org/10.1063/5.0102861.
2. A. Priyadarshan, M.S. Afzal, "Numerical investigation of flow past a circular cylinder modified with a single groove at low Reynolds number", Physics of Fluids 35, 027125 (2023).https://doi.org/10.1063/5.0137530.
3. S.C.R. Dennis, W. Qiang, "Viscous flow normal to a flat plate at moderate Reynolds numbers", J. Fluid Mech. (1993), vol. 248, pp. 605635. https://doi.org/10.1017/S002211209300093X.
4. Yahaya, S. Samion, F.M. Zawawi, "The Evaluation of Drag and Lift Force of Groove Cylinder in Wind Tunnel", Journal of Advanced Research in Fluid Mechanics and Thermal Sciences 68, Issue 2 (2020) 41-50. https://doi.org/10.37934/arfmts.68.2.4150

20

Synthesis Testing Charecterstics with Performance Analysis of Long Durability Light Weight Ionic Liquid Aluminium Battery.

Ashishkumar R. Kale , Deepshikha Datta , Dr. Bimal Das

Introduction:

Ionic liquid are compounds that have revolutionized research centres and chemical industries in recent year.[1] These compound are part of green chemicals like solvents, have a very important role in reducing the use of hazardous toxic and environmentally harmful.[2]

Particularly lithium ion batteries have attracted considerable attention and dominated the commercial market and academic research in various battery system in terms of high energy density, high operating voltage and superior cycle stability. [3] However the lithium sources are less that limit their market. In addition the safety issues caused by thermal runway also limit their application. [4]

Fortunately, several new advanced battery chemistries and concepts (not depends on lithium) have emerged in recent years, which opens up new avenue for research. These chemicals comes from verities of different elements

(aluminium, magnesium and sodium) and these materials can be classed as metal-ion battery concepts. [5]

Electrolyte are ubiquitous and indispensable in rechargeable batteries. [6] In all cases an important challenge is to develop electrolyte with good electrochemical properties, contribute to reduce battery aging, enhance battery safety and allow the system to be charged and discharged electrochemically. [7] Some work are their such as to devote to prepare electrolyte which have high ionic transport ability, excellent chemical/ electrochemical stability, non flammability, low viscosity and economic cost. [8]

In this review, a general description of ionic liquids and historical background are given; the structure of ionic liquids, cation, anions types and synthesis method in this related literature are summarized. The main application areas and basic applications are also discussed hear in detail.

Batteries history to present:

Batteries provide the primary source of electricity before the development of the electric grid around the end of 19th century. One important classification for batteries is by their life cycle. "Primary" batteries can produce current as soon as assembled but once the active element consumed they cannot electrically recharged.

The development of lead acid battery and subsequent "secondary" or "chargeable" types allowed energy to be restored to the cell, extending the life of permanently assembled cells. The introduction of nickel and lithium based batteries in later half of the 20th century made the development of innumerable portable electronic devices.

Plante's first model consisted of two lead sheet separated by rubber strips and rolled into a spiral. [9] His batteries were first used to power the light in train carriages.

In 1866 Georges Leclanche invented a battery that consist of a zinc anode and a magnese dioxide cathode wrapped in a porous material dipped in the jar of ammonium chloride solution. It provided a voltage of 1.4 volts. [10] The dry cell form was used to power the early telephones.

In 1899 Waldemar Jungner invented the nickel-cadmium battery, a rechargeable battery that has nickel and cadmium electrode in a potassium hydroxide solution; the first battery to use an alkaline electrolyte.

Until the late 1950s, the zinc-carbon battery continue to be a popular primary cell battery but its relatively low battery life reduces sales.

The nickel-hydrogen battery entered the market as an energy storage subsystem for commercial communication satellite. The nickel-metal hydride batteries tend to have longer life spans than Nickel-cadmium batteries. Since cadmium is toxic, NiMH batteries are less damaging to the environment.

In 1970s the commercial lithium ion batteries came into market. Lithium is the metal with lowest density with greatest electrochemical potential and energy to weight ratio. The low atomic weight and small size of ions also speed its diffusion, suggesting that it would make an ideal material for batteries. [11]

In 1985 Japan build the first lithium ion battery prototype, a rechargeable and more stable version of lithium battery. Then in 1997, the lithium polymer battery was released by Sony. These batteries hold their electrolyte in a solid polymer composite instead of in liquid solvent and the electrode and separator are laminated to each other. It is use in mobile phone, radio controlled aircraft.

In 2015 researchers at Stanford University claimed to have developed an aluminium ion battery with recharge time about one minute. Their cell provide about 2V, 4V if connected in series of two cell. The prototype lasted over 7500 charge discharge cycle with no loss capacity. The battery was made of aluminium anode, liquid electrolyte, isolation foam and a graphite cathode. During charging process $AlCl_4^-$ ions intercalate among the graphene stacked layer. While discharging $AlCl_4^-$ ions rapidly deintercalate through the graphite. The cell display high durability, withstanding more than 10,000 cycles without a capacity decay. The cell was stable, nontoxic, bendable and non-flammable. [12]

Aluminium:

Aluminium has density lower than those of other common metals at approximately one third that of steel. It has stable isotope. [13] This isotope is very common, making aluminium the twelfth most common element in the universe.

The aluminium cation $Al^{3+}$is small and highly charged; as such, it is polarizing and bonds aluminium forms tend toward covelency. It is the third most abundant element after oxygen and silicon.

The production of aluminium starts with the extraction of bauxite rock from the ground. The bauxite is process and transformed using Bayer process

into alumina, which is then processed using Hall-Heroult process resulting in the final aluminium metal.

Aluminium ion battery:

The large-scale energy storage equipment gradually becoming research hotspot in the field of electrochemistry, rechargeable aluminium ion batteries have described as the most promising candidate to substitute for well-developed lithium ion batteries. The attention should be paid to two crucial factors impacting the electrochemical performance that is the positive electrode material and the electrolyte.

The ionic liquid analog formed through the mixture of urea and $AlCl_3$has previously shown to serve as a low cost electrolyte for an aluminium graphite battery while maintaining good performance and achieving high columbic efficiency.

The aluminium-ion battery based on chloroaluminate ionic liquid electrolyte, the interfacial reaction between cathode and electrolyte contains three processes:

1. The dissociation process of polyanion near the surface of the cathode.
2. The migration of dissociated polyanion from an electrolyte to the surface of the cathode.
3. The cathode accepts electrons to form an external circuit.

From this the rate determination step is studied and calculated the activation energy barrier. It also helps to understand the effect of dissociation process of polyanions on electrochemical kinetics.

Analysis of current and voltage

The oxide layer on aluminium surface however would be detrimental to the battery performance. It contributes to the fact that the reversible electrode potential is not achieved and that the activation of the electrode is delayed (a time lag before the cell reaches its maximum operating voltage). Some groups report on benefits of the oxide film, such as restriction of the growth of crystalline aluminium dendrites and strong corrosion, thus improving the cyclic stability of an aluminium battery.

It is found that addition of small amount of Zn, Cd, Mg or Ba to the negative electrode potential by (0.1-0.3V) Fan et al. (2015) investigated the electrode properties and battery performance of polycrystalline Al, Al (001). The study revealed that Al (001) single crystals displayed lower corrosion rate and higher capacity density due to the low surface energy.

The current collector can be fabricated by coating Tin on stainless steel or flexible polyimide subtract by low cost, rapid, scalable method such as magnetron sputtering. When these current collector are used stable cathodic operation is observed at voltage of up to 2.5V (Al^{3+}/Al). These batteries have high columbic efficiency of 99.5%, a cyclability of at least 500 cycles.

Energy per kg of aluminium fuel cell is about 7-8 times more in the same 1.5-2 tonnes, aluminium fuel cells can promise a range of about 500-600 Km in 1.5-2 tonnes of battery cells. Furthermore aluminium plate's replacement would take minutes compared to hours of charging time of lithium ion batteries.

Energy density is about 45 to 91 Kg. Life cycle is 250,000 times. Efficiency is 90-99.5%. Then discharging C-rate is about 10-4000. Safety is high. Operating temperature is 20-150^{o}C.

Summary:

Most of the studies are dealing with aluminium chloride graphite batteries instead of aluminium-ion batteries, since $AlCl_4^-$ instead of Al^{3+} is a mobile species. In order to solve the challenges two major problem to overcome the good electrolyte and positive electrode. The limits concerning interface and diffusivities, however might be overcome with an entirely new manufacturing route making use of thin film technologies already existing in semiconductors industry. Hence suitable working solid aluminium-ion conductor should push the development of rechargeable aluminium-ion batteries. At the same time they would build thin film batteries with extraordinary energy densities, applicable for the on chip power supply of sensors and mobile applications.

The aluminium-ion battery is a highly promising battery technology concepts. If progress achieved in reversible aluminium stripping and deposition as well as in identifying suitable solid electrolyte and positive electrode, this battery may open a huge application range.

REFERENCES:

[1] Welton, T. Room-temperature ionic liquids: Solvents for synthesis and catalysis. Chem. Rev. 1999,99, 2071-2084.

[8] Brennecke, J. F.; Maginn, E. J. Ionic liquids: Innovative uids for chemical processing. AIChE J.2001,47, 2384-2388

[8] Brennecke, J. F.; Maginn, E. J. Ionic liquids: Innovative uids for chemical processing. AIChE J.2001,47, 2384-2388

[2] Brennecke, J. F.; Maginn, E. J. Ionic liquids: Innovative fluids for chemical processing. AIChE J. 2001, 47, 2384-2388.

[3] J. Tarascon and M. Armand, "Issues and challenges facing rechargeable lithium batteries," Nature, vol. 414, no. 6861, pp. 359–367, 2001.View at: Google Scholar

[4] F. Wu, H. Yang, Y. Bai, and C. Wu, "Paving the path toward reliable cathode materials for aluminum-ion batteries," Advanced Materials, vol. 31, no. 16, p. 1806510, 2019. View at: Google Scholar

[5] G. A. Giffin, "Ionic liquid-based electrolytes for "beyond lithium" battery technologies," Journal of Materials Chemistry A, vol. 4, no. 35, pp. 13378–13389, 2016.View at: Google Scholar

[6] K. Xu, "Nonaqueous liquid electrolytes for lithium-based rechargeable batteries," Chemical Reviews, vol. 104, no. 10, pp. 4303–4418, 2004.View at: Publisher Site | Google Scholar

[7] Q. Yang, Z. Zhang, X. G. Sun, Y. S. Hu, H. Xing, and S. Dai, "Ionic liquids and derived materials for lithium and sodium batteries," Chemical Society Reviews, vol. 47, no. 6, pp. 2020–2064, 2018.View at: Google Scholar

[8] V. Etacheri, R. Marom, R. Elazari, G. Salitra, and D. Aurbach, "Challenges in the development of advanced Li-ion batteries: a review," Energy & Environmental Science, vol. 4, no. 9, pp. 3243–3262, 2011.View at: Google Scholar

[9] "Gaston Planté (1834-1889)". Corrosion Doctors. Retrieved 2012-08-29.

[10] "Leclanché Cell". Battery Facts. Retrieved 2007-01-09.

[11] Winter, Martin; Barnett, Brian; Xu, Kang (30 November 2018). "Before Li Ion Batteries". Chemical Reviews. 118 (23): 11433–11456. doi:10.1021/acs.chemrev.8b00422. PMID 30500179. S2CID 54615265.

[12] "Ultrafast Rechargeable Aluminum-ion Battery". Industrial Technology Research Institute. Archived from the original on 15 November 2018. Retrieved 2 March 2018.

[13] "Aluminium". The Commission on Isotopic Abundances and Atomic Weights. Archived from the original on 23 September 2020. Retrieved 20 October 2020.

21

Thermodynamic Analysis of Waste Heat Powered Absorption Cooling System

Nitesh Kumar Choudhary, Sujit Karmakar

Abstract

Thisstudy presents a thermodynamic analysis of the absorption cooling system (ACS) with a cooling capacity of 105kW. The ACS is powered by waste heat available at the flue gas exhaust of a pressurized pulverized combined cycle power plant. The use of waste heat for cooling purposes offers a sustainable and efficient solution, reducing both energy consumption and environmental impact. The working fluid used in the ACS is a binary mixture comprised of ammonia and water, and with the use of cycle tempo software, the modelling and simulation part has been done. Energy analyses was performed to assess the ACS's thermodynamic performance. The thermodynamic analysis reveals that the ACS has a coefficient of performance (COP) of 0.595. In addition, varying the temperatures of the generator, absorber, condenser, and evaporator affects the COP of the ACS.

Keywords: Ammonia-water, cooling system, COP, Waste heat utilization

Introduction

The demand for cooling and air conditioning systems rising globally due to population growth and modernization. Earlier, these cooling and air

conditioning demands were fulfilled through conventional techniques. However, conventional cooling technologies heavily reliant on electricity consumption contribute to high energy demands and associated greenhouse gas emissions. These cooling systems use about 15% of the total electricity produced worldwide, according to the International Institute of Refrigeration [1]. It is anticipated that there will be an increase in conjunction with the projected global summer temperature rise of 2-4°C by the end of this century [2]. To address these challenges, there is a growing interest in sustainable and energy-efficient cooling systems. One such technology that holds promise is the absorption cooling system, which utilizes waste heat, solar energy etc., to provide cooling. India is a vast country with enormous and increasing electricity demand. In this scenario, the cooling system electricity demand creates an additional burden which can often be fulfilled by the waste heat utilization through the absorption cooling system (ACS).

This study presents a thermodynamic analysis of ACS and an innovative approach to harnessing the waste heat generated by a coal-based power plant for powering an ACS in order to achieve sustainable and efficient cooling solutions. The proposed system utilizes the waste heat from the power plant, which would otherwise be dissipated into the environment, to drive an ACS.

Materials and Methods

The proposed system is modelled and simulated using the Cycle Tempo software [3], a robust application developed by the Delft University of Technology, used for analyzing and optimizing thermodynamic cycles.

A. ACS Configuration

Figure 1 depicts a single-stage ammonia-water ACS, run by the power plant's waste heat, wherein water serves as the absorbent and ammonia as the refrigerant. The main components of the ACS include the evaporator, absorber, condenser, and generator, with auxiliary elements such as the separator, throttle valves, HE, and pump. The system utilized the waste heat at the generator to heat the rich ammonia solution, causing ammonia to evaporate and leaving behind a hot weak solution.

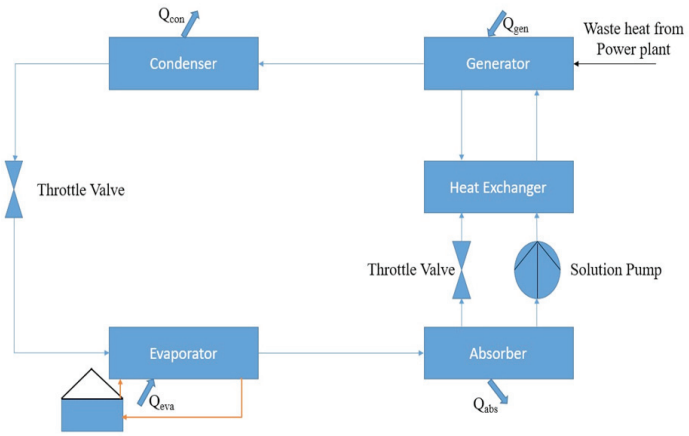

Figure-1: Absorption Cooling system.

B. Working Fluid Characteristics

In ACS, the working fluid typically consists of two main components: the refrigerant (in this case, ammonia) and the absorbent (water solution). The cooling process involves the refrigerant (ammonia) absorption into the absorbent (water) at low temperature and pressure and then releasing the refrigerant at high temperature and pressure to create a cooling effect.

C. Thermodynamic Modelling

The COP of the system is the ratio of heat transfer through the evaporator to the sum of heat transfer through the generator and the work done through thepump. The pump work (W_p) required in the absorption system is very small that can be neglected [4].

$$COP = \frac{\dot{Q}_{ev}}{\dot{Q}_{ge} + \dot{W}_p}$$

$\dot{Q}$ Represent the heat transfer rate, of evaporator (ev) and generator (ge).

Assumptions

1. The ambient conditions are set at 1.013 bar pressure and 25°C temperature.

2. Waste heat is harnessed from the flue gas exhaust of a 400 MW_e PPCC plant [5].
3. A 105kW of ACS system is considered for analysis.
4. The selected working fluid is a mixture of ammonia-water.
5. There are no pressure loss and heat leakage in the system except for the main components of ACS.

Results and Discussion

This section explains the findings and outcomes of the simulation analysis on ACS run by flue gas waste heat. It provides a comprehensive analysis of the system's performance, including cooling capacity, coefficient of performance (COP).

Thermodynamic Result

The thermodynamic performance of an absorption cooling system at different stages with a generator temperature of 80.45°C, Condenser temperature of 30°C, absorber temperature of 3°C, evaporator temperature of 12.19°C and cooling capacity of 105kW. It is evident that the system efficiently absorbs and releases heat at specific points, resulting in a cooling effect.

Table 1: Thermodynamic results of ACS

Heat input in Generator	176.04 kW
Heat transfer through Condenser	146.057
Cooling capacity in Evaporator	105 kW
Heat Transfer through Absorber	135.323 kW
Heat transfer through Solution HE	44.0765 kW
Work input in Pump	0.36 kW
COP	0.595

Table 1 shows the energy in and out through each component of the ACS. The table presents the thermodynamic results of an ACS. The system's generator requires a heat input of 176.04 kW to drive the absorption process, while the condenser transfers 146.057 kW of heat to the environment during the cooling cycle. The evaporator provides a cooling capacity of 105 kW, absorbing heat from the space being cooled. The absorber facilitates heat transfer of 135.323 kW during the absorption process, and the Solution Heat Exchanger (HE)

transfers 44.0765 kW of heat. The work input in the pump, responsible for circulating the absorbent, is relatively low at 0.36 kW. The Coefficient of Performance (COP) of the system is calculated to be 0.595, which represents the cooling output per unit of energy input.

Conclusions

The aim of this study is to harness the available waste heat from the flue gas exhaust of the plant. This research integrates an absorption cooling system with the pressurized pulverized combined cycle power plant to effectively utilize this waste heat and assess its thermodynamic performance. By incorporating the absorption cooling system, the power plant optimizes its energy utilization, leading to a reduction in its environmental impact. This strategy lessened the plant's dependence on supplementary electricity sources for cooling, resulting in improved energy efficiency and decreased carbon emissions. The thermodynamic analysis of the ACS indicates a coefficient of performance (COP) of 0.595. Moreover, variations in the generator, absorber, condenser, and evaporator temperatures affect the COP of the ACS. The analysis reveals that a slight increase in the COP of the system occurs with higher generator and evaporator temperatures, while raising the condenser and absorber temperature results in a COP decrease. In conclusion, integrating an ACS run by the power plant's waste heat provides a promising solution for sustainable cooling requirements.

- Future Work
- Exergy Analysis.
- Environmental Analysis.

Sensitivity analysis of COP, Reversible COP and Exergetic Efficiency to check the variability of the present cycle.

REFERENCES

1. Kalkan, N., Young, E.A. and Celiktas, A., Solar thermal air conditioning technology reducing the footprint of solar thermal air conditioning. Renewable and sustainable energy reviews, 2012, 16(8), pp.6352-6383.
2. IPCC, Intergovernmental Panel on Climate Change, 2022. IPCC Fourth Assessment Report: Climate Change.
3. Delft University of Technology (2007) Cycle Tempo Release 5.0 [online] http:// www.asimptote.nl/ software/cycle-tempo/cycle-tempo-details.

4. Shahata, A.I., Aboelazm, M.M. and Elsafty, A.F., Energy and exergy analysis for single and parallel flow double effect water-lithium bromide vapor absorption systems. International Journal of Science and Technology, 2012, 2(2), pp.85-94.
5. Kalimuthu, S., Karmakar, S. and Kolar, A.K., 2017. 3-E analysis of a Pressurized Pulverized Combined Cycle (PPCC) power plant using high ash Indian coal. Energy, 2017, 128, pp.634-648.

22

Thermodynamic analysis of a 500MWe Integrated Co-Gasification Hybrid Power Plant

Dinesh Singh, Nitesh Kumar Choudhary, Sujit Karmakar[3]

Abstract

Integrated Gasification Hybrid Power Cycle (IGHPC) is such a technology in which higher efficiencies can be achieved. The use of renewable energy sources, either sole or by blending with conventional energy sources, can minimize the emission of Carbon dioxide (CO_2). Rice husk, an energy-dense biomass, is abundant in India. A thermodynamic analysis based on energy analysis of a 500MWe Hybrid Power Cycle (HPC) and IGHPC power plant using coal and a mixture of coal and rice husk in different percentages is carried out by using a flow sheet computer program "Cycle Tempo". There is a gain of 2.423% point energy efficiency for IGHPC power plant in comparison with HPC power plant using Indian coal. Moreover, the use of rice husk (25%) blended with coal increases the plant energy efficiency by 2.788 % point in comparison with HPC.

Keywords: Integrated Gasification Hybrid Power Cycle, Co-gasification,Indian coal, Rice husk

Introduction

Population growth and industrialization have resulted in a significant demand for electricity. The primary source of energy has been fossil fuel power plants. Coal is used to generate electricity in the majority of countries throughout the world; After Australia, Russia, China, and the United States, India ranks fifth in terms of coal reserves. Coal-fired power plants provide around 61 percent of India's overall energy needs. The majority of power facilities burn coal in pulverized form [1]. The ash level of Indian coal is considerable, ranging between 35 and 55 percent by mass. In pulverized coal boilers, such coals produce a lot of fly ash and slag. As a result, there is a growing need to switch to more efficient and cleaner coal-fired power-producing systems.Gasification is one of these approaches, as it creates cleaner synthetic gas which can be charged in hybrid gas and steam power plants. As a result, the Integrated Gasification Hybrid Power Cycle (IGHPC) is seen as a better option than traditional power-producing systems in terms of reducing solid and gaseous emissions.Although coal gasification is a well-known technology, relatively little is known about the co-gasification of coal and biomass. The production of heat and electricity can now be accomplished by the co-gasification of biomass and coal. Following coal, oil, and natural gas as the most common energy sources, biomass accounts for more than 10% of global energy consumption. And it is estimated that By the year 2050, biomass and bio-waste are expected to avail one-third of the world primary energy needs [2]. Akanksha Mishra et al. has done an experiment on the effect of operating parameters on coal gasification and the results reveal that as the gasification temperature rises, so does carbon conversion and gasification rate [3].The 3-E analysis for a PPCC power plant using high ash Indian coal was carried out by Selvam Kalimuthu et al. They found that the plant energy efficiency of PPCC SubC and SupC plants using HA coal is 42.44 percent and 43.46 percent, respectively. Exergy efficiency for the same plant utilising HA coal is 38.94 percent and 39.87 percent, respectively [4].

In this present study, a 500 MWe Supercritical IGHPC power plant has been investigated by varying the percentages of rice husk blending with high ash Indian coal as fuel input, as well as changing excess air ratio in the combustor and then the thermodynamic performance of the IGHPC thermal power plant in terms of efficiencies are numerically analyzed.

Materials and Methods

A. Plant Configurations

Figure 1 depicts a 500 MWe IGHPC power plant with Super Critical steam characteristics of 250 bar/600°C with an economizing temperature of 359.63°C. A gasifier is currently integrated with the steam power plant in this arrangement. The syngas (primarily CO and H_2) is created when coal is combusted in the presence of less air and steam in the gasifier, and it is then combusted in the combustor with 57 percent surplus air for Indian coal and 51percent excess air for Indian coal blended with rice husk (25%). The flue gas pressure and temperature at the gas turbine's inlet are 15.5 bar &1595.52°C for coal and 15.5 bar & 1597.61°C for coal & rice husk mixture.

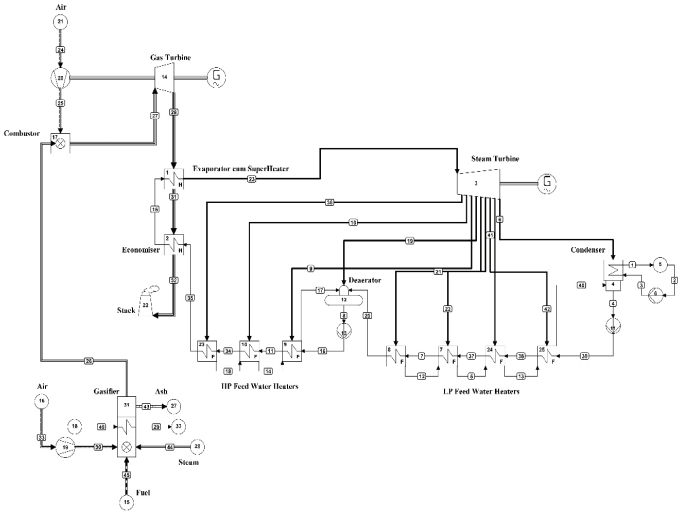

Figure-1: Layout ofIGHPC Plant

Methodology

Cycle Tempo, commercially available simulation software, is used to conduct thermodynamic analysis of the suggested model [5]. A power plant consists of several circuits, and each circuit has several components. These components are further connected with each other by pipes carrying different media like water, steam, air, fuel, flue gas, etc.

Performance Parameters

The power plant performance can be measured in terms of plant energy efficiency:

Energy efficiency (η), $\eta = \frac{\text{Net Power Output}}{\dot{m} \text{ of coal X HHV of coal}} \eta = \frac{\text{Net Power Output}}{\dot{m} \text{ of coal X HHV of coal}}$

D. Assumptions

1. A 500 MWe supercritical power plant is considered for the study.
2. The temperature of the bottom ash is 1050°C.
3. Turbines, compressors, and pumps have isentropic efficiency of 85 percent, 85 percent, and 80 percent,respectively.
4. Generator efficiency is considered as 0.987.
5. The pressure in the gasifier is 16 bar, and the reaction temperature is 800 °C.
6. 57% excess air in combustor for Indian coal and 51% excess air for Indian coal blended with 25% rice husk in case of IGHPC.

Results and Discussion

The comparison of plant efficiencies for HPC using Indian coal, IGHPC using Indian coal and IGHPC using Indian coal blended with rice husk (25%) are shown in Table 2. It can be clearly seen from Table 2 that there is about 2.423 % point increase in the plant energy efficiency for IGHPCusing Indian coal as compared to HPC using Indian coal. In addition, in the case of rice husk (25%) mixture with coal in IGHPCthere is about 2.788 % point increase in the plant energy efficiency as compared to HPC using Indian coal.

Table 2: Comparison of plant efficiencies

Different Power Plant	Energy efficiency (%)
Supc-HPC using Indian Coal	49.108
Supc-IGHPCusing Indian Coal	51.531
Supc-IGHPCusing Indian Coal blended with 25% Rice husk	51.896

Conclusions

The energy efficiency of IGHPC plant using Indian coal and Indian coal blended with 25% rice husk are 51.531%, 51.896% respectively. IGHPC using Indian coal has a 2.423 percent increase in plant energy efficiency compared to HPC using Indian coal. When rice husk (25%) is mixed with coal in an IGHPC, the plant energy efficiency increase by around 2.788 percent point, when compared to HPC using Indian coal. When utilizing Indian coal combined with 25% rice husk, increasing the amount of surplus air in the combustor from 40% to 80% lowers energy efficiency by 1.192 percent in the IGHPC plant.

1. *Future Work*
2. Exergy Analysis.
3. Environmental Analysis.
4. Sensitivity analysis with different parameters.

REFERENCES

1. Barnes, D.I., Understanding pulverized coal, biomass and waste combustion–a brief overview. Applied Thermal Engineering, 2015, 74, pp.89-95.
2. Farzad, S., Mandegari, M.A. and Görgens, J.F., A critical review on biomass gasification, co-gasification, and their environmental assessments. Biofuel Research Journal, 2016, 3(4), pp.483-495.
3. Mishra, A., Gautam, S. and Sharma, T., Effect of operating parameters on coal gasification. International Journal of Coal Science & Technology, 2018, 5(2), pp.113-125.
4. Kalimuthu, S., Karmakar, S. and Kolar, A.K., 3-E analysis of a Pressurized Pulverized Combined Cycle (PPCC) power plant using high ash Indian coal. Energy, 2017, 128, pp.634-648.
5. Cycle–Tempo Release 5.0.: Delft University of Technology. Available online: http://www.tudelft.nl, 2008.

23

Techno-Economic Optimization of HRES; A Trajectory Towards Sustainable Development

Nagendra Kumar, Askand Kumar, Sujit Karmakar

Abstract

Although India ranks third globally in energy generation, still 35% of Indian rural areas are struggling for electricity access due to lack of grid infrastructure or high energy costs. In this scenario the present study aims design, develop and optimize a polygeneration based solid waste assisted HRES that can cater electricity, heat and compost with minimal economy and higher reliability. Furthermore, the sensitivity analysis due capacity shortage is performed. The result shows that the proposed model is optimal at a capacity shortage of 1% with affordable cost of energy Rs. 3.92/kWh and net present cost of Rs. 1.75 million. Furthermore, the electricity, heat and compost generation from the optimal HRES is 108 kWh/day, 27.06 kWh/day and 360 kg/day respectively. Moreover, the proposed study indicates a trajectory towards sustainable development goal, 7 and 13 through polygeneration through HRES at an affordable cost.

Keywords: HRES, Distributed Generation, Polygeneration, Energy Economics, Waste-to-Energy.

Introduction

The Indian government is promoting the use of renewable energy sources, citing the environmental impact of conventional fuels and the global focus on emission reduction, in line with Sustainable Development Goal 7 and 2030 agenda [1]. While evaluating renewable energy capacity in India is estimated to be around 100,000 MW; however, a significant portion of this potential remains unexplored [2]. Over 35% of rural India's rural areas lack electricity access due to geographical, terrain, and environmental factors.

A viable alternative to these systems is the integration of several renewable energy resources to create a hybrid renewable energy system (HRES) [3]. Furthermore, the inclusion of solid waste to energy facilities within these systems can be considered as an additional contribution to the utilisation of renewable energy resources. The treatment of this solid waste can involve the processes of anaerobic digestion and gasification in order to generate biogas [4]. According to a study, the combustion of one metric tonne of biodegradable trash has the potential to produce around 550 kilowatt-hours (kWh) of power [5]. Apart from solar and wind there are many other HRES have been design, developed and implemented such as solar PV-wind assisted bio-generator HRES for Rural electrification [6]. Design and techno-economic optimization of solar-biogas based HRES for electrification of island [7]. Optimization of a trigeneration system for its economics in Indian scenario [8].

Several studies on renewable energy systems focusing on technical feasibility, economic viability, reliability, and electrification is performed [9]. However, there is a lack of focus on the techno-economics of Hybrid Renewable Energy Systems (HRES), considering solid waste disposal and polygeneration. This study examines energy shortages, and performs sensitivity analysis, for HRES performance and its economy.

Materials and Methods

The techno-economics of the proposed model is done with the help of Hybrid Optimization of Multiple Energy Resources (HOMER) software. In order to fulfil the required energy, demandthe input are provided to HOMER as energy resource data, load data, size, and cost parameters of each component.

Studied Location and Consumption Load

For the optimization of HRES Sessa village in Arunachal Pradesh, India, located in the Bhalukpong circle is considered. The village has a population of 184 with 46 residential houses. Agriculture and tourism is the main activity of locality for their survival. The village is covered with hills and forest which makes the area rich in renewable energy resource. Although the access to electricity in this area is absent due to unavailability of the central grid. Furthermore, the electrification of the selected area through grid extension is also costlier due to its geography. The consumption load demand is estimated to be 95 kWh/day with 13.95 kW peak for electricity and for heat the consumption demand is 30 kWh/day with 6.13 kW peak.

Resource Assessment

The community of Sessa village is fortunate to have access to abundant biomass (due to rice cultivation twice in a year) and a favourable solar resource. The surface receives an estimated annual average of 4.45 kWh/m^2 of solar radiation, with around 250 days of clear sun and an annual average clearness index (CI) of 0.51. Furthermore, the annual average wind speed is 2.44 m/s and daily temperature of 15.63°C at studied location.

Proposed Model

The resource assessment shows that the studied location has favourable and efficient energy generation scenario through the utilization of solar PV, and a bio-gas generator. Furthermore, a thermal load controller is employed to convert the excess electricity generated through the system and a storage device is integrated for the backup purpose. Fig.1 shows the schematic of the proposed HRES.

Results and Discussion

Homer provides the optimum result for the size of the HRES components and its economics based on the renewable energy and other economic data which are considered as inflation rate 2%, nominal discount rate 8%, real discount rate 5.88% and project lifespan is 25 years.

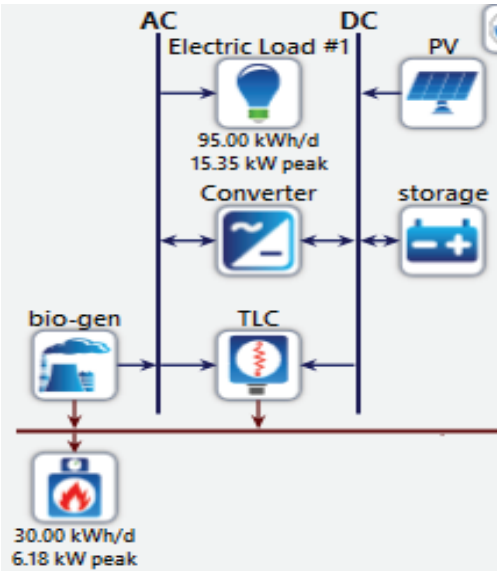

Figure-1: Schematic of the proposed model

Optimization of Proposed HRES

The optimization results show that the optimal system will have distinguished optimal system corresponding to each capacity shortage. The result of optimization of present study is shown below in Table 1.

Table 1: Optimization of proposed HRES with Various capacity shortage

	HRES-A	**HRES-B**	**HRES-C**	**HRES-D**	**HRES-E**	**HRES-F**
Capacity Shortage (%)	0	1	2	3	4	5
PV (kW)	14	14	14	13	13	12
Bio-Gen (kW)	5	5	5	5	5	5
Storage (kVA)	88	44	32	28	23	21
TLC (kW)	10	10	10	10	10	10
Converter (kW)	8.83	8.92	8.93	5.54	7.33	7.37
NPC (Rs.Million)	2.61	1.75	1.56	1.50	1.43	1.38
COE (Rs./kWh)	5.80	3.92	3.49	3.36	3.23	3.12

From the above table it is clear that out of all the model the HRES-B with CS 2% is found to be most optimal and have increased energy generation and the economics of the system is lowest with NPC of Rs. 1.75 million and COE

of Rs. 3.92/kWh due to the decreased capacity of storage requirement.

Performance Analysis of Optimal HRES- B

Electricity Generation

The electricity consumption demand from the community is 95 kWh/day with a peak load demand of 13.95 kW. Whereas, the optimal HRES generates an annual average of 39553 kWh/year (108.36 kWh/day) of electricity. This results in the surplus electricity generation of 3894kWh/year. Out of total electricity generated from the HRES the share of PV is 50.3% and bio-gen is 49.7%.

Heat Generation

The heat consumption demand from the community is 30 kWh/day with a peak load demand of 6.18 kW. Whereas, the optimal HRES generates an annual average of 9861 kWh/year (27.016 kWh/day) of heat. This results in the lack of heat generation of 3 kWh/day.

Compost production

The propose HRES utilizes the digester to convert the biomass (including kitchen waste and agricultural waste) for the biogas generation. This results in compost generation of 360 kg/day as a by-product. Since the biomass available at the studied location is almost 0.8 tons/day.

Economic Analysis

Table 2: Economics of the HRES-2

Component	Capital Cost (Rs.)	Replacement cost (Rs.)	Operating cost (Rs.)	Salvage cost (Rs.)	Total cost (Rs.)
PV	427,000	0.00	1,809	0	428,809
Bio-gen	11,041	50,784	360,354	-1870	420,309
Converter	31,215	13,244	0.00	-2492	41,967
Storage	528,000	310,970	56,881	-42162	853,688
TLC	6,000	1,912	0.00	-1078	6,834
System	1,003,257	376,911	419,045	-47,603	1,751,607

The economic analysis of the optimal HRES shows that, the optimal

system has lowest economy due to reduction in storage need. This results in low operating and replacement cost. Hence, the optimal HRES holds net present cost of Rs. 1.75 million and cost of energy Rs. 3.92/kWh. Table.2 shows the economics of the optimal HRES.

Conclusions

The escalating cost of fossil fuels with the growing energy demand have attracted the global concern towards renewable energy sources. India ranks third globally in energy generation, but 35% of rural areas are still struggling for electricity access due to lack of grid infrastructure or high energy costs. This study explores a solid waste-based hybrid renewable energy system. The optimal HRES generates 108.36 kWh/day of electricity, 27.06 kWh/day of heat and 360 kg/day of compost and holds minimal economy as NPC is Rs.1.75 and COE is Rs.3.92/kWh. Furthermore, the simple payback period of optimal system is 4.8 years.

REFERENCES

1. Ministry of New and Renewable Energy.
2. https://mnre.gov.in/img/documents/uploads/file_f-1680367776122.pdf
3. Murugaperumal K, Raj PA. Feasibility design and techno-economic analysis of hybrid renewable energy system for rural electrification. Solar Energy. 2019 Aug 1; 188:1068-83.
4. Karaca AE, Dincer I, Nitefor M. A unique biomass based integrated energy system for cleaner production of multiple energy outputs for sustainable communities. Sustainable Cities and Society. 2023 Feb 1; 89:104330.
5. Chukwuma EC. Facility location allocation modelling for bio-energy system in Anambra State of Nigeria: Integration of GIS and location model. Renewable Energy. 2019 Oct 1; 141:460-7.
6. Brunner, P.H. and Rechberger, H., 2015. Waste to energy–key element for sustainable waste management. Waste management, 37, pp.3-12.
7. Tabasová, A., Kropá, J., Kermes, V., Nemet, A. and Stehlík, P., 2012. Waste-to-energy technologies: Impact on environment. Energy, 44(1), pp.146-155.
8. Kumar, A. and Samadder, S.R., 2017. A review on technological options of waste to energy for effective management of municipal solid waste. Waste Management, 69, pp.407-422.

9. Kumar N, Jana K, Karmakar S. A comparative study of solid waste based distributed multigeneration system between two Indian islands. J Indian Chem Soc. 2020 Oct;97(10b):1949.
10. Murugaperumal K, Srinivasn S, Prasad GS. Optimum design of hybrid renewable energy system through load forecasting and different operating strategies for rural electrification. Sustainable Energy Technologies and Assessments. 2020 Feb 1; 37:100613.

24

Flow Analysis around a Circular Cylinder with Trapezoidal Groove Modification

Chandan Kumar Bharti, Geeta Verma, Rabindra Nath Barman

Abstract

A numerical investigation on a circular cylinder having a trapezoidal groove (a passive control technique) at 90^0 has been studied. The aim of this study was to reduce the total drag coefficient developed by the flowing fluid at low Re (Re= 10, 20, 30, and 40). It has been observed that the coefficient of pressure (C_p) is increased at the rear end of the cylinder, which eventually increases the flow separation angle. The recirculation length is decreased by almost 25.71%. The vortex formation length is decreased. Affecting all these parameters it has been concluded that the total drag coefficient is reduced with a minimum percentage reduction of 0.45% at Re=10 and a maximum percentage reduction of 0.62% at Re=40.

Keywords: Passive control technique, Trapezoidal groove,Wake formation,Vorticity and Drag

Introduction

The flow of fluid around a circular cylinder [2-3] is a classical problem in fluid mechanics. Due to the widespread use of bluff bodies particularly circular cylinders, It is a topic of high interest for the researchers. The behavior of the

flow around a circular cylinder is influenced by various parameters such as cylinder diameter, flow velocity, Reynolds number etc. Although by observing the vorticity generated, the wake length, coefficient of pressure, and coefficient of drag generated by fluid as it passes the body, flow behavior can be examined. Sen et al.[3] Performed a steady 2d laminar flow around a stationary circular cylinder with a Re range of 6 to 40 of blockage ratio of 0.005. There is a different way to control drag produced one is the active control technique and another is the passive control technique [1, 4-6]. Active control techniques involve external energy input and real-time adjustments to manipulate fluid flow, While passive control techniques rely on fixed design features or material properties to control flow control. Here in this study passive control technique is used to describe flow behavior.Priyadarsan et al.[1] work on passive control technique using a circular cylinder with the modified groove of square, V-shape, and u-shape. It concluded that 90^0square-shaped groove gives better results. Very few work has been performed on trapezoidal groove shapes. This study is to examine the drag force acting on the circular cylinder having a trapezoidal groove at $90^{0.}$

Methodology

To investigate the present study a rectangular domain of 100Dx150D is used, Upstream length (L_u)=50D, Downstream length (L_d)=100D, A trapezoidal grooved cylinder of diameter D has been selected. The groove has a depth(d)=0.1D, r is the ratio of top length (Lt) to bottom length (L_b), r =2 is shown in Figure 1. The boundary condition used for the present study is uniform velocity at the inlet, outflow boundary condition at the outlet, No slip at both the bottom and top wall of the domain and no slip at the cylinder and groove. A finite volume-based simulation technique is used for mesh generation and calculation of the governing equations.Validation is done from Soares et al. for circular cylinders at Re 5 to 40 as shown in Table 1. The grid independence test is also performed.

Table-1: Validation result of circular cylinder [2]

Re	5	10	20	30	40
C_D(Present)	4.28	2.94	2.11	1.77	1.57
C_D (Soares et al)[2]	4.26	2.84	1.98	1.63	1.44

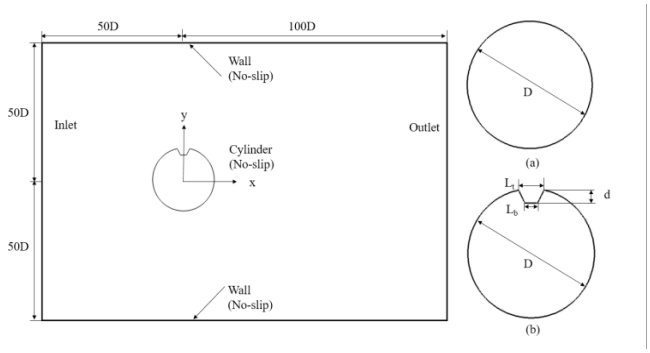

Figure-1: Schematic of domain.

Results and Discussion

Coefficient of Pressure (C_p)

Figure 2 shows variation of the coefficient of pressure at different location at the surface of cylinder. Here in this plot, it can be observed that at the front stagnation point, the vorticity of fluid is zero hence it gives maximum pressure here. As fluid moves towards the top point i.e. 90^0 from the front stagnation point C_p decreases, Again as it move behind the cylinder, the C_p increases indicating a recovery in pressure. By using passive control technique i.e. introducing a trapezoidal groove. It gives a higher value at the front stagnation pointand when it reaches to groove the pressure decreases below zero value. At the exit of groove pressure kinks and afterward it increases with same as in the smooth cylinder with a higher pressure coefficient which eventually increases the flow separation angle which result in decrease in drag.

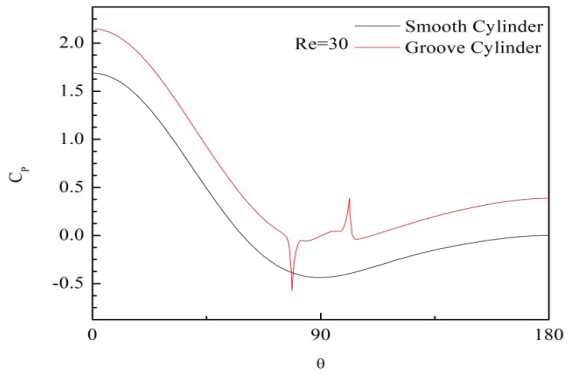

Figure 2: Coefficient of Pressure on the surface of the cylinder

RecirculationLength

Figure 3 shows the recirculation length. It has been observed from the study that by using the trapezoidal groove the recirculation length decreases by approximately 25.71%. which further illustrates that flow is reattached behind the cylinder at a distance less than in a smooth cylinder. It means the length of the wake generated is reduced which in result reduces the drag.

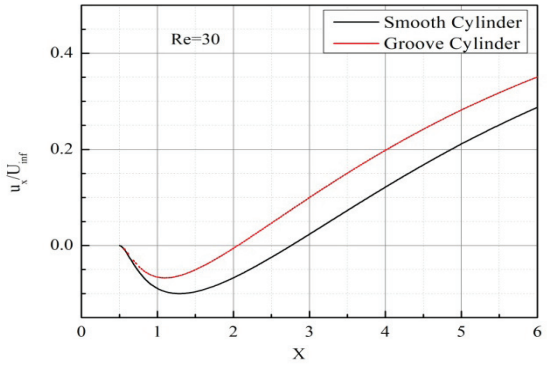

Figure-3: Recirculation length at Re=30

Vorticity

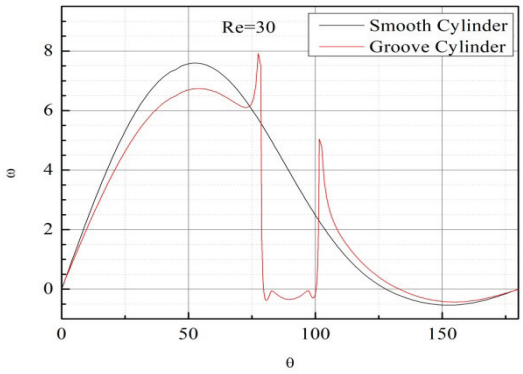

Figure-4: Vorticity on the surface of the cylinder

Vorticity is a fundamental parameter that describes the local rotation of fluid elements. Figure 4 shows the variation of vorticity along the surface of the cylinder. It is observed that at the front stagnation point to top of the cylinder vorticity is smaller for the grooved cylinder.Vorticity shows complex behaviour

in the groove, it increases then decreases rapidly at the entrance of the groove and at the exit respectively. vorticity is higher in the back side of cylinder than the smooth cylinder. Higher vorticity result in the shorter vortex formation length (Length of wake formed) which eventually reduces the drag. Further insights are when the vorticity plot crosses zero line (i.e. negative value), the separation starts. In this study it is also observed that flow separation angle is increased by introducing the trapezoidal groove in the cylinder.

Coefficient of Drag (C_D)

The Coefficient of drag (C_D) for flow past a circular cylinder is a key parameter that characterizes the resistance to motion caused by fluid flow. From Figure 5 (C_D v/s Re plot), It is observed that in Re range 10 to 40, the C_{Dv} values decreases from Re=10 to Re=40. The value of C_{Dv} in the grooved cylinder is less than the smooth cylinder. The C_{Dp} values also decrease from Re=10 to Re=40 but here the groove cylinder has higher value. When it comes to the overall C_D value decreases in grooved cylinder than in smooth cylinder by significant percentage. The decreased value at different Re in percentage terms is shown in Table 2.

Table-2: Percentage decrement in drag by modifying cylinder

Re	10	20	30	40
C_D(Smooth Cylinder)	2.9685	2.1118	1.7635	1.5626
C_D(Groove Cylinder)	2.9551	2.1010	1.7533	1.5529
percentage decrement	0.45	0.51	0.58	0.62

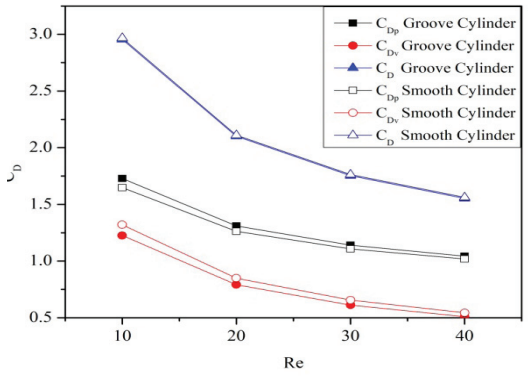

Figure-5: Pressure, viscous and total drag at different Re

Conclusions

This study investigates the reduction in drag coefficient using a passive control technique when flow passes a circular cylinder at different Re. The study includes a trapezoidal groove to reduce the drag. It is observed that the coefficient of pressure at the rear end of the cylinder has increased which increases the flow separation angle clockwise from the front stagnation point. Recirculation length decreases by 25.71%, which eventually formsa shorter wake. Vorticity is also investigated in this study and found that vortex formation length has been reduced which once again reduces the drag. The overall coefficient of drag(C_D) is investigated at Re = 10, 20, 30, and 40 and found that C_D value decreases by 0.42% at Re10, 0.51% at Re20, 0.58% at Re=30, and 0.62% at Re=40. It is concluded that as the Re value increases the percentage reduction in drag(C_D) decreases

REFERENCES

1. Priyadarsan, Ashutosh, and Mohammad Saud Afzal. "Numerical investigation of flow past a circular cylinder modified with a single groove at low Reynolds number." Physics of Fluids 35, no. 2 (2023).
2. Soares, A. A., J. M. Ferreira, and R. P. Chhabra. "Flow and forced convection heat transfer in crossflow of non-Newtonian fluids over a circular cylinder." Industrial & Engineering Chemistry Research 44, no. 15 (2005): 5815-5827.
3. Sen, Subhankar, Sanjay Mittal, and Gautam Biswas. "Flow past a square cylinder at low Reynolds numbers." International Journal for Numerical Methods in Fluids 67, no. 9 (2011): 1160-1174.
4. B. Sharma, G. Verma, and R. N. Barman, "Steady flow of power-law fluids past a slotted circular cylinder at low Reynolds number," Phys. Fluids, vol. 34, no. 9, 2022, doi: 10.1063/5.0102861.
5. B. Sharma and R. N. Barman, "Unsteady flow past slotted circular cylinders in laminar regime: Effect of slit shapes and Reynolds number," Phys. Fluids, vol. 35, no. 1, 2023, doi: 10.1063/5.0130736.
6. B. Sharma and R. N. Barman, "Steady laminar flow past a slotted circular cylinder," Phys. Fluids, vol. 32, no. 7, 2020, doi: 10.1063/5.0007958

25

Comparative Thermodynamic Analysis of Oxy-Coal and Air-Coal Combustion based 500 MWe Supercritical Steam Power Plants with Solar Aided Feed Water Heating

S.J. Chatterjee and S. Karmakar

Abstract

This paper proposes a comparative performance study of Oxy-Coal Combustion (OCC) and Air-Coal Combustion (ACC) based (both having solar assisted feed water heating(SAFWH) 500MW Supercritical (SupC) power plant with CO_2 capture system at fixed furnace temperature. The proposed configurations are modelled in computer based analysis software 'Cycle-Tempo' at different operating conditions and the detailed thermodynamic study is carried out based on Energy, Exergy and Environmental (3-E) analysis. Result shows that the net plant energy and exergy efficiencies of ACC based 500MW SupC steam power plant with CO_2 capture are about 40.33 % and 36.91 %, respectively which is higher than the OCC based power plant by about 6.21 % and 5.7 %, points respectively. This performance reduction is due to more auxiliary power consumption by the Air Seperation Unit (ASU) of OCC based power plant which is about 1.94 times higher than the ACC based power plant. Environmental benefits of OCC based power plant is more than the ACC based power plant as amount of emissions of CO_2 to atmosphere is about 0.141 kg/kWh which is about 16.73 times lower than the value observed in ACC based power plant. For the OCC based plant, amount of dry fluegas at the inlet of CO_2 capture system is lower than the ACC based plant and thereby amount of CO_2 capture is

reduced by about 0.08 kg/kWh. It is also analyzed that the performance of CO_2 Capture Unit (CCU) for the OCC based plant is about 80.62% which is about 3.66 times higher than the ACC based plant due to increase in the concentration of CO_2 in the fluegas stream and also the auxiliary power consumption per kg of CO_2 capture is reduced for the OCC based plant. Effect of furnace temperature variation on the performance of OCC based plant is carried out by varying fluegas recirculation and it is found that the efficiency gap in between ACC and OCC based plant reduces but the metallurgical temperature limit of boiler tube materials restrict for using the higher value of furnace temperature.

Keywords: Air-Coal Combustion, CO2 Capture, Oxy-Coal Combustion, Supercritical, Power Plant.

INTRODUCTION

Using solar radiation in concentrated form is viewed as an efficient process of power generation using solar thermal energy. But owing to solar radiation's low intensity, uneven availability and distribution, this process of power generation which utilizes solar energy as the primary form of input is normally costly and has low efficiency. As a result, development of hybrid process of solar/fossil is nessecary which includes systems that utilizes different heat sources at variable temperature levels, e.g as the solar thermal based energy are quite inexpensive, whereas for increasing the energy efficiency the energy resources based on fossil fuel are integrated keeping in view of the cost factor. This hybrid system gives a solution for saving fossil fuels which are depleting and makes a increase in efficiency of conversion of solar heat to power.

Such a hybrid system was proposed by (Lior and co-workers, 1984) named as SSPRE (solar steam powered Rankine Engine). A system called solar thermal aided power generation (SAPG) was suggested by (Hu, 2010) that utilizes solar heat for replacing some of bleed steam in the regenerative Rankine power cycle for heating of feedwater to achieve extra power generation or reduction in consumption of fuel. In India there are about 250-300 days which are having clear sunny sky with a annual radiation amounting to 1600-2200 kWh/m^2 annually(Ramachandra and Shruthi, 2007), contribution of solar energy for production of power is negligible. The main factors which provides a hindrance to the large scale commercialization of power production systems using stand-alone solar power are huge cost of investment and low plant capacity factor.

METHODOLOGY

The plant has single stage of reheating and steam parameters in case

of supercritical conditions are 242.2 bar/537°C/565°C, with final water temperature before entering the economiser being 280°C. In the SupC plant there is one number single-flow HP turbine, two number dual-flow IP turbine, and two numbers of double-flow LP turbines. The number of heat sinks(solar) are two nos. ASU consists of two stage air compressors with intercoolers to obtain mole purity of O_2 at 95%. At the exit of ESP the flue gas passes through the Flue Gas Desulfurization (FGD) and Flue Gas Condenser (FGC). The flue gas at the exit of ESP passes through the Flue Gas Desulfurization (FGD) and Flue Gas Condenser (FGD) to obtain 0.85 mole purity of CO_2 with a CO_2 capture efficiency of 85%. Four-stages of compression and intercooling is done by compressing CO_2 to achieve pressure of 110 bar and to reach 35°C temperature with intercoolers for ease of transportation and storage.

III. RESULTS AND DISCUSSION OF SUPER CRITICAL POWER PLANTS USING HIGH ASH COAL

A. 2-E (Energy & Exergy) based comparative analysis of both plants

Both the energy analysis and exergy analysis has been done for the ACC and OCC based 500MW SupC coal-fired power plants are studies are based on simulated operating data and compared with each other. It is observed that the energy efficiency of the OCC based power plant with fluegas recirculation system are lower than the ACC based power plant by about 6.21 % point due to increase in fuel consumption by about 1.94 % point. Overall, the net plant energy efficiency and net plant exergy efficiency of ACC based 500MW SupC steam power plant with CO_2 capture are about 40.33 % and 36.91 %, respectively and it is higher compared to the OCC based power plant by about 6.21 % and 5.7 %, points respectively. Moreover, higher auxiliary power consumption of OCC based power plant which is about 1.94 times more than ACC based power plant causes less energetic and exergetic plant performances compared of ACC based power plant. For the environment protection, OCC based power plant may be promoted over the ACC based power plant instead of poor plant performance.

B. Environmental Impact of the both Plants

Environmental impact of the ACC and OCC based power plants are studied and it can be seen that the environmental benefits of OCC based power plant

is more compared to the ACC based power plant as the amount of atmospheric emission and the CO_2 captured is drastically reduced to about 0.141 kg/kWh and 0.585 kg/kWh, respectively. Amount of dry flue gas at the inlet of CO_2 Capture Unit (CCU) is lower than the ACC based plant and thereby amount of CO_2 capture is reduced by about 0.08 kg/kWh compared to ACC based power plant. It is also analyzed that the performance of CCU for the OCC and ACC based plants are about 80.62 and 22.05 point, respectively and the same is shown in Fig.7.7. The performance of CCU for the OCC based power plant is higher than the ACC based power plant which is about 3.66 times as the CO_2 concentration increases in the fluegas stream. From Fig.7.9, it is found that the auxiliary power consumption of the OCC based power plant is about 24.862 % of total generation and as compared to the ACC based power plant it is higher due to additional power consumed by the Air Seperation Unit (ASU). It is also analyzed from Fig.7.9 that the power consumption per kg of CO_2 capture for the OCC based power plant is about 510.968 kWh/kg which is about 1.06 times lower than the ACC based plant and this reduction is due to increase the performance of CO_2 Capture Unit (CCU) of OCC based plant.

CONCLUSIONS

Major conclusions which can be drawn from the present study are as follows:

1. Additional power consumption by the ASU and flue-gas recirculation of OCC based power plant cause poor energetic and exergetic performances of the plant.
2. Compared to ACC based plant the environmental effect of OCC based plant is less as the emission of CO_2 to the atmosphere for OCC based plant is lower than the ACC based power plant by about 16.73 times due to lower volume of flue gas emission with a higher concentration of CO_2 present in it.
3. The performance of CCU for the OCCbased plant has higher performance than the ACCbased plant as there is an increase in the concentration of CO_2 in the flue gas stream.
4. It can be seen that in the CO_2 capture unit of the OCC based plant auxiliary power consumption is about 1.06 times less than that for the ACCbased plant and the figure comes to 510.968 kW/Kg and the main reason for this is the higher performance of CCU.

26

A Review of the Latest Research on Direct Energy Deposition Technique Using Wire and Arc Additive Manufacturing

Subhadeep Saha and Ratnesh Kumar

Abstract

Wire Arc Additive Manufacturing, shortened as WAAM has emerged as a noteworthy method in the domain of Additive Manufacturing (AM), enabling the construction of large-scale parts with high efficiency and reduced cost. The Wire Arc Additive Manufacturing (WAAM) process has seen notable advancements due to its cost-effective capability to produce large-scale metal components at higher rates of deposition. This progress encompasses a deeper understanding of the process itself, with the mechanical and microstructural attributes of the created parts. As WAAM has matured, it has been adapted to a diverse array of materials, expanding its application range.

This article delves into the latest research developments on WAAM methodologies and prevalent metal feedstock material. It offers an in-depth analysis of the metallurgical characteristics and material properties of the fabricated parts. The article also highlights common defects observed in wire arc additively manufactured components across various alloys, such as deformation, porosity, and cracking. It further discusses strategies to enhance the quality of the manufactured components, considering the unique needs of different alloys. In

conclusion, while WAAM holds vast potential, its widespread application comes with its set of challenges. Addressing these challenges tailored to individual materials is essential to realize a functional system within a reasonable timeframe. The synergy between materials and the manufacturing process to yield flawless and robust components is a pivotal focus for future endeavours.

Keywords : Additive Manufacturing, Wire Arc Additive Manufacturing**,** metallurgical characteristics, material properties, defects, cold metal transfer.

Introduction

Overview on Additive Manufacturing

Additive manufacturing (AM) is a swiftly advancing technology that has gained widespread acceptance in global manufacturing sectors due to its ability to produce large components with near net shape and high deposition rates. As defined by the American Society for Testing and Materials (ASTM), AM involves creating objects from 3-Dimensional model data by layering materials, thereby distinguishing it from traditional subtractive manufacturing methods. Traditional manufacturing methods often involve extensive machining and may not satisfy the ever-growing demands. The push towards Additive Manufacturing (AM) stems from the desire to automate machining operations, decrease material wastage, lower energy usage and enhance efficiency of the material. Furthermore, AM's capability to craft three-dimensional, free-form components layer-by-layer stands as a significant catalyst for breakthroughs and innovation. [1-4]

History of Additive Manufacturing

Equipment for additive manufacturing and its feedstock material was first started in 1980s by Japanese, French and American scientists. Hideo Kodama of the NMIR (Nagoya Municipal Industrial Research Institute) in 1981 launched two equipments on additive manufacturing photo-polymer system, in which masked pattern or fibre transmitter controls the area of UV exposure.

In 1984, William Masters (Bill Masters), an American cum-producing businessman, patented his Computer Automated Manufacturing System and Method. The first full copyright for the stereolithography system was developed by Charles W. Hull (Chuck Hull) of 3D Systems Corporation. The body is characterized by the method of stereolithography as a three-dimensional method

of producing a pattern of different parts of an object to ed. In this method curing photopolymers with ultraviolet light lasers are used to add the layers. Charles Hull, also known as Chuck Hull, was granted patents in 1986. His company known as 3D Systems Corporation has released the first 3D printer, SLA-1 which is used commercially.

Metal 3D printing first opened with the creation of laser melting and sintering techniques in the 1990s.

SLS (Selective Laser Sintering) and SLM (Selective Laser Melting) are part of DMLS (Direct Metal Laser Sintering). However, the innovation involved by most 3D printers in the 2010s is Fused Filament Fabrication also known as FFF, material extrusion or the proprietary Stratasys division's Fused Deposition Modelling also known as FDM. FDM was patented for 20 years in 1989 by S. Scott Crump.

1.3 Classification of Additive Manufacturing techniques

The ASTM (American Society for Testing and Materials) international committee has classified AM processes into seven distinct categories, as outlined in Figure 2 [8]. It's worth highlighting that all seven categories have profound commercial applications in the domain of Additive Manufacturing industry.

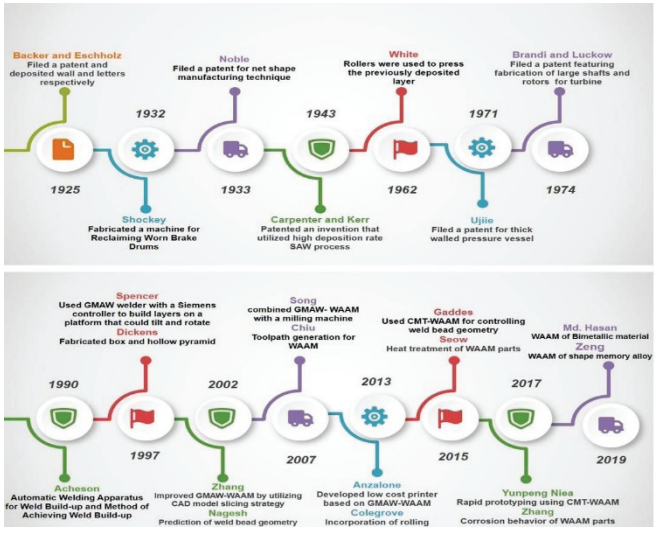

Figure 1: History of AM [5-7]

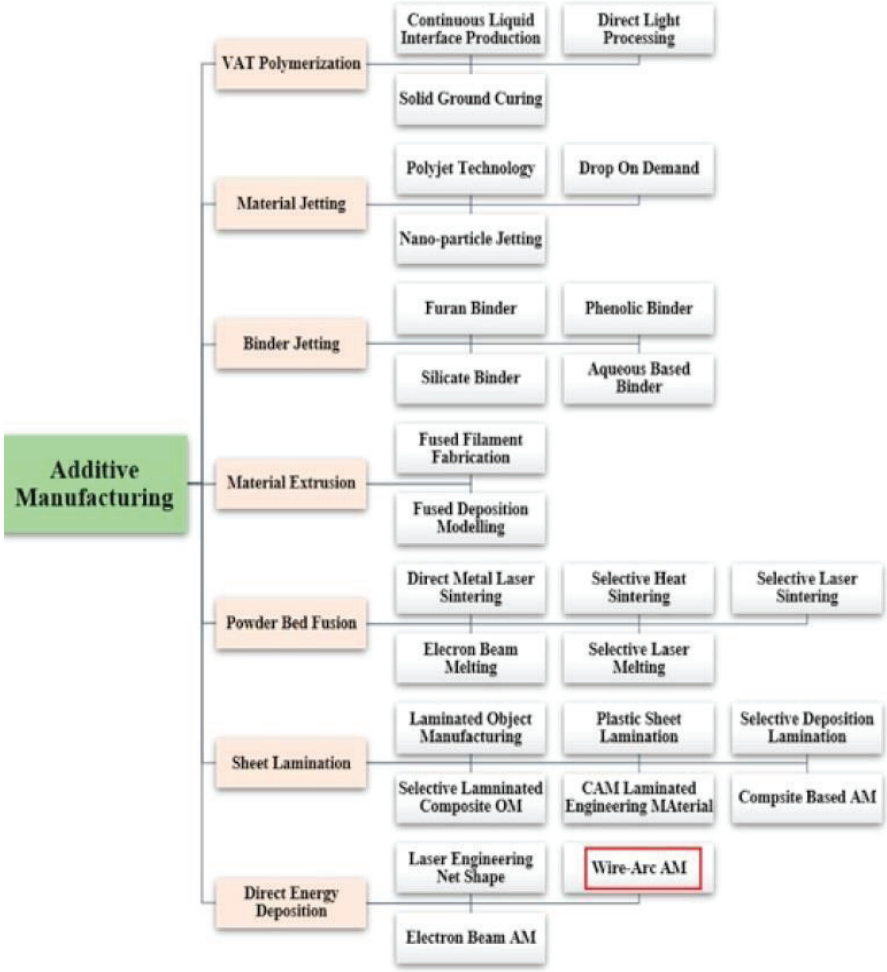

Figure 2: Seven Categories in Additive Manufacturing [8]

The seven main categories of additive manufacturing technology has been presented in Table 1, that include Vat Photo-polymerization, Material Extrusion, Material Jetting, Binder Jetting, Sheet Lamination, Powder Bed Fusion and Directed Energy Deposition (DED).

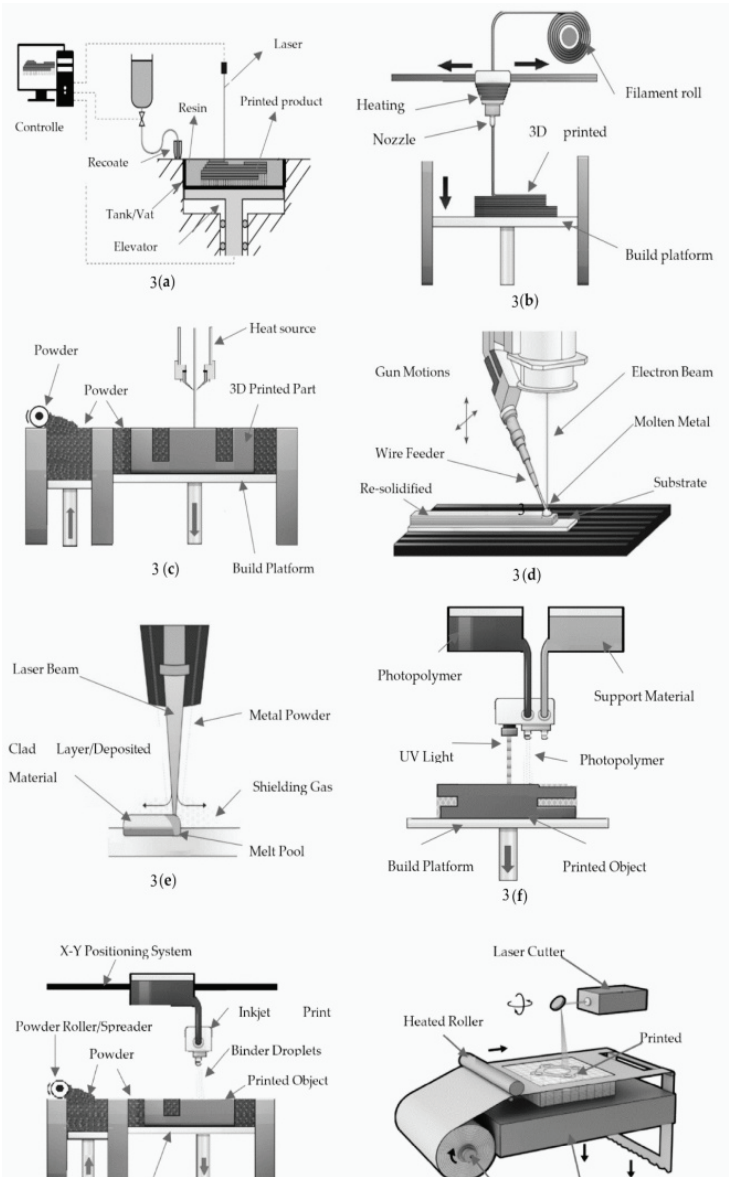

Figure 3: Seven AM processes [25,26]

Based on data published by Cherdo [27], Figure 4 showcases the varied industrial uptake of AM processes. From the data, it's evident that only two of these processes are predominantly utilized for metals, which will be elaborated upon in the subsequent sections.

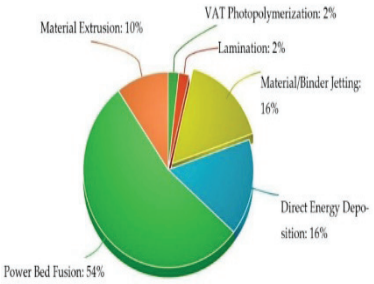

Figure 4- Pie Chart showing Market share of Metal Additive manufacturing [27]

Wire Arc Additive Manufacturing

Wire and Arc Additive Manufacturing (WAAM) is a subset of Direct Energy Deposition (DED) technology that employs arc welding techniques to fabricate three-dimensional metal parts. While WAAM might not be as widely recognized as other processes, it holds significant promise for large-scale production across various industries. Unlike powder-based DED methods, WAAM melts metallic feedstock wire using an electric arc as its heat source. Guided by a robotic arm, the design is constructed on a substrate base plate. Once the part is complete, it's detached from this base. The molten wire is deposited in bead-like walls onto the substrate. As these beads are continuously laid down, they coalesce to form a solid layer of the metal object. This procedure is iteratively performed until the desired 3D shape is achieved.

Materials used for WAAM

WAAM supports a range of various metal feedstock materials, provided they are in the form of wire, such as:

- Mild steel, stainless steel,
- Carbon and low alloy steels,
- Aluminium Alloys (mostly AL-Mg alloys),
- Titanium Alloys (mostly Ti-6Al-4V),
- Inconel (mostly IN718, IN625),
- Copper etc.

Advantages and disadvantages of WAAM

The improvement of WAAM is being driven by the requirement for increased manufacturing efficiency of engineering structures. Some advantages and limitations of WAAM technique is presented in Table 2.

Table 2: Advantages and disadvantages of WAAM

Advantages of WAAM	Disadvantages of WAAM
WAAM is better at 3D printing large metal parts than PBF metal AM technologies.	Near-net-shape parts with poor accuracy and surface quality are typically produced.
Cheaper method than other AM methods and wire materials are easily available.	Machining is needed after job completion, thereby decreasing productivity.
High-quality parts eminent for their strong mechanical properties and high density.	It involves high working temperature which causes build-up of residual stresses, that often leads to deformation in a component.
It's suitable for fixing and maintenance tasks for explicit parts like turbine blades.	Shielding gas is needed in certain cases (like titanium).
By the deposition of new materials on damaged part, it can fix the component.	WAAM technique has distorted welding heat input.

Applications of WAAM

With new innovations like wire and arc additive manufacturing, it requires investments for applications to create and felt throughout the business. In any case, we see the interest for huge metal 3D-printed parts suggesting, developing and recommending that the reception of WAAM will speed up. Some of the applications of WAAM are shown in Figure 5:

1. Production of marine parts such as the ship's propeller.
2. Large offshore crane hook for lifting operations.
3. 3D-printed steel bridge.
4. Locomotive metal wheel-set bearing cover.
5. Repair of impeller fan blade.
6. Rotors, Turbine Nozzles etc.

There are six steps to Fabricate a 3-dimensional product from scratch using WAAM, as shown in Figure 6. These include substrate plate penetration, deposition of metal by arc welding method, heat treatment to improve mechanical and metallurgical properties, machining to improve surface finish and achieve dimensional accuracy, substrate or support removal from the as built part and the last step is inspection of the fabricated part for defects.

Figure 5: Applications of WAAM [28,29,30]

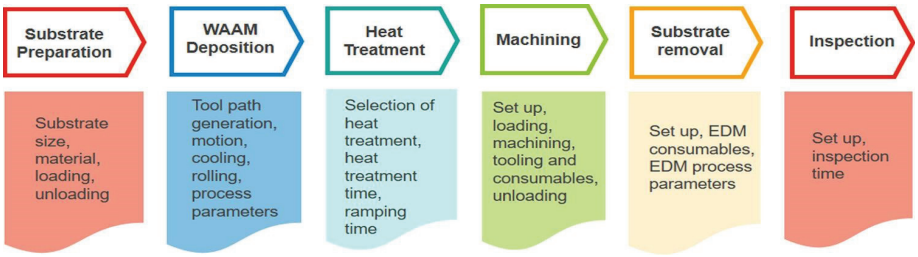

Figure 6: Fabrication steps in WAAM [Laukik et al.]

Conclusion

This paper provides a comprehensive review of the latest technological advancements in the WAAM process, highlighting its historical evolution, benefits, drawbacks, industrial applications, feedstock materials, process-related defects, defect mitigation, and post-processing treatments. WAAM is

an emerging technology with research delving into its applicability for various materials and alloys, including nickel, aluminium, steel, bronze alloys and many more. The potential of WAAM in advanced materials like functionally graded materials or high entropy alloys warrants exploration. Each deposited layer in the WAAM process undergoes a unique thermal journey, influencing the microstructure of the samples, which impacts the attributes like grain structure, grain size, and phase transformations. Some researchers advocate for the control of process parameters that affect grain characteristics, such as wire feed speed, travel speed, and heat input. Deposition rate is pivotal for both productivity and cost-effectiveness. Defects observed in WAAM-fabricated parts, like porosity, deformation and cracking are intrinsically tied to the chosen material's properties and process parameters. Some of these defects can be mitigated through postprocessing techniques. There's a need for a versatile WAAM machine capable of handling a broad spectrum of materials and integrating multiple manufacturing processes. Given its extensive applications and superior mechanical and microstructural properties, WAAM presents a promising alternative to conventional manufacturing techniques. Its potential spans across various engineering and medical sectors. As research progresses, more refined solutions are anticipated in the near future.

REFERENCES

1. Attaran M. The rise of 3-D printing: the advantages of additive manufacturing over traditional manufacturing. Bus Horiz 2017;60:677e88. https://doi.org/10.1016/ j.bushor.2017.05.011.
2. Mu¨ ller J, Grabowski M, Mu¨ ller C, Hensel J, Unglaub J, Thiele K, et al. Design and parameter identification of wire and arc additively manufactured (WAAM) steel bars for use in construction. Metals 2019;9. https://doi.org/10.3390/ met9070725.
3. Huang R, Riddle M, Graziano D, Warren J, Das S, Nimbalkar S, et al. Energy and emissions saving potential of additive manufacturing: the case of lightweight aircraft components. J Clean Prod 2016;135:1559e70. https://doi.org/10.1016/ j.clepro.2015.04.109.
4. Rodrigues TA, Duarte V, Miranda RM, Santos TG, Oliveira JP. Current status and perspectives on wire and arc additive manufacturing (WAAM). Materials 2019;12. https://doi.org/ 10.3390/ma12071121
5. J.D. Spencer, P.M. Dickens and C.M. Wykes, Rapid Prototyping of Metal Parts by ThreeDimensional Welding, Proc. Inst. Mech. Eng. Part B J. Eng. Manuf., 1998, 212, p 175–182. https://doi.org/10.1243/ 0954405981515590

6. Y.M. Zhang, Y. Chen, P. Li and A.T. Male, Weld Deposition-Based Rapid Prototyping: A Preliminary Study, J. Mater. Process. Technol., 2003, 135, p 347–357. https://doi.org/10.1016/S0924-0136(02)0086 7-1
7. Y. Nie, P. Zhang, X. Wu, G. Li, H. Yan and Z. Yu, Rapid Prototyping of 4043 Al-Alloy Parts by Cold Metal Transfer, Sci. Technol. Weld. Join., 2018, 23, p 527–535. https://doi.org/10.1080/13621718.2018. 1438236
8. Ransikarbum, K.; Pitakaso, R.; Kim, N. A Decision-Support Model for Additive Manufacturing Scheduling Using an Integrative Analytic Hierarchy Process and Multi-Objective Optimization. Appl. Sci. 2020, 10, 5159
9. Cherdo, L. The Best Metal 3D Printers in 2020. Available online: https://www.aniwaa.com/best-of/3d-printers/best-metal-3dprinter/ (accessed on 8 January 2021).
10. Piñero Vega, D.; Batista Ponce, M.; Valerga Puerta, A.P.; Vazquez Martinez, J.M.; Fernandez Vidal, S.R. A Comparison of Macro and Microgeometrical Properties of Specimens Made with a FDM Commercial Printer and Its Opensource Retrofit Version. Ann. DAAAM Proc. 2018, 29, 1108–1115.
11. Hu, G.; Cao, Z.; Hopkins, M.; Lyons, J.G.; Brennan-Fournet, M.; Devine, D.M. Nanofillers can be used to enhance the thermal conductivity of commercially available SLA resins. Procedia Manuf. 2019, 38, 1236–1243.
12. Caccia, M.; Tabandeh-Khorshid, M.; Itskos, G.; Strayer, A.; Caldwell, A.; Pidaparti, S.; Singnisai, S.; Rohskopf, A.; Schroeder, A.; Jarrahbashi, D. Ceramic–metal composites for heat exchangers in concentrated solar power plants. Nature 2018, 562, 406.
13. Sakly, A.; Kenzari, S.; Bonina, D.; Corbel, S.; Fournée, V. A novel quasicrystal-resin composite for stereolithography. Mater. Des. (1980–2015) 2014, 56, 280–285.
14. Roberson, D.A.; Perez, A.R.T.; Rocha, C.R. Methods and Compositions for Material Extrusion 3D Printing. Google Patents US20160160073A1, 9 June 2016.
15. Miyanaji, H.; Momenzadeh, N.; Yang, L. Effect of printing speed on quality of printed parts in Binder Jetting Process. Addit. Manuf. 2018, 20, 1–10.
16. Wheat, E.; Vlasea, M.; Hinebaugh, J.; Metcalfe, C. Sinter structure analysis of titanium structures fabricated via binder jetting additive manufacturing. Mater. Des. 2018, 156, 167 183.
17. Wong, K.V.; Hernandez, A. A Review of Additive Manufacturing. ISRN Mech. Eng. 2012, 2012, pp. 1–10.
18. Guo, H.; Gingerich, M.B.; Haedings, L.M.; Hahnlen, R.; Dapino, M.J. Joining of carbon fiber and aluminum using ultrasonic additive manufacturing (UAM). Compos. Struct. 2019, 208, 180–188.
19. Vilardell, A.; Takezawa, A.; du Plessis, A.; Takata, N.; Krakhmalev, P.; Kobashi, M.; Yadroitsava, I.; Yadroitsev, I. Topology optimization and characterization of Ti6Al4V ELI cellular lattice structures by laser powder bed fusion for biomedical applications. Mater. Sci. Eng. A 2019, 766, 138330.

20. Kretzschmar, N.; Ituarte, I.F.; Partanen, J. A decision support system for the validation of metal powder bed-based additive manufacturing applications. Int. J. Adv. Manuf. Technol. 2018, 96, 3679–3690.
21. Chen, C.; Gojon, S.; Xie, Y.; Yin, S.; Verdy, C.; Ren, Z.; Liao, H.; Deng, S. A novel spiral trajectory for damage component recovery with cold spray. Surf. Coat. Technol. 2017, 309, 719– 728.
22. Yan, X.; Huang, C.; Chen, C.; Bolot, R.; Dembinski, L.; Huang, R.; Ma, W.; Liao, H.; Liu, M. Additive manufacturing of WC reinforced maraging steel 300 composites by cold spraying and selective laser melting. Surf. Coat. Technol. 2019, 371, 161–171.
23. Cunningham, C.; Flynn, J.; Shokrani, A.; Dhokia, V.; Newman, S. Invited review article: Strategies and processes for high quality wire arc additive manufacturing. Addit. Manuf. 2018, 22, 672–686.
24. Wu, B.; Pan, Z.; Ding, D.; Cuiuri, D.; Li, H.; Xu, J.; Norrish, J. A review of the wire arc additive manufacturing of metals: Properties, defects and quality improvement. J. Manuf. Process. 2018, 35, 127–139.
25. Diegel, O.; Nordin, A.; Motte, D. Additive Manufacturing Technologies. In A Practical Guide to Design for Additive Manufacturing; Springer: Singapore, 2019; pp. 19–39.
26. Barbosa de Lima, J.C. Laminated Object Manufacturing. Available online: https://www.manufacturingguide.com/en/laminatedobject-manufacturing-lom
27. Cherdo, L. The Best Metal 3D Printers in 2020. Available online: https://www.aniwaa.com/best-of/3d-printers/best-metal-3dprinter/
28. Graves, J. Nexxt Spine Develops AM Spinal Implants Using MTS Test Systems; Nexxt Spine: Noblesville, IN, USA, 2019; p. 89.
29. Camacho, D.D.; Clayton, P.; O'Brien, W.; Ferron, R.; Juenger, M.; Salamone, S.; Seepersad, C. Applications of additive manufacturing in the construction industry—A prospective review. In Proceedings of the 34th International Symposium on Automation and Robotics in Construction and Mining (ISARC 2017), Taipei, Taiwan, 27–30 June 2017.
30. Siemens. Fast, Efficient, Flexible: Additive Manufacturing (3D-Printing) in the Energy Sector. Available online: https: //new.siemens.com/global/en/products/energy/services/maintenance/parts/additivemanufacturing.html (accessed on 21 November 2020).
31. Liu J, Xu Y, Ge Y, Hou Z, Chen S. Wire and arc additive manufacturing of metal components: a review of recent research developments. Int J Adv Manuf Technol 2020; 111:149e98. https://doi.org/10.1007/s00170-020-05966-8.
32. Almeida, P.M.S., Williams, S., "Innovative Process Model of Ti-6Al-4V Additive Layer Manufacturing using Cold Metal Transfer (CMT)", Proceedings of the 21st Annual International Solid Freeform Fabrication Symposium, January 2010.

33. Sizova, I., Hirtler, M., Günther, M., Bambach, M., "Wire-Arc Additive Manufacturing of Pre-forms for Forging of a Ti–6Al–4V Turbine Blade", AIP Conference Proceedings 2113, July 2019.
34. Mishurova, T., Sydow, B., Thieda, T., Sizona, I., Ulbricht, A., Bambach, M., Bruno, G., "Residual Stress and Microstructure of a Ti-6Al-4V Wire Arc Additive Manufacturing Hybrid Demonstrator", Metals, Vol. 10, Issue 6, 701, February 2020.
35. C.V. Haden, G. Zeng, F.M. Carter, C. Ruhl, B.A. Krick and D.G. Harlow, Wire and Arc Additive Manufactured Steel: Tensile and Wear Properties, Addit. Manuf., 2017, 16, p 115–123. https://doi.org/10. 1016/j.addma.2017.05.010
36. L. Wang, J. Xue and Q. Wang, Correlation Between Arc Mode, Microstructure, and Mechanical Properties During Wire Arc Additive Manufacturing of 316L Stainless Steel, Mater. Sci. Eng. A, 2019, 751, p 183–190. https://doi.org/10.1016/j.msea.2019.02.078
37. X. Zhang, Q. Zhou, K. Wang, Y. Peng, J. Ding, J. Kong et al., Study on Microstructure and Tensile Properties of High Nitrogen Cr-Mn Steel Processed by CMT Wire and Arc Additive Manufacturing, Mater. Des., 2019, 166, p 107611. https://doi.org/10.1016/j.matdes. 2019.107611
38. V.T. Le and D.S. Mai, Microstructural and Mechanical Characteristics of 308L Stainless Steel Manufactured by Gas Metal Arc Welding- Based Additive Manufacturing, Mater. Lett., 2020 https://doi.org/10. 1016/j.matlet.2020.127791
39. Abe, T., Sasahara, H., "Layer geometry control for the fabrication of lattice structures by wire and arc additive manufacturing", Additive Manufacturing, Vol. 28, pp. 639-648, August 2019.

27

Mixed Convection in A Rotating Trapezoidal Enclosure Heated trom the Bottom

Saurabh Chhipa, Geeta Verma, Rabindra Nath Barman

Abstract

Laminar, steady state, mixed convection of Newtonian fluids in a rotating trapezoidal enclosure with a temperature difference imposed on the top and bottom ends is being analyzed by numerical simulation for different values of Reynolds number (i.e. 0 1) and inclination angles (i.e. for nominal Prandtl number. To conduct the parametric analyses finite volume solver is used to study the effect of different Reynolds numbers and inclination angles on Nusselt number.

Introduction

Enclosure refers to a space that is closed off by walls, Enclosure often contains heat sources and heat sinks such as electronic components that can influence heat transfer within the enclosure. Industrial applications are food processing, chemical reactors, biomedical equipment, and HVAC. The design and shape of the enclosure depend on requirements like rectangular, cylindrical, spherical, tubular, and trapezoidal. The study of Bingham fluids and Newtonian fluid has been considered [1] for trapezoidal enclosures heated from the bottom and adiabatic from the top wall with cooled side walls offering

natural convection study showed a variation of mean Nusselt number with different Rayleigh number . The Rayleigh–Bénard convection heated from the bottom wall and cooled from the top wall with adiabatic inclined side walls within trapezoidal enclosures filled with viscoplastic fluid has been analyzed by Aghighi et al. [4] for a range of parameters the angle of inclination of the side walls φ, Rayleigh number *Ra* and Prandtl number *Pr*. The consequence of the centrifugal field on the heat transfer by thermally induced fluid motion has been studied [2] for vertical cylinders having temperature differences between both ends with adiabatic from the side walls for varying ranges of Reynolds numbers having specific Grashof number. In this paper, a mixed convection in a vertical rotating trapezoidal enclosure with a temperature difference imposed on the top and bottom ends is investigated. To find the effect of inclination angle and Reynolds number on Heat transfer.

Methodology and Numerical Techniques

The schematic of the computational domain considered in the analysis is shown in Fig. 1 where L is the length of the bottom wall, H is the height of the trapezium whose aspect ratio is H/L to be unity having inclination angle of sidewall. The no-slip condition is applied to all walls. The fluid flow inside the enclosure assumes two dimensional laminar, steady, and incompressible. The boundary conditions are a hot bottom wall, a cold top wall with adiabatic sidewalls and the entire enclosure is rotating about the central axis of the domain. Numerical simulations are performed using the commercial software ANSYS Fluent and the governing equations are integrated by finite volume method by using a double precision method. The numerical model has been validated with Natural convection of Newtonian fluids in trapezoidal enclosure with differentially heated bottom wall and sidewalls with adiabatic top wall, for different inclination angles [1] for all cases satisfactory results were obtained. Fig. 2 represent the graph of local Nusselt number with normalised horizontal dimension and Fig.3 represent the contours of non-dimensionalized temperature in the domain for the configuration Ra = 10^3, Pr = 10^3, φ 30.

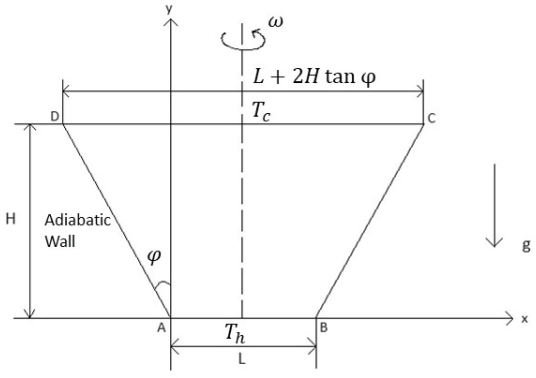

Figure 1: Shape of the computational Domain

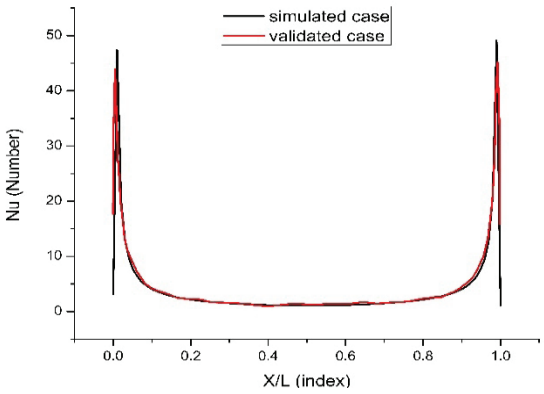

Figure 2: Validation of local Nusselt number with normalised horizontal distance a with present study with reference paper for Ra = 10^3, Pr = 10^3, φ 30°

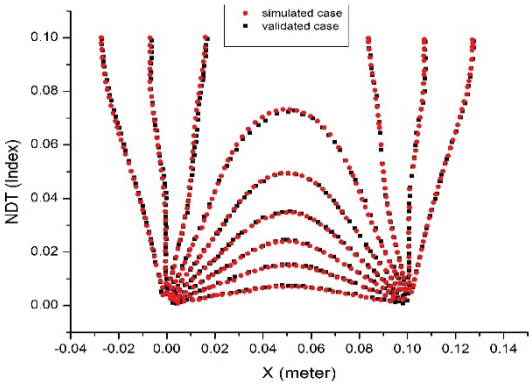

Figure 3: Validation of contour of non-dimension temperature with reference paper for Ra = 10^3, Pr = 10^3, φ 30°

Results and Discussion

In this section, the effects of Re on the heat transfer behaviour in the trapezoidal enclosure are discussed. The variations of local Nusselt number on the hot bottom wall with normalised horizontal distance x/L for Re = 0, Re = 0.1, Re = 1 where Pr = 10^3 and Ra = 10^3 for Newtonian fluid with inclination angel φ = 30°are shown in fig 5. It shows that Nu increases with increasing Re

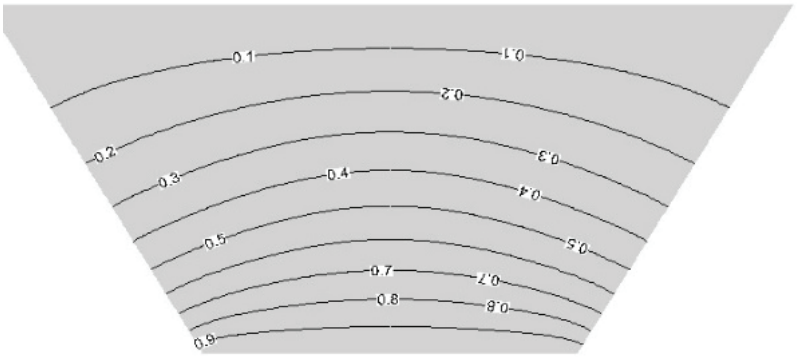

Figure 4: Contour of non-dimension temperature for Newtonian fluid for Ra = 10^3, Pr = 10^3, φ 30°

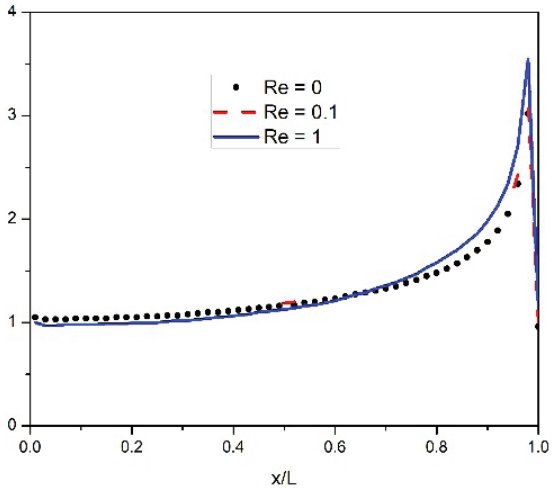

Figure 5: Variations of local Nusselt number on the hot bottom wall with normalised horizontal distance x/L for Re = 0, Re = 0.1 and Re = 1 where Pr = 10^3 for Newtonian fluid, inclination angle φ 30°

Conclusions

Laminar, steady, mixed convection of Newtonian fluid in trapezoidal enclosure with a heated bottom wall, cooled top wall and adiabatic sidewalls has been analysed based on Ansys fluent solver for a range of Re (i.e. 0 1). It has been found that Nu increasing with increasing Re due to rotational effect.

REFERENCES

[1] S.Alshaaili, S.P.Malkeson, N.Chakraborty "Laminar natural convection of Bingham fluids in a trapezoidal heated from the bottom", 17th UK heat transfer conference (UKHTC2021).

[2] Zeng Yuan Guo, Chao min zhang "Thermal drive in centrifugal fields-mixed convection in a vertical rotating cylinder". lnt. J. Hear Mass Transfer (1991), vol. 35, No.7, pp. 1635-1644, 1992.

[3] Kamil Kahveci, Mehmet Cem Ece "Thermal Convection in a closed vertical rotating circular cylinder heated from the top". ASME International Mechanical Engineering Congress (2008), IMECE2003-41121, pp. 179-188.

[4] M.S. Aghighi, A. Ammar, H. Masoumi & A. Lanjabi, Rayleigh–Bénard convection of a viscoplastic liquid in a trapezoidal enclosure. International Journal of Mechanical Science, 180 (2020) 105630.

[5] M.P.Escudier "Observations of the flow produced in a cylinder container by a rotating endwall" Experiments in Fluids, Vol.2, Issue 4, pp.189-196

[6] ANSYS Fluent User's Guide 2021.

28

Measure the Mechanical Property and Microstructure Prepared By Low Cost New Hybrid Reinforced MMC

Uttam Kumar Mandal, Debashis Podder, and Sujoy Chakraborty

Abstract

Aluminium-6063 and Copper alloy is used to prepare the MMC. A mixer of Zirconium Oxide and Titanium Oxide of different particle size has reinforced into base metal by using stirrer mechanism. The microstructure and mechanical properties has been checked in this research work. This research work has been done to check the effect of SPS (Single particle size), DPS (Double particle size) and TPS (Triple particle size) of ZrO_2 and TiO_2 abrasive mixer, and other process parameters like percentage of abrasive, percentage of copper, abrasive particles size, percentage of brick powder, cooling time, percentage of binder and stirring time on the fracture toughness of the MMC.Taguchi's L18 is used to minimize the number of experiments. Microstructure of the casted product has obtained by using optical microscope.

Keywords: Hybrid Abrasive, Particle Size, Fracture Toughness

INTRODUCTION

MMC has better mechanical and physical properties than the base metal. It has better elastic modulus; increased hardness and strength, improved wear resistance, lower coefficient of thermal expansion and better electrical and thermal conductivity [1]. On the basis of reinforcement MMCs are divided

into three types; fiber reinforced, polymer reinforced and particle reinforced metal matrix composites. These different types of reinforcements provide the composite with improved properties which cannot be achievable in monolithic alloys [2].Metal matrix composites have a vast application area all over the world [3-9]. In automotive engineering, MMCs are widely using for making different parts of it [10].Feng and Froyen in 2000 used in-situ process to develop aluminium based TiO_2 reinforced MMC. Al_3Ti and Al_2O_3 have been used to form Al-TiO_2 at high temperature [11]. Zhu et al. in 2008 used exothermic propagation method to prepare Al–TiO_2–B_2O_3 MMC. The wear resistance property has improved due the presence of B_2O_3 and other mechanical properties have been improved due to the presence of TiO_2 [12]. Wittig et al. in 2008 prepared ZrO_2 based MMC and the Young's modulus and bending strength has been found to be better than the base metal due the presence of the ZrO_2 [13]. Different mechanical properties can be improved by using ZrO_2 as reinforcement [14]. A number of research works is found with SiC and Al_2O_3, few with ZrO_2 and TiO_2 as reinforcement in aluminium matrix. But no any work has been found with the combination of ZrO_2 and TiO_2 as reinforcement in Al-Cu alloy matrix. So in this research this combination has been used to prepare a new material.

METHODS

The whole casting method has been divided into six steps which are as follows:

Step 1: The first step was to preheat the mixer of abrasive (1:1) in muffle furnace at a temperature of1100°C for half an hour.

Step 2: Experiment has been started with the formation of mould. For the present research work three types of binders have used which are cow-dung, molasses and starch.

Step 3: Cope and drag parts have beenfilled with sand separately and place the pattern and sprue. After ramming of the mold removal of the pattern has been done.

Step 4: The copper pieces and the aluminium pieces have been melted and mixed in the crucible at 1100°C.

Step 5: After the preparation of copper-aluminium alloy the preheated abrasive was brought and poured to the matrix and stir it with the help of stirrer

mechanism for different sequence of time for different experiments as it was set in the Taguchi's L18 Array.

Step 6: Whenever mixing has done, bring it to the mould and poured into the mould and leave it for solidification. Three thermocouples were placed at an equal distance of 2cm. to measure the rise and fall in temperature through the mould.

MATERIALS

An alloy of Copper of different percentage has been added to aluminium to prepare the matrix. By adding the copper into aluminium the strength heat and electric conductivity can be increased. A hybrid abrasive of ZrO_2 and TiO_2 of different particle size has been used as reinforcement. Single particle size (SPS), double particle size (DPS), triple particle size (TPS) of the mixer of the abrasive is used. 7%, 12% and 17% of weight percentage of the hybrid abrasive is used as reinforcement. The ratio of ZrO_2 and $TiO_2$was 3:7, 1:1 and 7:3. The base metal is prepared by adding 20%, 33% and 54% of copper into the aluminium.

EXPERIMENT

Now based on Table 1 the castings were prepared for 18 sets of experiments and correspondingly micro-hardness tests have been performed on Vickers hardness (HV) testing machine.

Table-1: Input parameters and their levels

Sl. No.	Parameters	Level 1	Level 2	Level 3
A.	Percentage of binder	5%	10%	--
B.	Percentage of Hybrid Abrasive	50% of each	30% of ZrO_2+ 70% of TiO_2	30% of TiO_2+ 70% of ZrO_2
C.	Percentage of Abrasive	7% of Hybrid Abrasive	12% of Hybrid Abrasive	17% of Hybrid Abrasive
D.	Percentage of copper mixed in aluminium	20% of copper	33% of copper	54% of copper
E.	Size of abrasive	SPS	DPS	TPS
F.	Stirrer time	5 minutes	7 minutes	12 minutes

G.	Percentage of brick powder	50% of each	25% of each	0% of each
H.	Cooling time	25 min	30 min	35 min

Table-2: Control log of experimentation

Experiment	Percentage of binder	Percentage of Hybrid Abrasive	Percentage of Abrasive	Percentage of copper mixed in aluminium	Size of abrasive	Stirrer time	Percentage of brick powder	Cooling time
1.	1	1	1	1	1	1	1	1
2.	1	1	2	2	2	2	2	2
3.	1	1	3	3	3	3	3	3
4.	1	2	1	1	2	2	3	3
5.	1	2	2	2	3	3	1	1
6.	1	2	3	3	1	1	3	3
7.	1	3	1	2	1	3	2	3
8.	1	3	2	3	2	1	3	1
9.	1	3	3	1	3	2	1	2
10.	2	1	1	3	3	2	2	1
11.	2	1	2	1	1	3	3	2
12.	2	1	3	2	2	1	1	3
13.	2	2	1	2	3	1	3	2
14.	2	2	2	3	1	2	1	3

15.	2	2	3	1	2	3	2	1
16.	2	3	1	3	2	3	1	2
17.	2	3	2	1	3	1	2	3
18.	2	3	3	2	1	2	3	1

By using the above stated 18 set up all the casting has done and 18 casted MMC pieces has been found. All the 5x5x5 cm^3 pieces has been cut into small pieces for performing different experiments.

RESULT AND DISCUSSION

Charpy Impact Test

A 48 mm long and 10 mm width piece has cut out from all the 18 casted MMCs for impact test. At the middle of all the pieces a triangular section at 45^o angle and 2mm depth has cut for the experiment purpose. By using Charpy Impact test impact toughness or fracture toughness can be measured. The oscillating hammer strikes the piece with impact energy. With reference to this impact energy, the fracture toughness can be measured.

Table-3: Observations of all18 experiments

Specimen No.	Impact energy on the specimen (in KJ)	**Fracture Toughness* (in KJ/m^2)**	**Room Temperature**
1.	10	2083.33	38
2.	15	3125	38
3.	20	4166.67	38
4.	12	2500	38
5.	12	2500	38
6.	10	2083.33	38
7.	15	3125	38
8.	12	2500	38
9.	15	3125	38
10.	10	2083.33	38
11.	12	2500	38
12.	20	4166.67	38

13.	15	3125	38
14.	10	2083.33	38
15.	10	2083.33	38
16.	20	4166.67	38
17.	15	3125	38
18.	12	2500	38

*Fracture = Impact Energy/ Area

(e.g. for the specimen no. 1, Fracture Toughness= 10/0.0048 = 2083.33 KJ/m^2)

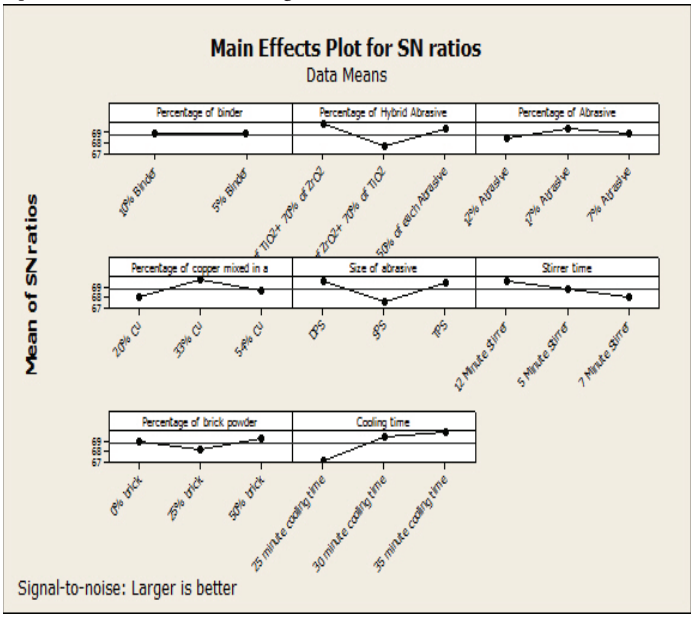

Figure 1: SN graph for impact energy

As per SN graph 5% of binder, (30% of TiO_2+ 70% ofZnO_2) of Hybrid Abrasive, 7% of Abrasive, 33% of copper mixed in aluminium, TPS abrasive size, 12 minutes Stirrer time, 50% of brick powder and 35 minutes Cooling time can give the best result for the impact strength. This set-up of parameters is almost matching with the experiment no. 7. From the observation table it has found that this sample is showing the best result.

The reason behind getting this much of impact strength value is because of following reasons:

1. Use of 5% of binder to make the mold increases its compactness as a

result heat flow has done slowly and impact strength of the casted product become higher.

2. 30% of TiO_2+ 70% of$ZnO_2$is giving the highest impact strength value as impact strength of TiO_2 is smaller than the ZrO_2 as a result this combination is showing the highest impact strength value
3. 7% of hybrid abrasive is giving the better impact strength value as it is the minimum percentage of the abrasive material.
4. 33% copper with aluminium is giving better impact strength value.
5. In case of SPS 50µm of both the abrasive particles have used to produce the MMC. In case of DPS, mixer of 50µm and 30µm of both of the abrasive particles have used as a result quantity of abrasive particles is greater in case of DPS than the SPS per unit weight/volume. TPS particle size has the more quantity of abrasive particles per unit weight/volume as it is consist of 50µm, 30µm and 10µm sizes of abrasive particles. As a result TPS particle size is giving the best impact strength value.
6. 12 minutes of stirrer time is the highest stirring time as stirring time increases proper mixing of the abrasive particles as a result of this more stirring time is giving better impact strength value.
7. 50% of brick powder is the highest percentage of brick powder in the mold and this brick powder increases the permeability of the mold as a result impact strength increases.
8. 35 minutes cooling time is the maximum cooling time. In this case the heat flow has been done slowly as a result impact strength become higher.

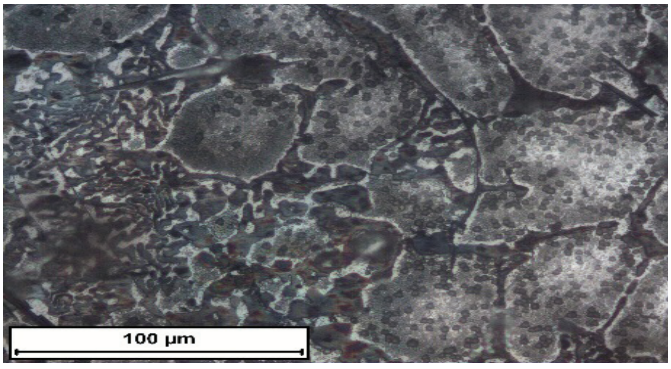

Figure 2: Microstructure of the MMC Figure

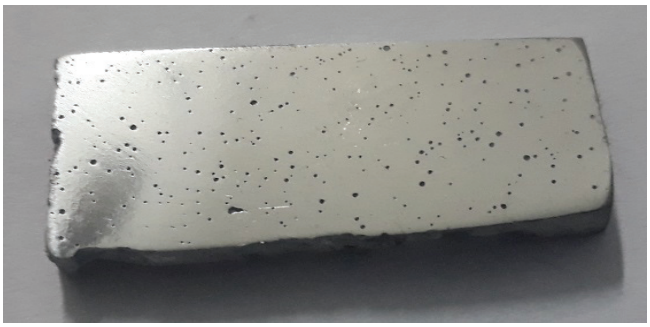

Figure 3: Sample piece

CONCLUSION

A damage in the appearance of a scratch, crack, fracture or break may takes place in two objects when they collide with each other. That's why it is necessary to know about the behavior of the materials under impact load and the magnitude of forces they can resist.

Impact strengthis the output response in this present study. The effects of different process parameters have been successfully investigated on the output response. The surface characterization (Figure: 2) was also performed by using optical microscope. The conclusions are summarized as follows:

1. A wide range of impact strength (10-20 kJ) has been observed in different parametric combinations of percentage of hybrid abrasive, size of abrasive particles, mould binder and stirring time.
2. Percentage of abrasive also plays a vital role on the impact strength of the composite. It has been observed that 17% of hybrid abrasive shows the highest impact strength value and 12% of hybrid abrasive gives lower impact strength value.
3. 30% of TiO_2 + 70% of ZrO_2 gives the highest impact strength and 30% of ZrO_2+ 70% of TiO_2 gives lowest impact strength which may be due to the higher percentage of ZrO_2. This higher percentage of ZrO_2 than the TiO_2 increases the strength of the MMC.
4. It has also been observed that TPS particle size is giving highest impact strength and SPS particle size is giving the lowest. As TPS is having more quantity of particles in the MMC and SPS has the minimum due to this TPS particle size is showing highest impact strength value.

5. As per SN graph 5% of binder, (30% of TiO_2+ 70% ofZnO_2) of Hybrid Abrasive, 7% of Abrasive, 33% of copper mixed in aluminium, TPS abrasive size, 12 minutes Stirrer time, 50% of brick powder and 35 minutes cooling time can give the best result for the impact strength.
6. Microscopic image analysis evidenced the presence of abrasive particles comprising of ZnO_2 and TiO_2 on the aluminium-copper matrix composite.
7. From the study, it has also been observed that the impact strength value of the composite is 10 to 12 times more than the base material.

ACKNOWLEDGMENT

The authors are very much grateful to the Production Engineering Department, NIT Agartala for extending the lab facilities and alsoMr. Biswanath Karmakar for his valuable assistance in this research work.

REFERENCES

1. Taya, M. and Arsenault, R. J., 1989, "Metal Matrix Composites, Thermomechanical Behavior," Pergamon Press, NY.
2. P.K. Rohatgi, 1993, "Metal Matrix Composites", Defence Science Journal, Vol 43, No 4, October 1993, pp 323-349.
3. N.V. Nayak, 2014, "Composite Materials in Aerospace Applications", International Journal of Scientific and Research Publications, Volume 4, Issue 9, September 2014.
4. D. L. McDanels et. al., 1986, "Polymer, Metal, and Ceramic Matrix Composites for Advanced Aircraft Engine Applications", American Society for Metals, Vol.8 , No. 1, June 1986.
5. Suraj Rawal, 2001 "Metal-Matrix Composites for Space Applications" The Journal of The Minerals, Metals & Materials Society (TMS), April, 2001
6. Sharma et. al., 2015, "A study on microstructure of aluminium matrix composites", Journal of Asian Ceramic Societies 3 (2015) 240–244.
7. K.R. Padmavathi, Dr. R. Ramakrishnan, 2014, "Tribological behaviour of Aluminium Hybrid Metal Matrix Composite" Procedia Engineering 97 (2014) 660 – 667.
8. H. Kala et. al., 2014, "A Review on Mechanical and Tribological Behaviors of Stir Cast Aluminum Matrix Composites" Procedia Materials Science 6 (2014) 1951 – 1960.

9. M.K.S. Sai, 2016, "Review of Composite Materials and Applications", IJLTET, Vol 6, Issue 3, January 2016.
10. Karl U. Kainer, 2006, "Basics of metal matrix composites" Metal matrix composites: custom-made materials for automotive and aerospace engineering, 21 August, 2006.
11. C. F. Feng, L. Froyen, 2000, "Microstructures of in situ Al/TiB2 MMCs prepared by a casting route", Journal Material Science, February 2000, Volume 35, Issue 4, pp 837–850.
12. Zhu L, et al. (2008) Molecular cloning and responsive expression to injury stimulus of a defender against cell death 1 (DAD1) gene from bay scallops Argopecten irradians. Mol Biol Rep 35(2):125-32
13. Wittig et al., 2008, "Focused grooming networks and stress alleviation in wild female baboons", Hormones and Behavior 54 (2008) 170–177
14. Mileiko et. al., 2017, "Silicide-Molybdenum Fibrous Composites: Fracture Toughness and Creep Resistance" Research Article, Res Rep Metals Vol: 1 Issue: 2

Section 4

Instrumentation and Measurement

29

EEG Signal Analysis Using Brainstorm toward Noninvasive Detection of Epileptic Seizure

Sunil Kumar Choudhary[1,2], Tushar Kanti Bera[1]*

Abstract

Brainstorm is an open-source software tool that is freely available for use in the analysis of multimodal electrophysiological data and source imaging. It is primarily designed for the analysis of data obtained from techniques such as magnetoencephalography (MEG), electroencephalography (EEG), and depth recordings. The Brainstorm software possesses a visually appealing and user-friendly graphical user interface. The utilization of this particular tool enhances the process of acquiring knowledge and enhances efficiency over a broader spectrum of neuroscience. Individuals who possess a limited or negligible understanding of scientific coding and scripting. However, it can also be. Python is commonly employed as a robust scripting tool for executing reproducible and easily distributable batch-processing tasks. The presence of substantial amounts of data. This article provides an overview of the Brainstorm interactive and scripted methodologies. This study aims to elucidate the characteristics by means of visual representation, employing a comprehensive examination of collective data obtained from a sample size of 24 individuals. In a study utilizing electroencephalography (EEG) for visual perception analysis.

Keywords: Brainstorm, electroencephalography (EEG), Epileptic, Detection Seizure,

Introduction

The study of MEG/EEG data and source imaging encompasses a diverse array of methodologies that rely on a broad spectrum of signal processing techniques. The process of forward head modeling involves the mapping of elemental neuronal current sources to scalp potentials and external magnetic fields. This mapping is influenced by the shape and conductivity of the head tissues. Various methods can be employed to perform forward head modeling, including simple spherical head models, overlapping spheres, and boundary or finite element methods [1-3].The examination of Magnetoencephalography (MEG)/EEG data necessitates the transformation of neuropsychology and cognitive neuroscience inquiries into hypotheses pertaining to electrophysiology. Consequently, the development of a systematic procedure for the extraction and analysis of signals necessitates the creation of an analytical workflow, which may incorporate techniques such as source imaging and model estimation [4]. Brainstorm is a software platform that offers a range of tools and solutions designed to cater to the needs of a diverse group of neuroscience researchers [5].

In this study, we focus on two distinct facets of data analysis using the Brainstorm software. The following section provides a comprehensive overview of the interactive processing steps involved in analyzing data from a typical subject. These steps include the preprocessing of raw data, extraction of event-related responses, generation of time-frequency decompositions, and source modeling. Next, we proceed to elucidate the process of extrapolating this analysis to encompass the entire cohort of 16 participants and subsequently deducing inferential statistics at the group level. The replication of the analyses described in this research can be achieved by referring to the newly developed online tutorials, which serve as supplementary resources. New users of Brainstorm will also derive advantages from our extensive introductory courses.

Process of Downloading and Installing Data and Software

The files mentioned in this correspondence can be accessed on openneuro.org. The comprehensive study necessitates a cumulative amount of 400 gigabytes (GB) of accessible storage space. In order to replicate the studies outlined in this study, it is recommended that readers acquire and install Brainstorm6 software.

The interactive environment of Brainstorm can be executed without the need for a Matlab license. Nevertheless, those who do not possess a Matlab license are unable to execute Matlab scripts, thereby impeding their ability to run the automated scripts that replicate the findings outlined in this study. To engage in scripting, it is necessary to have Matlab 2008a or a more recent version.

Automation: Scripting and Reporting of Analysis Pipelines

A practical suggestion for Brainstorm scripting is to divide data analysis pipelines into distinct pieces. For example, the process of importing anatomical data and raw EEG files, performing frequency filtering, estimating power spectrum, and detecting and removing epileptic seizures can be automated without the need for user intervention. These tasks can be executed simultaneously through a unified script. User participation is necessary for several interventions, such as the evaluation of raw files, the identification and confirmation of faulty channels and data segments, and the selection of appropriate SSP or ICA components. Another set of procedures can be executed to segment and average the data, create models of the sources, and extract relevant measurements such as time-frequency decompositions and connectivity metrics. The results of performed scripts are recorded in a log file, which serves the purpose of verifying correct execution and facilitating the process of identifying and resolving any errors or issues. The process of including screenshots in this execution log is accomplished by selecting the "File > Save snapshot" option from the menu.

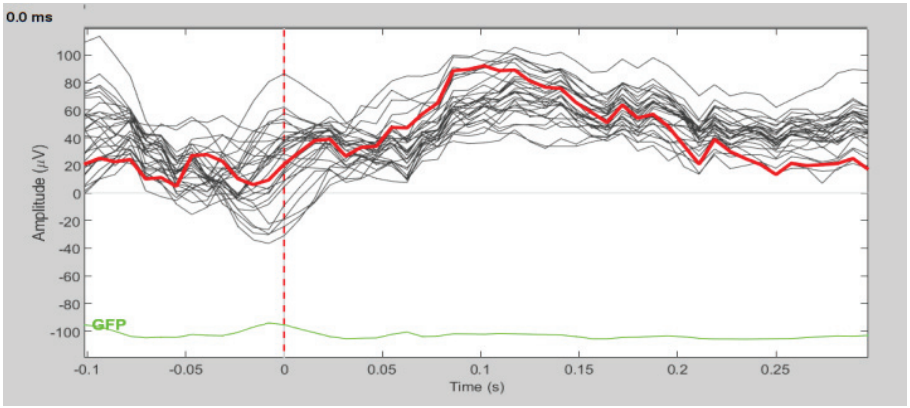

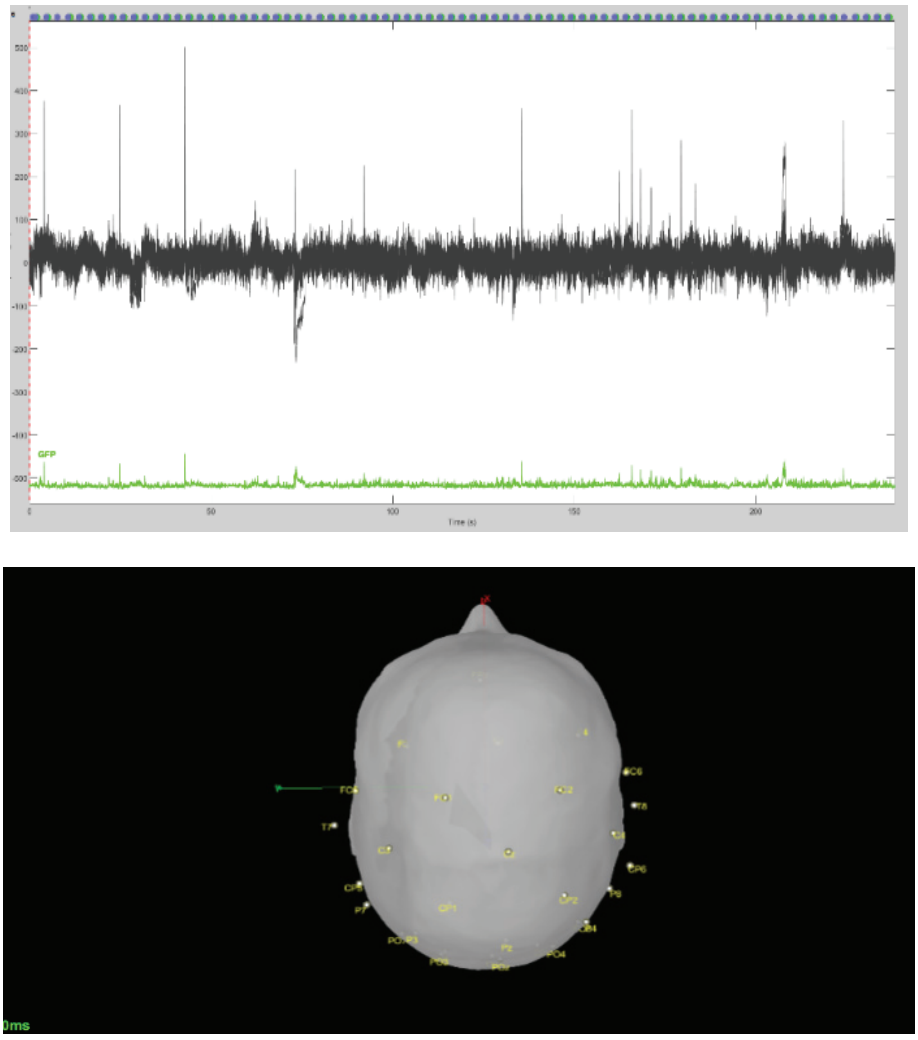

Figure 1. After the successful importation of anatomical EEG data, a screenshot was taken to document the initial brainstorming process.

Conclusion

Brainstorm offers a range of interactive and user-friendly tools that facilitate the creation of automated and standardized processing pipelines. These tools prioritize the implementation of quality control measures and the verification of data integrity. The application provides users with handy tools to visually analyze the results of each step in a data analysis pipeline through execution reports.

REFERENCES

1. Darvas, Felix, et al. "Generic head models for atlas based EEG source analysis." Human brain mapping 27.2 (2006): 129-143.
2. John Nolte, The Human Brain: An Introduction to its Functional Anatomy, Mosby; 6 edition (August 5, 2008).
3. Baillet, Sylvain, and Line Garnero. "A Bayesian approach to introducing anatomy-functional priors in the EEG/MEG inverse problem." IEEE Transactions on Biomedical Engineering 44.5 (1997): 374-385.
4. Baillet, Sylvain. "Magnetoencephalography for brain electrophysiology and imaging." Nature Neuroscience 20.3 (2017): 327-339.
5. Tadel, François, et al. "Brainstorm: a user-friendly application for MEG/EEG analysis." Computational intelligence and neuroscience 2011 (2011): 1-13.

30

Detecting Cardiac Disease with Machine Learning (ML) Technique: A Technical Study with Electrocardiograms (ECG)

Pinaki Ranjan Das, Amiya Samanta and Tushar Kanti Bera

Abstract

Cardiovascular diseases (CVD) represent a significant global health problem that requires prompt and accurate diagnosis. Irregular heartbeats commonly known as Arrhythmia is a serious cardiac condition spread through globally. In this study we tried to predict and categorize arrhythmia as per AAMI EC57 standards. To achieve early detection of heart conditions and better treatment towards patients advance understanding of ECG data is required. A variety of machine learning techniques were utilized and combined to tackle the categorization challenge. Our analysis revealed that the most effective model as Majority Voting Ensemble, boasting an impressive accuracy of 0.897 and specificity of 0.907.

Index Terms: Cardiac Disease, Arrhythmia, Machine Learning, Electrocardiogram (ECG/ EKG), Majority Voting Ensemble, WLAG

INTRODUCTION

The heart is accountable for blood circulation and pressure management

throughout the body. Unfortunately, cardiovascular disease continues to be a primary cause of morbidity and death across the world, owing to factors such as poor nutrition, bad lifestyle choices, substance abuse, and hypertension. This tendency is not limited to India, where these circumstances impose a considerable burden on public health and society overall. While accurate and quick diagnosis is vital, standard clinical techniques can take time and have limits. [1], [2]

Machine learning algorithms can analyze large amounts of medical data such as ECG signals, pictures, patient records, and genetic information. This technology can help healthcare practitioners make more precise diagnoses, hence increasing patient care quality. Machine learning, with its potential for effective and scalable cardiac diagnostics, is a viable strategy for addressing cardiovascular disease. [3]

In this work, we investigated several types of ML algorithms to classify five unique arrhythmias based on AAMI EC57. This study's primary contributions are displayed below.

This study has been done to perform comparative analysis among different ML models.

For prediction, we used logistic regression (LR), K nearest neighbor (KNN), and random forest (RF).

Majority voting ensemble has been applied to collectively use the strength of different ML models.

Further, the Weighted Linear Aggregation Model (WLAG) has been applied for the score level fusion from each independent machine learning (RF, LR, KNN) model's outcome for the extensive study.

The best model has been reported as the out come of this extensive study.

DATASET

The MIT-BIH Arrhythmia Database (mitdb) [4], [5] is comprised of three files: a header file, a binary file, and an annotation file. Each record in the database consists of approximately 650,000 samples. Our analysis focuses on the AAMI EC57 standard 5 micro-categorizations of the database, which include Normal (N), Supraventricular ectopic beat (S), Ventricular ectopic beat (V), Fusion beat (F), and Unknown beat (Q). Only 125-Hz resampled ECG MLII lead data were used in this investigation.

To extract beats from the ECG data, we divided the data into 10-second fragments. The signal amplitude values were standardized between 0 and 1. R peaks were identified by establishing a sufficient threshold value on the normalized value. The R-R time intervals of the signal were determined by locating the window's median. To ensure that all samples had the same length, zeros were added to each selected component. Due to imbalanced data, we unsampled to achieve 20000 samples each. To achieve upsampling, the sampled data point was put back into the original Data Frame after it was selected. For training and testing of the data, the database was divided into 80-20% respectively. This approach was used to reconstruct the academic analysis.

MATERIALS AND METHODS

Our study aims to thoroughly examine five different types of arrhythmia detection and use advanced machine learning (ML) algorithms to categorize these arrhythmias based on the

AAMI EC57 standards. To accomplish this, we investigated several ML prediction models such as logistic regression (LR), k-nearest neighbors (KNN), and random forest (RF). In addition, to integrate the capabilities of various ML models, we used a majority voting ensemble technique and weighted linear aggregation model. We determined the best-performing model in our study after undertaking thorough assessments. The sections that follow give in-depth discussions of our approaches and models.

A. Electrocardiogram (ECG/EKG)

The electrocardiogram (ECG) is an indispensable tool in cardiology that detects and records the electrical activity of the heart over time. This non-invasive technique is widely available and extremely useful for detecting and monitoring cardiovascular problems. Six chest electrodes are put on the skin at specified places to gather electrical impulses from the heart. The resultant ECG waveform contains critical information about how the heart works and is required for recognizing various cardiac diseases. The P-wave (atrial depolarization), QRS complex (ventricular depolarization), T-wave (ventricular repolarization), and ST segment (interval between depolarization and repolarization) compose the conventional ECG waveform. Irregular heartbeats are known as arrhythmias, and ventricular arrhythmias can be fatal.

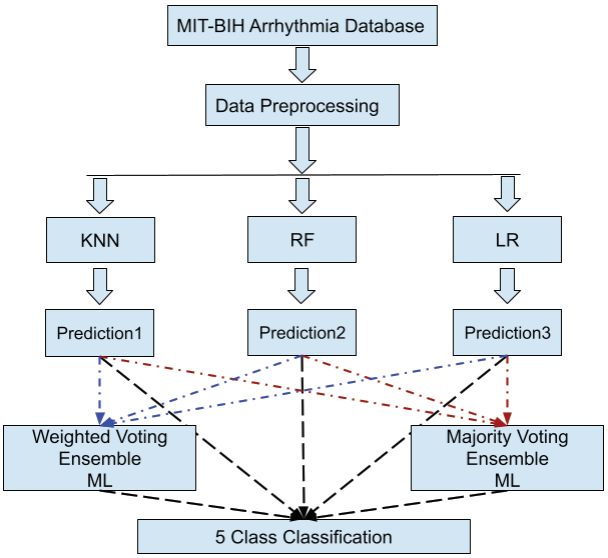

Fig. 1. Flow diagram of Arrhythmia classification study

B. Cardiac Disease Detection from ECG Data using ML

Machine learning algorithms are widely used to analyze ECG data for diagnosing cardiac illnesses. Accuracy is often superior to previous methods. Activities required for diagnosis include data collection, processing, and feature extraction. Large, labeled datasets are needed, and algorithms must be robust to noise and artifacts. The goal is interpreting ECG data in the context of a patient's medical history. [6], [7]

1. *Logistic regression (LR):* Logistic regression is widely used for binary and multi-class classification. It's used in ECG signal processing to estimate model parameters and determine decision boundaries. [8] The model is trained using labeled ECG data and optimization techniques. It's great for ECG analysis when linear correlations between variables and classes are significant. Scikit-learn's logistic regression model with 'multinomial' multi-class classification and the 'lbfgs' solver was used in our study.
2. *K-Nearest Neighbors (KNN):* KNN is an intuitive machine learning technique for classification and regression. It is non-parametric and requires no assumptions about the data distribution. [9] By evaluating feature vectors in ECG signals with a distance metric like Euclidean

distance, it determines the similarity of comparable patterns. The hyperparameter K, which specifies the number of nearest neighbors to include, is an important factor here.

3. *Random Forest (RF):* Random Forest is an ensemble learning approach for classification and regression in machine learning that is good at managing complex datasets. It is widely employed in ECG signal processing classification to categorize ECG signals into distinct groups or conditions. Random Forest's ensemble of decision trees enables noise tolerance and the capacity to record complicated data linkages, resulting in a better grasp of feature significance. This aids in identifying the most important ECG signal characteristics for categorization and gives insight into the clinical importance of distinct ECG aspects. Random Forest can also help with class imbalance issues in ECG signal processing. [10] Overall, Random Forest is a great technique for effectively classifying ECG data.

C. Majority Voting Ensemble

A prominent machine learning approach is the Majority Voting Ensemble, which involves integrating numerous models to create a collective forecast. The algorithm is determined by the majority decision of all the individual predictions made by each model in the ensemble. [11], [12] This approach is commonly used in ensemble learning tasks because it leverages the diverse perspectives of multiple models to arrive at a more accurate prediction by improving overall predictive accuracy and reducing overfitting.

D. Weighted Linear Aggregation Model

The Weighted Linear Aggregation (WLAG) method employs a weight assignment mechanism to allocate weights to different collective algorithms based on their effectiveness in achieving the user's desired goal. It is imperative to ensure that the sum of the weights assigned to various sections equals one. [13] We used score level fusion to combine RF, LR, and KNN models. Weighted linear aggregation with weights 0.4, 0.3, and 0.3 was used to generate the model. After analyzing the results on a validation set, we assigned a higher weight (0.4) to RF model as it is providing best accuracy value.

E. Method

We analyzed the mitdb data and put it through ML algorithms with

various parameter tweaks to find the best effective technique for identifying five distinct arrhythmias. We examined the results of each algorithm and chose the one that performed best with the available data, resulting in considerable gains in accuracy, recall, and specificity. These approaches enabled us to identify arrhythmias more efficiently, offering a perfect setup for further study.

Table I: Result with all models

	RF	LR	KNN	Weighted	WLAG
Accuracy	0.894	0.845	0.815	0.856	*0.897*
Recall	0.635	0.693	0.605	0.652	0.686
Specificity	0.889	0.9	0.881	0.889	*0.907*

RESULTS

A random forest model was used in a multi-class classification experiment to evaluate the effect of the n-estimator parameter on its performance. The number of trees utilized in the model is specified by this parameter. The findings showed that the ideal n-estimator number for the random forest model is 55, based on the assessment criteria of accuracy, recall, and specificity. The model earned remarkable accuracy, recall, and specificity scores of 0.894, 0.635, and 0.889 at this level. In addition, for prediction purposes, Logistic Regression (LR) and K Nearest Neighbor (KNN) were used as distinct machine learning models. LR had accuracy, recall, and specificity ratings of 0.845, 0.693, and 0.9, respectively, whereas KNN had 0.815, 0.605, and 0.881. A Majority Voting Ensemble and Weighted Linear Aggregation Model was employed using machine learning models such as LR, KNN, and RF algorithms. The Majority Voting Ensemble produced scores of 0.897, 0.686, and 0.907, respectively, while the WLAG yielded scores of 0.856, 0.652, and 0.889. After evaluating three different ML algorithms, it was determined that RF had the highest accuracy score of 0.894, while LR exhibited the best recall and specificity scores of 0.693 and 0.9, respectively.

DISCUSSION

After evaluating various models, the Majority Voting Ensemble emerged as the top performer in terms of accuracy and specificity. While it trailed the LR model by only 1.01% in recall value, relying too heavily on a single model can result in suboptimal performance. The efficacy of different performance metrics

varies depending on the specific model, such as RF. Therefore, prioritizing an underperforming metric like REC could negatively impact the entire aggregation model and lead to overall underperformance. Overall, this study recommends using the Majority Voting Ensemble as a promising method for achieving exceptional results in multi-class classification tasks.

CONCLUSION

In our research, most notably, the model was only implemented using the imbalance dataset mitdb. Future studies will include the integration of more datasets to acquire a more thorough knowledge of prediction performance.

REFERENCES

1. C. A. Morillo, A. Banerjee, P. Perel, D. Wood, and X. Jouven, "Atrial fibrillation: the current epidemic," *Journal of geriatric cardiology: JGC*, vol. 14, no. 3, p. 195, 2017.
2. R. Gupta, I. Mohan, and J. Narula, "Trends in coronary heart disease epidemiology in india," *Annals of global health*, vol. 82, no. 2, pp. 307– 315, 2016.
3. M. Kachuee, S. Fazeli, and M. Sarrafzadeh, "Ecg heartbeat classification: A deep transferable representation," in *2018 IEEE international conference on healthcare informatics (ICHI)*. IEEE, 2018, pp. 443– 444.
4. A. L. Goldberger, L. A. Amaral, L. Glass, J. M. Hausdorff, P. C. Ivanov, R. G. Mark, J. E. Mietus, G. B. Moody, C.-K. Peng, and H. E. Stanley, "Physiobank, physiotoolkit, and physionet: components of a new research resource for complex physiologic signals," *circulation*, vol. 101, no. 23, pp. e215–e220, 2000.
5. G. B. Moody and R. G. Mark, "The impact of the mit-bih arrhythmia database," *IEEE engineering in medicine and biology magazine*, vol. 20, no. 3, pp. 45–50, 2001.
6. A. Rath, D. Mishra, G. Panda, and S. C. Satapathy, "Heart disease detection using deep learning methods from imbalanced ecg samples," *Biomedical Signal Processing and Control*, vol. 68, p. 102820, 2021.
7. M. M. Ahsan and Z. Siddique, "Machine learning-based heart disease diagnosis: A systematic literature review," *Artificial Intelligence in Medicine*, vol. 128, p. 102289, 2022.
8. F. A. Latifah, I. Slamet, and S. Sugiyanto, "Comparison of heart disease classification with logistic regression algorithm and random forest algorithm," in *AIP Conference Proceedings*, vol. 2296, no. 1. AIP Publishing, 2020.
9. I. K. A. Enriko, M. Suryanegara, and D. Gunawan, "Heart disease diagnosis system with k-nearest neighbors method using real clinical medical records," in *Proceedings*

of the 4th international conference on frontiers of educational technologies, 2018, pp. 127–131.

10. R. G. Kumar, Y. Kumaraswamy, *et al.*, "Investigating cardiac arrhythmia in ecg using random forest classification," *Int. J. Comput. Appl*, vol. 37, no. 4, pp. 31–34, 2012.
11. P. Pławiak and U. R. Acharya, "Novel deep genetic ensemble of classifiers for arrhythmia detection using ecg signals," *Neural Computing and Applications*, vol. 32, no. 15, pp. 11137–11161, 2020.
12. A. Rath, D. Mishra, and G. Panda, "Imbalanced ecg signal-based heart disease classification using ensemble machine learning technique," *Frontiers in Big Data*, vol. 5, p. 1021518, 2022.
13. D. Sun, M. Wang, and A. Li, "A multimodal deep neural network for human breast cancer prognosis prediction by integrating multidimensional data," *IEEE/ACM transactions on computational biology and bioinformatics*, vol. 16, no. 3, pp. 841–850, 2018.

31

Early Detection of Landslides Using Wireless Sensor Networks: A Focus on Geological Factors

Rituparna Bhattacharya and Mitra Barun Sarkar

Abstract

Landslides pose a significant threat to both human lives and infrastructure, necessitating the development of effective early warning systems. Wireless Sensor Networks (WSNs) have emerged as a promising solution for real-time monitoring and early detection of landslides. This review paper focuses on the utilization of WSNs to detect landslides in relation to geological factors. The paper examines recent advancements in sensor technology, data processing techniques, and modeling approaches to enhance the accuracy and timeliness of landslide detection. The integration of geological factors in these systems further improves their reliability and effectiveness.

Keywords: Sensors, Tropology, Inclinometers, GPS modules, Fault lines, Slope morphology.

Introduction

The early detection of landslides has emerged as a critical area of research and technological innovation, aiming to mitigate the devastating consequences

of these natural disasters. In recent years, wireless sensor networks (WSNs) have taken center stage in this endeavor, revolutionizing the way we monitor geological factors that contribute to landslides. This review delves into the captivating realm of "Early Detection of Landslides using Wireless Sensor Networks," with a particular emphasis on the pivotal role played by geological factors in this groundbreaking field.

Landslides, characterized by the abrupt and destructive movement of soil and rock down a slope, pose significant threats to both human lives and infrastructure. As climate change intensifies, the incidence and severity of landslides are on the rise, underscoring the urgency of developing robust early warning systems. In this context, the integration of wireless sensor networks with the geological domain offers a transformative approach, promising real-time monitoring and early detection capabilities that were once only dreamt of.

This review embarks on a comprehensive exploration of the integration of wireless sensor networks with geological factors to detect landslides. It will uncover the underlying principles, sensor technologies, data analysis methods, and practical applications that are reshaping our ability to foresee and respond to landslide events. Through this journey, we will delve into the intricate synergy between modern sensor technology and the earth sciences, shedding light on how these developments are shaping the future of landslide hazard management.

Geological Factors in Landslide Detection

Soil Composition and Stability:

The paper discusses how the geological characteristics of soil, such as its composition, permeability, and cohesion, influence the likelihood of landslides. WSNs can deploy various sensors to measure soil moisture, pressure, and stability indicators, aiding in the identification of potential landslide-prone areas.

Slope Morphology and Gradient:

The topography and slope gradient significantly affect landslide occurrence. WSNs equipped with inclinometers and GPS modules can monitor changes in slope angles, providing valuable insights into slope stability and potential landslide triggers.

Geological Structures and Fault Lines:

Geological structures, such as fault lines and rock formations, impact the spatial distribution of landslides. Integrating seismic sensors into WSNs enables the detection of ground vibrations and shifts associated with geological activities, enhancing the accuracy of early warning systems.

Sensor Technologies

Accelerometers and Gyroscopes:

These sensors are used to detect ground vibrations, slope movements, and changes in terrain. The paper discusses their integration within WSNs and their role in detecting subtle shifts that might precede a landslide.

Soil Moisture and Pressure Sensors:

By measuring soil moisture content and pressure changes, these sensors offer insights into potential soil instability. The review covers their applications in landslide-prone regions.

Seismic Sensors:

Seismic sensors are essential for detecting ground movements caused by geological factors, including fault line activities. Their incorporation into WSNs enhances the overall detection accuracy.

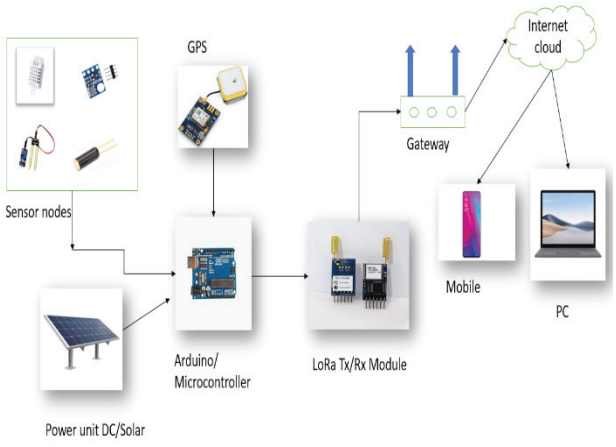

Fig 1: Landslide detection system architecture

Data Processing and Modeling

Data Fusion and Integration:

The paper addresses the challenges of handling heterogeneous data from multiple sensors in a WSN. It explores techniques for data fusion and integration to create a comprehensive view of the monitored area's stability.

Machine Learning and Predictive Modeling:

Utilizing machine learning algorithms and predictive modeling, WSNs can analyze historical data to identify patterns and anomalies indicative of imminent landslides. The review highlights various algorithms suitable for this purpose.

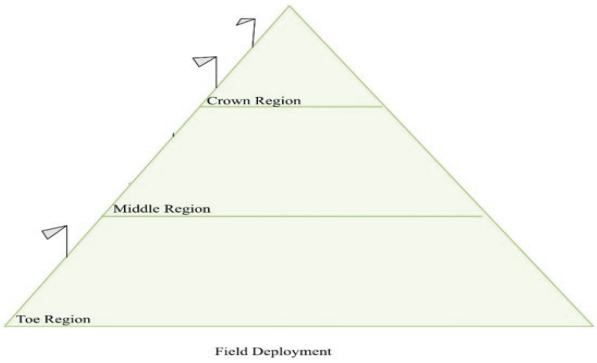

Fig 2: Field Deployment Of Sensor Nodes

Case Studies

The review provides examples of successful WSN deployments for landslide detection in different geological settings. It discusses how these deployments effectively incorporated geological factors to enhance accuracy and reduce false alarms.

Challenges and Future Directions

The paper concludes by outlining challenges such as sensor calibration, energy efficiency, and network robustness. It also proposes future research directions, including the integration of remote sensing data and the development of autonomous sensor networks.

Conclusion

Wireless Sensor Networks offer a powerful solution for early landslide detection by leveraging geological factors. By incorporating insights from soil composition, slope morphology, and geological structures, these systems can provide accurate and timely warnings, ultimately saving lives and reducing damage. Continued research and technological advancements will further enhance the reliability and effectiveness of WSN-based landslide detection systems.

REFERENCES

1. G. N. L. R. Teja, V. K. R. Harish, D. Nayeem Muddin Khan, R. B. Krishna, R. Singh and S.Chaudhary, "Land Slide detection and monitoring system using wireless sensor networks (WSN)," 2014 IEEE International Advance Computing Conference (IACC), Gurgaon, India, 2014, pp. 149-154, doi: 10.1109/IAdCC.2014.6779310.
2. SS, Vinod Chandra, and E. Shaji. "Landslide identification using machine learning techniques: Review, motivation, and future prospects." Earth Science Informatics (2022): 1- 28.
3. Reethika, A., et al. "Automatic sensor network analysis for the landslide detection system." Journal of Physics: Conference Series. Vol. 1916. No. 1. IOP Publishing, 2021.
4. Susanto, Erwin, et al. "Slope, humidity and vibration sensors performance for landslide monitoring system." 2019 IEEE Asia Pacific Conference on Wireless and Mobile (APWiMob). IEEE, 2019.

32

Strengthening Weak Clay Soil through the Incorporation of Plastic Strips

Sanku Konai, Sushmita Kumari, Gaurav Kumar, Anand Raj

Abstract

Plastics offer many conveniences, but because of the throw away habit, a single plastic contributes 40% of the plastic waste which is produced every other year. Many plastic products, such as plastic bottles, bags and food wrapping materials exist in the environment for several years. Therefore, to decrease the ecological hazard, a proper way should be found to dispose the plastic waste. Plastic pollution has now become the most critical environmental issue, as production of disposable plastic products is increasing rapidly. From the previous research it was seen that plastic material can be use as soil stabilizer for improving the strength of the weak soil. Construction on weak soil is a serious concern for geotechnical engineers as it cannot provide adequate load carrying capacity. To increase the strength characteristics of soil, many stabilization methods have been discovered so far with various stabilizing agents. Out of all stabilizers, plastic as stabilizer can be one of the economical ways to stabilize the weak soils. In the present study, the main objectives are to investigate engineering properties of the weak soil mixed with polypropylene plastic strips as a soil stabilizerand its effect on the soil strength by performing CBR tests. Different percentages of polypropylene plastic strips such as 0.5%, 1.0%, and 2.0% by the weight of the dry soil were properly mixed with weak clay soil and laboratory

investigations were performed. A huge increase in CBR value was observed when polypropylene plastic strips were added to the weak clay soil.

Keywords: Strength Improvement, Plastic strips, CBR tests, Clay soil, Polypropylene

Introduction

Plastic products have become a fundamental part of our everyday lives. Globally, the production of plastic exceeds 150 million tons annually. According to a survey by the Central Pollution Control Board (CPCB) in India, reported by Times of India on April 30, 2015, it was estimated that 60 cities in India generate approximately 15,342.6 tons of plastic waste daily [10]. This amounts to roughly 5.6 million tons per year. However, more than 6000 tons of this waste remain uncollected and scattered. There is a pressing need for the proper disposal of these waste products. One innovative and cost-effective method of recycling these materials is to use them as reinforcing agents to enhance the strength of weak soils. This approach not only recycles the waste but also serves a practical purpose.

The design of structures in weak soil requires geotechnical engineering to improve the ground conditions. Before starting any development or construction work for civil purposes, it is important to determine the soil type and the strength needed to support the structural loads.

Soil Stabilization is a way of improving the engineering properties of soils. Stabilization increases strength, decreases permeability & compressibility of soil. It is done either by compaction or by adding admixtures like lime, cement etc. Soil stabilization can be performed by several methods.

1. Mechanical stabilization: -Mechanical stabilization involves vibration or compaction. This process alters the physical state of soil particles.
2. Chemical stabilization: - In this stabilization method a chemical stabilizer is used which causes chemical reaction between soil and stabilizer.

According to previous research work, it is seen that embankments and road pavement layers can be improved by soil stabilization with plastic waste, which results in increased soil strength. Interesting results are observed when the soil is stabilized with plastic waste, as evidenced by the increase in soil strength characteristics measured in various tests [1,2]. The size and shape of plastic waste particles have an influence on the strength of soil [3]. Maximum dry density of fibre mix stone dust increases with increase in fibre content and

Optimum moisture content decreases with addition of plastic fibres. Mixing fibre can also increase the strength of stone dust[4].

Recently, there has been a growing interest among researchers in exploring soil stabilization techniques using polymers or waste materials, such as polythene bags and discarded plastic bottles. An assessment has been conducted on waste marble dust, revealing that it significantly enhances the physical characteristics of the soil [5].The soil's strength and engineering properties were enhanced by the addition of fibre reinforcement. The optimal percentage of plastic fibre was found to be between 0 and 5%. This addition resulted in an increased CBR value [6].

However, previous studies have shown that the results differ with different type of soil and some strength values may change with waste plastic stabilization as the effect in the soil strength properties is different with the type of waste plastic fibres, strips or flakes show different interaction behaviour. The CBR values increase until the optimum percentage of plastic waste.

Many stabilizations method have been discovered so far, but some of the stabilizers are not economical. In this experimental analysis to assess the effectiveness plastic strips as a soil stabilizer, a series of heavy compaction tests were conducted. These tests were performed on clay soil samples, which were mixed with varying percentages of polypropylene plastic strips. The percentages used were 0%, 0.5%, 1.0%, and 2.0%, each calculated based on the dry weight of the soil sample.

EXPERIMENTAL ANALYSIS

Weak clay soil having poor strength was used for the present study. Soil sample for present experimental study are collected from nearby area of Balangir from Orissa, India. Various laboratory tests were conducted to obtain geotechnical properties of the soil samples. Properties of soil samples are presented in Table 1. Maximum dry density of soil sample from Light compaction test and Heavy Compaction tests were 1.77 gm/cc (18.5% OMC) and 1.96 gm/cc (13.5% OMC) respectively. Polypropylene plastic strips (PP) were used as reinforcing materials and mixed with soils to increase the strength. Polypropylene (PP) is the thermoplastic polymers. It is made from several combinations of the propylene monomers. Properties of Polypropylene strips (PP) are presented in Table 2.

Table 1: Geotechnical properties of soil sample

Properties	Value
Specific gravity	2.63
Free swell index (%)	46

Liquid limit (%)	55
Plastic limit (%)	29
Plasticity index	26
Shrinkage limit (%)	11

Table 2: Geotechnical properties of Polypropylene

Engineering property	**Value**
Chemical formula	[C3H6] n
Melting temperature(oC)	130
Tensile strength (MPa)	32
Flexural strength (MPa)	41
Specific gravity	0.91
Acid and alkali resistance	Very good
Average length	12 mm

A series of CBR tests were conducted in the laboratory on soil mixed with Polypropylene plastic strips and results were obtained. To perform the CBR tests on soil samples, it was first oven dried for 24 hours and then pulverized and passed through the required sieve. Then, the soil sample is mixed thoroughly with different percentages i.e. (0%, 0.5%, 1.0%, and 2.0% by the weight of the dry soil sample) of plastic strips. Soil samples are then compacted using heavy compaction method. Test results were obtained and analysed to know its suitability to be used as soil stabilizer and effects of the plastics strips on strength properties of soils.

Results and Discussion

Unsoaked CBR tests were performed in laboratory on soil mixed with 0%, 0.5%, 1.0%, and 2.0% Polypropylene plastic strips. For each combination of soil mix, maximum dry density (MDD) at optimum moisture content was obtained in laboratory. By considering OMC for each soil mixed, soil samples were prepared for all CBR tests. Soil mixes are compacted in 5 layers with 56 number of blows for each layer. Then the results are recorded for 2.5 mm and 5mm penetrations. Figure 1 shows the nature of load vs settlement curve for Soil mixed with 0%, 0.5%, 1.0%, and 2.0% plastic strips. It can be observed from Figure 2 that as the percentage of plastic strips were increased, the load capacity of soil samples was increased. Figure 2 is showing the percentage increment in CBR value for different soil mixes. CBR value obtained for soil mixed with 0%, 0.5%, 1.0%, and 2.0% plastic strips were 1.8%, 5.46%, 7.4% and 8.35 respectively (Figure 2). It is observed from Figure 1 and Figure 2 that adding

plastic strips in soil showed significant increase in strength. This may be due to the resistance against penetration, contributed by the interaction between soil particles and plastic fibres.

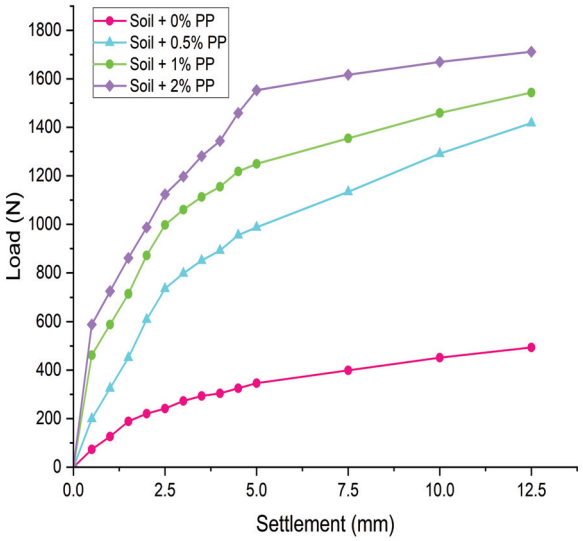

Figure-1: Load vs Settlement curve for Soil mixed with 0%, 0.5%, 1.0%, and 2.0% plastic strips.

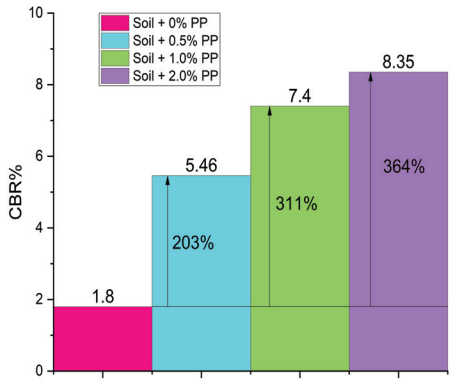

Figure-2: Percentage increment in CBR value for soil mixed with 0%, 0.5%, 1.0%, and 2.0% plastic strips.

Conclusions

A series of CBR tests were conducted on clay soil mixed with 0%, 0.5%, 1.0%, and 2.0% Polypropylene plastic strips and following conclusions are obtained.

As the proportion of plastic strips in the soil sample was increased, there was a corresponding increase in the CBR value. Specifically, the CBR value rose from 1.80% to 8.35% for a 2.5 mm penetration when 2% PP strip was mixed in.

The CBR test is often viewed as an indirect method of testing strength. The addition of plastic strips to the soil has been observed to significantly enhance this strength. This enhancement is likely due to the increased resistance to penetration, which is a result of the interaction between the soil particles and the plastic fibres.

It's noteworthy that when soil is appropriately mixed with plastic strips, it can effectively serve as a soil stabilizer. This not only enhances the strength of soil but also is cost-effective.

Form the present study, it was seen that using Polypropylene plastic strips can be used as an economical soil stabilizer. However, conclusions were made from the present research work were based on experiments with one type of soil and plastic strips. More experiments are required to make generalized conclusions.

REFERENCES

1. Choudhary A.K., Jha J.N., and Gill K.S, A Study on CBR Behaviour of Waste Plastic Strip Reinforced Soil. Emirates Journal of Engineering Research. 15(2010), 51-57.
2. Nagle R., Jain R., and Shinghi A, Comparative Study of CBR of Soil, Reinforced with Natural Waste Plastic Material. International Journal of Engineering & Science Research, 4(2014),304-308.
3. Peddaiah S., Burman A., and Sreedeep S, Experimental Study on Effect of Waste Plastic Bottle Strips in Soil Improvement. Geotechnical and Geological Engineering, vol. 36(2018),2907-2920.
4. Mahali K P., Sinha A K, Utilization of stone dust with plastic waste for improving the subgrade in highway pavement construction International Journal of Research in Engineering and Technology,4, 29-35.
5. Waheed A., Arshid M., Khalid R.A, Soil Improvement Using Waste Marble Dust for Sustainable development. Civ. Eng. J. 2021, 7, 1594–1607.
6. Iravanian A.; Haider A.B, Soil Stabilization Using Waste Plastic Bottles Fibers: A

Review Paper. IOP Conf. Series Earth Environ. Sci. 2020, 614.

7. Fauzi A,Soil engineering properties improvement by Utilization of cut waste plastic and crushed waste glass as additive, Int. J. of engineering and Technology,8,15-18, 2016.
8. Arpitha G, Soil Stabilization by using Plastic Waste, ICETETSM-17, ISBM-978-93-867-71-54-2 (2017).
9. Dhatrak A. I., Konmare S.D,Performance of randomly oriented plastic waste in flexible pavement, Int. J. of pure and applied research in Engineering and Technology,FI3,193-202, 2015.
10. Times of India, article on April 30, 2015, http://timesofindia.indiatimes.com/home/environment/pollution/60-citiesgenerate-over-15000-tonnes-of-plastic-waste-per day/article show/47110633.cms

33

Enhancing Concrete Strength through partial substitution of Conventional Materials with Marble Powder, Crushed Marble, and Over-Burnt Bricks

Md. Hamjala Alam, Koyndrik Bhattacharjee, Arijit Kumar Banerji, Chanchal Das and Satabdi Saha[2]

Abstract

Due to modern innovations and developments in the construction industry, the use of natural aggregate is on the rise, and at the same time, solid waste production from the demolition of buildings is on the rise. It is for these reasons that the reuse of demolished constructional waste, such as over-burnt bricks, marble powder and crushed marble, has become a viable option for reducing both solid waste and the shortage of natural aggregates for making concrete. This research investigates the potential enhancement of concrete strength through the partial substitution of conventional constituents, namely cement, sand, and coarse aggregate, with environmentally friendly alternatives. Marble powder, derived from the waste of the marble industry, crushed marble and over-burnt bricks, known for their pozzolanic properties, were used as supplementary materials. The concrete prepared with these alternate products was tested for workability and strength. Experimental results reveal that the incorporation

of these sustainable alternatives not only reduces the environmental impact of concrete production but also positively influences its mechanical properties. It was also observed that the properties of the concrete in a fresh and hardened state were impressive, although the results varied drastically from the original properties with the conventional materials. The findings highlight the potential for more resource-efficient and durable concrete mix designs, contributing to the broader goals of sustainable and eco-friendly construction.

Keywords: concrete strength, natural aggregates, over-burnt bricks, marble powder, crushed marble

Introduction

The construction industry is in continual work for innovative and sustainable solutions to address the challenges of urbanization, resource scarcity, and environmental impact. In this context, concrete, as the foundation of modern construction, is undergoing a transformation towards greater sustainability. Concrete is a widely used construction material composed of a mixture of cement, water, fine aggregates (such as sand), and coarse aggregates (such as gravel or crushed stone). When these components are combined and allowed to cure, they form a solid and durable material that is widely used in the construction industry for various applications. Concrete possesses a wide range of properties that make it a popular and versatile construction material. The properties of concrete can be influenced by the mix design, the quality of materials used, curing conditions, and other factors [1]. Concrete gains strength through a chemical reaction called hydration. When water is mixed with cement, a series of complex chemical reactions occur, leading to the formation of a hardened cementitious matrix. This process is what gives concrete its strength and durability over time. Proper consideration of these properties is essential during the design and construction of concrete structures to ensure their safety, longevity, and performance.

Concrete is an incredibly versatile construction material, and its uses are widespread in various sectors of the construction industry. Concrete is extensively used in constructing residential buildings, commercial structures, high-rise buildings, bridges, constructing roads, highways, airport runways, construction of dams, reservoirs, canals, and other water-related structures. The excellent compressive strength and ability to form durable linings make concrete a preferred material for constructing tunnels and underground structures. Concrete is often used to build retaining walls that prevent soil

erosion and provide structural support for slopes and embankments. Pre-stressed and post-tensioned concrete is used in bridges, beams, and other structures to enhance their load-carrying capacity and reduce cracking. In coastal areas, concrete is used to construct seawalls and other structures to protect against erosion and flooding. Concrete is popular and widely used in the construction industry for several reasons, including its unique combination of properties and advantages over other construction materials [2]. Concrete production heavily relies on finite natural resources, and its carbon footprint is a significant concern in contemporary construction [3]. By harnessing the properties of waste materials like marble powder, crushed marble, and over-burnt bricks as partial replacements, we can potentially reduce the demand for raw materials and minimize the environmental consequences associated with concrete production. Moreover, such substitutions offer the prospect of not only enhancing concrete performance but also addressing issues related to the disposal of these waste materials.

Marble, a highly regarded material in the architectural world, has gained attention for its potential as a supplementary material in concrete production. A huge quantity of dust is produced during the cutting process of marble. About 25% of the original mass of marble is rendered into dust in the process of cutting [4]. Crushed marble is a natural stone aggregate produced by crushing marble rocks into smaller fragments. Also from the demolition of marble structures, smaller crushed marbles are obtained. Crushed marble can be used as an aggregate in concrete mixes, contributing to the overall strength and appearance of the concrete. Crushed marble exhibits properties conducive to concrete production, such as excellent compressive strength and durability [4]. The irregular shapes of crushed marble particles create interlocking effects within the concrete matrix, enhancing its strength characteristics. Research suggests that using crushed marble in concrete mixes can lead to improved mechanical properties, making it a sustainable alternative to traditional coarse aggregates [4-6]. Moreover, marble powder, a byproduct of the marble industry, is increasingly recognized for its pozzolanic properties. Researchers have explored its use as a partial replacement for cement in concrete mixes [7-9]. The fine particles of marble powder react with calcium hydroxide in the cement matrix to form additional binding materials. This pozzolanic reaction contributes to improved compressive strength, reduced permeability, and enhanced durability in concrete [8]. Several studies have demonstrated the positive effects of incorporating marble powder in concrete, particularly in terms of increasing strength and reducing the carbon footprint of cement production [7-9]. In addition, over-

burnt bricks, also known as clinker bricks are a type of brick that has been subjected to excessive heat during the firing process in the kiln. This intense heat causes the clay to become vitrified, resulting in a darker colour and a distinct appearance. Over-burnt bricks are typically darker shades of red or brown and may have a rough, irregular surface texture. These bricks can be used for partial replacement of coarse aggregates as they also possess strength and density. These bricks, subjected to high temperatures during production, possess remarkable compressive strength and durability properties. Integrating over burnt bricks into concrete mixes has shown promise in enhancing concrete strength and promoting sustainability by reducing waste in the brick industry [10, 11].

From a review of the literature, composite cement displayed better strength at 28 days compared to 7 days, indicating a higher intensity of the material. The increased strength is attributed to the higher marble content, which also correlates with the amount of dust present in the marble. Consequently, the concrete incorporates marble dust, leading to reduced natural resource consumption and a positive impact on mitigating pollution and environmental harm [7-9]. Several researchers have worked on the idea of replacing fine aggregate in concrete with manufactured sand, crushed marble, and crushed basalt. The results have clearly demonstrated that the fine aggregates could be replaced up to a good percentage with these materials which, in other aspects are solid wastes, and the requisite properties and results are also obtained [10]. In a study, Ahmadi et al. [12] explored the use of waste from marble mining byproducts in structural concrete. Substituting marble waste with sand improved compressive and flexural strength. Increased replacement of recycled aggregates improved impact resistance, although no distinct water absorption trend was identified. Overall, research in this field emphasizes the potential advantages of these substitutions in terms of mechanical properties, durability, and environmental impact. However, further investigation and standardization are necessary to fully realize their potential and promote sustainable practices in the concrete industry. This paper explores a novel approach to enhance concrete strength by partially substituting conventional cement, sand, and coarse aggregate with marble powder, crushed marble, and over-burnt bricks. Through a series of experimental analyses and performance assessments, we aim to provide valuable insights into the feasibility of adopting these alternative materials for concrete production.

Materials

Coarse Aggregates and Sand

Coarse aggregates provide the bulk and stability to concrete mixes, enhancing their mechanical properties. The selection of coarse aggregates depends on factors like desired strength, durability, and workability.Sand is a crucial component in concrete mixes, serving as the fine aggregate that fills the voids between larger particles like gravel and contributes to the workability and cohesiveness of the mixture. The quality and characteristics of sand greatly influence the concrete's properties, such as compressive strength, durability, and finishing. The coarse aggregates (Fig. 1a) were obtained from the Pachami stone quarry in Birbhum, West Bengal; and the sand was obtained from Joydev, West Bengal. Table 1 shows the physical parameters of coarse aggregates and sand.

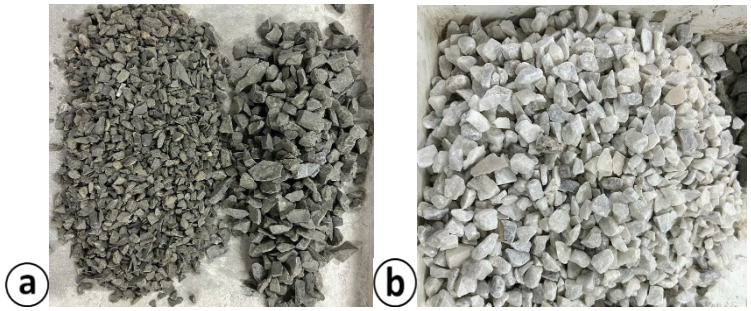

Figure-1: a) Coarse aggregate, b) Crushed marble

Table 1: Physical properties of coarse aggregates and sand

Parameter	Test Result of Coarse Aggregate	Test Result of Sand
Specific gravity	2.42	2.66
Bulk Density (kg/m^3)	1591	1480
Water Absorption (%)	1.29	3.62
Crushing Value (%)	22.60	NA
Impact Value (%)	14.10	NA
Fineness Modulus	NA	2.67

Cement

The cement utilised in this study is ordinary Portland cement of Grade 53.

OPC 53-grade cement (Fig. 2a) is known for its high compressive strength, making it an ideal choice for applications where structural stability is vital. Its superior strength attributes contribute to the durability and load-bearing capacity of concrete structures. Its properties is shown in Table 2.

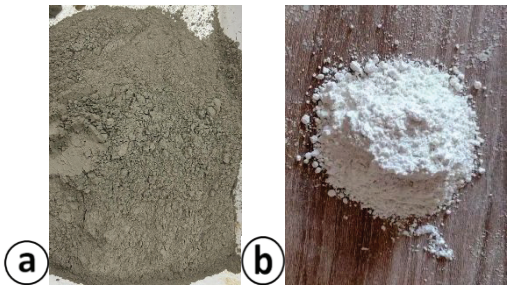

Figure-2: a) Cement, b) Marble powder

Table 2: Physical properties of cement

Parameter	Test Result
Specific gravity	3.08
Density (kg/m^3)	1591
Soundness (mm)	2
Fineness (%)	2
Initial Setting Time (minutes)	110
Final Setting Time (minutes)	240
Consistency (%)	33

Crushed Marble and Marble Powder

Crushed marble refers to marble stone that has been mechanically crushed or broken into smaller pieces. Crushed marble (Fig. 1b), when used as a partial replacement for conventional coarse aggregates in concrete, contributes to improved workability. Its angular and irregular particle shape creates a more interconnected matrix, enhancing the concrete's plasticity and making it easier to place and finish during construction. Marble powder (Fig. 2b) is a fine, dry substance that results from the process of grinding or pulverizing marble into a fine dust or powder. It is obtained as a byproduct during various marble processing operations, such as cutting, polishing, or shaping marble. Marble powder exhibits pozzolanic properties when used as a partial replacement for cement in concrete. This pozzolanic activity contributes to enhanced binding

and the development of secondary cementitious compounds, resulting in improved compressive strength and durability.Table 3 shows the physical parameters of crushed marble and marble powder.

Table 3: Physical properties of crushed marble and marble powder

Parameter	Test Result of Crushed Marble	Test Result of Marble Powder
Specific gravity	2.20	2.53
Water Absorption (%)	1.06	0.97
Crushing Value (%)	27.67	NA
Impact Value (%)	17.56	NA
Colour	White	White

Over-Burnt Bricks

Over-burnt bricks are a distinctive type of brick used in the construction industry, known for their unique characteristics resulting from exposure to extremely high temperatures during the firing process. This intense heat treatment alters their physical and chemical properties, resulting in a harder and more durable material compared to regular bricks. Over-burnt bricks (Fig. 3) exhibit a dark, often blackened appearance due to the extreme heat they endure. Table 4 shows the physical parameters of over-burnt bricks.

Figure-3: Appearance of Over-burnt bricks

Table 4: Physical properties of over-burnt bricks

Parameter	Test Result
Specific gravity	2.67
Water Absorption (%)	10.08
Crushing Value (%)	31.2
Impact Value (%)	20.45
Colour	Dark Black

Composition of concrete and mix design

Concrete and mix design composition is a critical aspect of achieving this universal construction material's desired properties and performance. Concrete is typically composed of four primary components: cement, aggregates (comprising coarse and fine aggregates), water, and admixtures. The ratio of these ingredients, known as the mix design, is accurately determined to meet specific project requirements. The mix design takes into account factors such as desired compressive strength, workability, durability, and environmental conditions. It involves selecting the appropriate type and proportion of cement, aggregates, water-cement ratio, and the addition of admixtures. In this study, the concrete grades M20 is designed with four different combinations of materials. These combinations were determined based on the authors' experience and literature support.

The control sample, which served as a reference, did not include any recycled aggregates and marble powder in its composition. The remaining three mixtures underwent evaluation, with varying percentages of recycled crushed marble, marble powder and over-burnt bricks replacing fine aggregates and coarse aggregate. The replacement percentages for recycled marble aggregates were set at 0%, 5%, 10%, and 15% of the total fine aggregate content. The mix design was calculated in accordance with IS: 456 [13]. In accordance with the mix design calculations, all concrete ingredients were precisely blended together using manual mixing techniques. Once the mixing process was finalized, the concrete casting phase was initiated, and the entire mixing process concluded within a time frame of 10 to 15 minutes. The mixture ratios are detailed in Table 5 and 6.

Table 5: Proportions of the concrete compositions

Items	**Case-1**	**Case-2**	**Case-3**	**Case-4**
Cement	0	5	10	15
Fine Aggregate	0	10	15	5
Coarse Aggregate	0	15	5	10

Table 6: Mix Design of Concrete

Items	Case-1	Case-2	Case-3	Case-4
Cement (kg)	3.2	3.04	2.88	2.72

Marble Powder (kg)	0	0.16	0.32	0.48
Fine Aggregate (kg)	5.73	5.15	4.88	5.44
Crushed Marble (kg)	0	0.57	0.86	0.28
Coarse Aggregate (kg)	10.5	8.92	9.98	9.45
Over burnt bricks (kg)	0	1.57	0.52	1.05
Case 1: C : F.A. : C.A. = 1 : 1.82 : 3.34 Case 2: C : M.P : F.A : C.M : C.A : O.B = 1 : 0.05 : 1.69 : 0.18 : 2.93 : 0.18 Case 3: C : M.P : F.A : C.M : C.A : O.B = 1 : 0.11 : 1.69 : 0.29 : 3.46 : 0.18 Case 4: C : M.P : F.A : C.M : C.A : O.B. = 1 : 0.17 : 2 : 0.10 : 3.47 : 0.38 # C: cement; MP: marble powder; FA: fine aggregate; CM: crushed marble; CA: coarse aggregate; OB: over-burnt bricks				

Test Methods

The need for assessing the workability of concrete through the slump cone test arises from its fundamental importance in construction. Workability refers to the ease with which concrete can be mixed, placed, compacted, and finished while maintaining its desired properties. The workability of concrete is a critical aspect evaluated through the slump cone test in the context of enhancing concrete strength by partially substituting conventional materials. During the test, a slump cone is filled with freshly mixed concrete in layers and compacted. Subsequently, the cone is carefully lifted, and the amount by which the concrete settles or slumps is measured. It ensures that while following improvements in concrete strength, the material remains practical for construction purposes. The slump cone test, in this case, aids in promoting the right balance between enhanced strength and workability, ultimately contributing to the successful and efficient execution of construction projects. In addition, in the context of enhancing concrete strength through the partial substitution of conventional materials with marble powder, crushed marble and over-burnt bricks, conducting a compressive strength test is crucial. The need for this test arises from the fundamental requirement of ensuring that the modified concrete mixture maintains or exceeds the minimum strength standards expected for the intended application. By incorporating unconventional materials such as marble powder, crushed marble, and over-burnt bricks into the mix, it becomes imperative to validate the structural competence of the resulting concrete. The compressive strength of cubes (Fig. 4), with dimensions of 15 × 15 × 15 cm, was determined according to the IS 516 standard at a curing period of 28 days. The specimens are placed in a compression testing machine, commonly known as the universal testing machine. The test machine applies a gradually increasing axial load to the specimen in a controlled manner until the concrete fails. Compressive strength testing assists in optimizing the mix design by modifying the proportions of conventional and unconventional materials to achieve the desired strength characteristics.

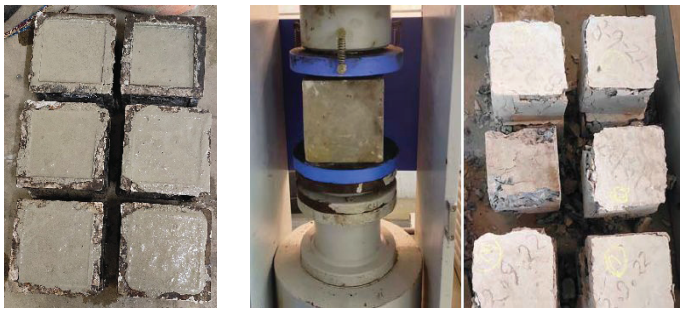

Figure-4: Compressive strength test

Results and Discussions

The effect of partial replacement of cement with marble powder has been observed. The table below depicts the effect of partial replacement of cement with marble powder.

Table 7: Effect of partial replacement of cement with marble powder

Percentage replacement by weight	Compressive strength (MPa)	
	7 days	28 days
0%	11.35	26.9
5%	12.93	29.62
10%	13.09	30.4
15%	12.50	26.1

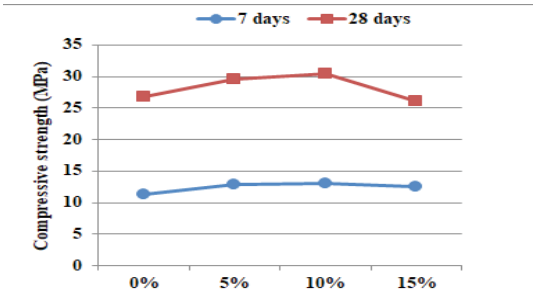

Figure-5: Compressive strength at various percentage replacement of cement with marble powder

When fine aggregate was partially replaced with crushed marble, then it was seen that maximum compressive strength was obtained at 15% replacement of fine aggregate with crushed marble. The data has been presented in tabular form below. The same data was plotted in graphical form in Figure 5. Both curves for 7 days and 28 days compressive

strength, the natures of curves are increasing. So 15% replacement of crushed marble with the fine aggregates gives the maximum strength.

Table 8: Effect of partial replacement of fine aggregate with crushed marble

Percentage replacement by weight	Compressive strength (MPa)	
	7 days	28 days
0%	9.45	23.5
5%	11.65	26.4
10%	12.10	27.85
15%	12.90	28.4

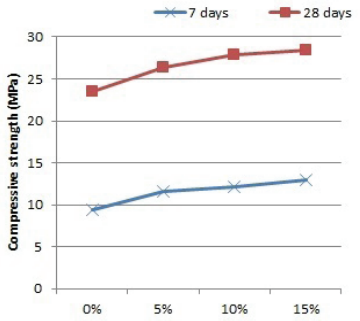

Figure-6: Compressive strength at various percentage replacement of fine aggregate with crushed marble

As it is evident from the above table that 7 day compressive strength test, up to 10% replacement of cement with crushed marble powder. Beyond this the compressive strength shows a down fall. So, the partial replacement of cement with 10% crushed marble powder is considered the optimum mix.

Coarse aggregates were partially replaced with over burnt bricks. Also the compressive strength was obtained for various percentage replacement of fine aggregate with crushed marble. Both curves for 7 days and 28 days compressive strength, the natures of curves are decreasing beyond 5%. So 5% replacement of coarse aggregates with over burnt bricks gives the optimum result.

Table 9: Effect of partial replacement of coarse aggregate with over burnt bricks

Percentage replacement by weight	Compressive strength (MPa)	
	7 days	28 days
0%	8.35	22.50
5%	11.25	24.30
10%	9.10	21.85
15%	9.50	21.40

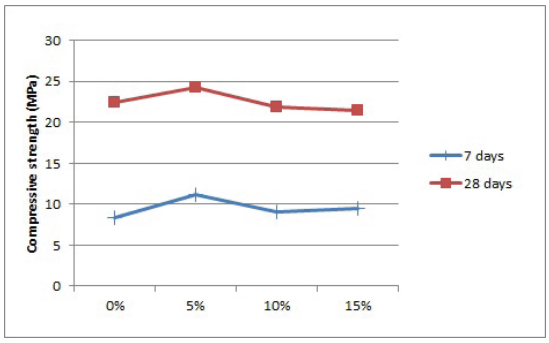

Figure-7: Compressive strength at various percentage replacement of coarse aggregate with over burnt bricks

The results obtained after mixing marble powder, crushed marble and over burnt brick is being presented here. The table below shows results from slump cone test for measurement of workability in mm.

Table 10: Test results from slump cone test for workability in mm

Items	% replacement (MP + CM + Over burnt Brick)	Over burnt bricks (kg)
Case 1	0 + 0 + 0	100
Case 2	5 + 10 + 15	90
Case 3	10 + 15 + 5	105
Case 4	15 + 5 + 10	96

The plot of slump height (mm) for various cases of mix design viz. case 1 , case 2, case 3 and case 4 have been depicted in the graph below.

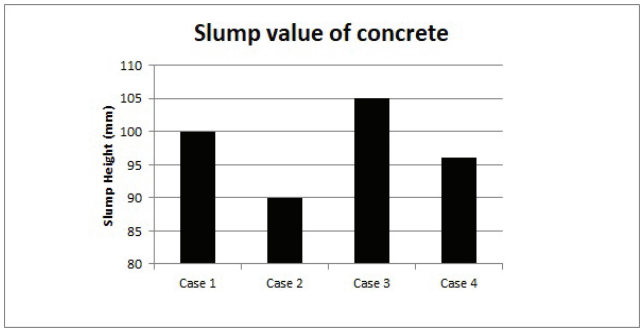

Figure-8: Slump values of concrete

Table 11: Compressive strength test results for different cases at 7 days and 28 days

Items	7 day	28 day
Case 1	11.35	26.9
Case 2	12.93	29.62
Case 3	13.09	30.4
Case 4	12.5	26.1

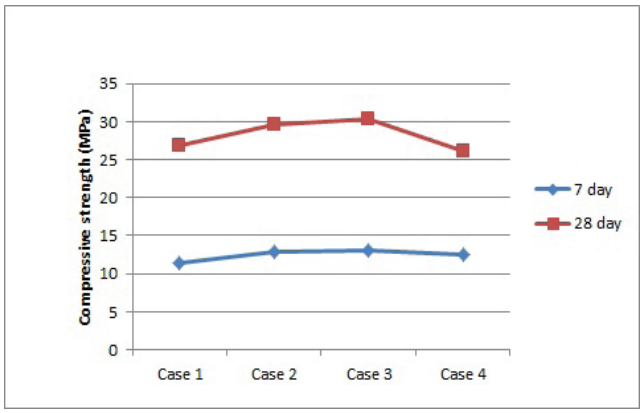

Figure-9: Compressive strength at test results for different cases at 7 days and 28 days

So, it is observed that for Case 3, the compressive strength is maximum at 7 days as well as 28 days which is 15.33 % and 13.01% more than original strength respectively.

Conclusions

This study explores the potential of enhancing concrete strength by partially substituting conventional materials with three alternative components: marble powder, crushed marble, and over-burnt bricks. These materials, often overlooked or considered waste, are repurposed to create a more robust and environmentally friendly concrete mixture. The research investigates their impact on workability and compressive strength, providing valuable insights into optimizing concrete mix designs for both performance and sustainability. The incorporation of these alternative materials into concrete mixtures has shown a positive impact on workability. Despite concerns about potential irregularities in particle size and shape, the concrete remains highly workable, allowing for efficient placement and construction processes. Furthermore,

one of the most significant findings of this study is the substantial increase in compressive strength. Concrete specimens with partial substitutions consistently exhibited higher compressive strength values compared to the control group, demonstrating the effectiveness of these materials in improving structural performance. Beyond the technical aspects, this research highlights the sustainability benefits of utilizing waste materials like marble powder and over-burnt bricks in concrete production. By repurposing these materials, we reduce waste disposal and resource consumption, contributing to more eco-friendly construction practices.

REFERENCES

1. Yucel H.E., Dutkiewicz M., and Yildızhan F., The Effect of Waste Ballast Aggregates on Mechanical and Durability Properties of Standard Concrete, Materials, Vol. 16, Issue 7, 2023, pp. 2665.
2. Sharma A., Chauhan A.S., Jain A., and Jangid, J.B., Utilization of Waste Material to Make Green Concrete, Int. Res. J. Eng. Technology, Vol. 7, 2020, pp. 2666-2669.
3. Banerji A.K., Topdar P., and Datta A.K., Structural Performance of Cement-treated Base Layer by Incorporating Reclaimed Asphalt Material and Plastic Waste, Jordan Journal of Civil Engineering, Vol. 17, Issue 2, 2023, pp. 259-271.
4. Basaran B., Kalkan I., Aksoylu C., Özkılıç, Y.O., and Sabri, M.M.S., Effects of waste powder, fine and coarse marble aggregates on concrete compressive strength, Sustainability, Vol. 14, Issue 21, 2022, pp. 14388.
5. Kumar M.A., Balaji S., Selvapraveen, S., and Kulanthaivel, P., Laboratory study on mechanical properties of self compacting concrete using marble waste and polypropylene fiber, Cleaner Materials, Vol. 6, 2022, pp. 100156.
6. Ulubeyli G.C., Bilir T., and Artir R., Durability properties of concrete produced by marble waste as aggregate or mineral additives, Procedia engineering, Vol. 161, 2016, 543-548.
7. Singh M., Choudhary K., Srivastava A., Sangwan K.S., and Bhunia D., A study on environmental and economic impacts of using waste marble powder in concrete, Journal of Building Engineering, Vol. 13, 2017, pp. 87-95.
8. Wang Y., Xiao J., Zhang J., and Duan Z., Mechanical behavior of concrete prepared with waste marble powder, Sustainability, Vol. 14, Issue 7, 2022, pp. 4170.
9. Khan K., Ahmad W., Amin M.N., Ahmad A., Nazar S., Alabdullah A.A., and Arab A.M.A., Exploring the use of waste marble powder in concrete and predicting its strength with different advanced algorithms, Materials, Vol. 15, Issue 12, 2022, pp. 4108.
10. Apebo N.S., Shiwua A.J., Agbo A.P., Ezeokonkwo J.C., and Adeke P.T., Effect of

Water-Cement Ratio on the Compressive Strength of gravel-crushed over burnt bricks concrete, Civil and Environmental Research, Vol. 3, Issue 4, 2013, pp. 74-81.

11. Praveen K., Sathyan D., and Mini K.M., Study on performance of concrete with over-burnt bricks aggregates and micro-silica admixture, In IOP Conference Series: Materials Science and Engineering, Vol. 149, Issue 1, 2016, pp. 012061.
12. Ahmadi M., Abdollahzadeh E., and Kioumarsi M., Using marble waste as a partial aggregate replacement in the development of sustainable self-compacting concrete, Materials Today: Proceedings (2023).
13. IS 456. (2000). Indian Standard Plain and Reinforced concrete-code of conduct, Bureau of Indian Standards, New Delhi.
14. IS 516. (2004). Indian Standard Code for Methods of Tests for Strength of Concrete, Bureau of Indian Standards, New Delhi.

NEW DELHI PUBLISHERS
Head Office:
90 Sainik Vihar, Mohan Garden, Uttam Nagar,
New Delhi, India
Corporate Office:
7/28, Room No 208-209, Vardaan House, Ansari Road,
Daryaganj, New Delhi, India
Branch Office:
216, Green Park, Narendrapur, Kolkata, India
Phone number: 011-23256188, 9971676330, 9582248909
Email: ndpublishers@gmail.com
Website: www.ndpublisher.in

ISBN: 978-81-19006-98-4